



**HAL**  
open science

# Including a meso-structure in multi-scale modeling of granular soils

Huaxiang Zhu

► **To cite this version:**

Huaxiang Zhu. Including a meso-structure in multi-scale modeling of granular soils. Materials. Université Grenoble Alpes, 2015. English. NNT : 2015GREAI094 . tel-01278364

**HAL Id: tel-01278364**

**<https://theses.hal.science/tel-01278364>**

Submitted on 24 Feb 2016

**HAL** is a multi-disciplinary open access archive for the deposit and dissemination of scientific research documents, whether they are published or not. The documents may come from teaching and research institutions in France or abroad, or from public or private research centers.

L'archive ouverte pluridisciplinaire **HAL**, est destinée au dépôt et à la diffusion de documents scientifiques de niveau recherche, publiés ou non, émanant des établissements d'enseignement et de recherche français ou étrangers, des laboratoires publics ou privés.

## THÈSE

Pour obtenir le grade de

### DOCTEUR DE L'UNIVERSITÉ GRENOBLE ALPES

Spécialité : **mécanique, matériaux, génie mécanique, génie civil**

Arrêté ministériel : 7 août 2006

Présentée par

**Huaxiang ZHU**

Thèse dirigée par **François NICOT** et  
codirigée par **Félix DARVE**

préparée au sein du **IRSTEA-Grenoble**  
dans l'**École Doctorale Ingénierie, Matériaux, Energétique,**  
**Environnement, Procédés, Production (I-MEP2)**

# Prise en compte d'une échelle intermédiaire dans la modélisation micro-structurale des sols granulaires

Thèse soutenue publiquement le **11 Décembre 2015**,  
devant le jury composé de :

**Professor, Bernard CAMBOU**

Professor, École Centrale de Lyon, Rapporteur

**Professor, Niels KRUYT**

Professor, University of Twente, Rapporteur

**Professor, Jean LERBET**

Professor, Université Evry Val d'Essonne, Président

**Professor, Francesco FROILIO**

Professor, École Centrale de Lyon, Examineur

**Professor, Félix DARVE**

Professor, INP-Grenoble, Co-directeur de thèse

**Professor, François NICOT**

Professor, IRSTEA-Grenoble, Directeur de thèse





---

# Including a meso-structure in multi-scale modeling of granular soils

Huaxiang ZHU

---



Grenoble 2015



---

# **Including a meso-structure in multi-scale modeling of granular soils**

**Huaxiang ZHU**

---

Huaxiang ZHU  
Irstea de Grenoble  
Unité de Recherche Erosion Torrentielle Neige et Avalanches  
Domaine Universitaire, BP 76  
F38402 – Saint Martin d’Hères Cedex – France  
[huaxiang.zhu@irstea.fr](mailto:huaxiang.zhu@irstea.fr)

# Abstract

Granular materials exhibit a wide spectrum of constitutive features under various loading paths. Developing constitutive models which succeed to characterize these features has been challenging scientists for decades. A promising direction of achieving this can be the multi-scale approach. Through this approach the constitutive model is formulated by relating material's macroscopic properties to their corresponding micro-structure properties.

A comprehensive investigation has been carried out on the basis of numerical biaxial tests using a 2D discrete element method (DEM), in order to ascertain the micro-structure characteristics of the granular material, the way they evolve along the loading path and roles they play in the macroscopic behaviors. In a meso-scale, intermediate between the single contact scale and the macro-scale, the force transmission network (force-chains) and area element enclosed by contacts branches (meso-loops) are highlighted in terms of their significant influences on material's macro-scale behavior. Meso-loops herein are tessellated from the whole area of the granular assembly by the contact network, and are subsequently categorized according to their side number.

The development of meso-loops is observed to be intimately related to material's volumetric evolution, especially to the plastic part. Then, the interaction between force-chains and meso-loops and the significance of this interaction to the global volumetric behavior and the macroscopic strength are revealed. Meso-loops with 3 sides ( $L_3$ ) appear to be indispensable for the force-chain stability, meanwhile, meso-loops with more than or equal to 6 sides ( $L_{6+}$ ) contribute much to the volume expansion and accelerate the buckling of the force-chain they confine. Otherwise, in the critical state, an identical

meso-structure is found in the failure area of both localized and diffuse failure mode. To this extent,  $L_3$  and  $L_{6+}$  are enormously important for the granular material to transmit forces and to perform the volumetric variation.

A constitutive model has been developed by modifying the H-directional model (Nicot and Darve, 2011b). In this model, the individual hexagons, the representatives of  $L_{6+}$ , construct the fabric as distributing along different directions in the space. A homogenization approach is then used to relate macroscopic properties to local ones. This model is then validated in different loading paths, and eventually proved satisfying.

**Keywords:**

Failure, instability, micro-structure, constitutive modeling, multi-scale, DEM

# Résumé

Les matériaux granulaires exhibent un spectre très large de propriétés constitutives, le long de chemins de chargement très divers. Développer des modèles constitutifs permettant de reproduire ces caractéristiques a demeuré un réel challenge scientifique au cours des dernières décennies. A cet égard, les approches multi-échelles constituent aujourd'hui une voie très prometteuse. Elles permettent de relier les propriétés macroscopiques à celles observées à l'échelle microscopique.

Une investigation a été menée sur la base de simulations numériques discrètes (DEM) d'essais biaxiaux, afin d'identifier les caractéristiques micro-structurelles du matériau granulaire, la manière dont elles évoluent au cours d'un chemin de chargement, et le rôle qu'elles jouent dans l'émergence du comportement macroscopique. A l'échelle mésoscopique, le réseau de transmission de force (chaines de force) et les cellules définies par les vecteurs branches (meso-cycles) apparaissent jouer un rôle de première importance. Les meso-cycles, construits à partir du réseau de contact de l'assemblage, peuvent être caractérisés en fonction du nombre de cotés qu'ils contiennent (topologie). Leur influence sur le comportement volumique de l'échantillon est en effet étroitement liée à ce nombre de contact. En outre, leur interaction avec les chaines de force est également fortement dépendante de leur topologie. Ainsi, les cycles contenant 3 cotés ( $L_3$ ) participent activement à la stabilisation des chaines de force, alors que les cycles contenant au moins 6 cotés ( $L_{6+}$ ) contribuent essentiellement au comportement dilatant de l'échantillon et à l'effondrement des chaines de force. Enfin, l'existence d'une méso-structure unique à l'état critique, au sein de la bande de cisaillement (rupture localisée) ou au sein de l'échantillon (rupture diffuse), est clairement démontrée.

Sur la base de ces résultats, un modèle constitutif a été développé à partir du modèle H-directionnel (Nicot and Darve, 2011b). La structure du matériau granulaire est décrite par un assemblage d'hexagones (modélisant les cycles  $L_6$ ), orientés dans toutes les directions de l'espace. A partir d'opérations d'homogénéisation, les contraintes et les déformations incrémentales peuvent être reliées à l'échelle de l'assemblage, donnant lieu à un modèle de comportement dont la performance a pu être testée le long de chemins de chargements variés.

**Mots clés:**

Rupture, Instabilité, micro-structure, modélisation constitutive, Multi-échelle, DEM

# Contents

<b>Abstract</b>	<b>v</b>
<b>Résumé</b>	<b>vii</b>
<b>1 General Introduction</b>	<b>1</b>
1.1 Background: micro-structure of the soil and multi-scale approach . . . . .	1
1.2 Constitutive modeling for granular material: knowledge and problems . . . . .	3
1.2.1 micro-structure investigation . . . . .	3
1.2.1.1 Material fabric and its evolution . . . . .	4
1.2.1.2 Structures in a meso-scale . . . . .	8
1.2.2 Constitutive modeling based on the fabric . . . . .	12
1.3 Objectives . . . . .	13
1.4 Outline of this thesis . . . . .	15
1.5 Conclusion . . . . .	16
<b>2 Numerical Modeling by Discrete Element Method</b>	<b>17</b>
2.1 Introduction of discrete element method . . . . .	18
2.1.1 Calculation cycle . . . . .	19
2.1.2 Contact law . . . . .	21
2.1.3 Calculation of the particle displacement . . . . .	22
2.1.4 Computational stability condition . . . . .	23
2.1.5 Yade-DEM software . . . . .	24
2.2 Biaxial tests in DEM . . . . .	24
2.2.1 Parameters . . . . .	24
2.2.2 Applying confining load and Consolidating . . . . .	25
2.2.3 Drained biaxial loading . . . . .	26
2.3 Conclusion . . . . .	27
<b>3 Micro-structure Analysis in 2D Granular Material</b>	<b>29</b>
3.1 Micromechanics of granular material . . . . .	30
3.1.1 Description of the fabric . . . . .	31
3.1.2 Static and kinematic homogenization . . . . .	33
3.2 Meso-structure: force-chains and meso-loops . . . . .	35
3.2.1 Force-chains . . . . .	35
3.2.2 Meso-loops . . . . .	37
3.3 Meso-loops evolution during biaxial loading . . . . .	38
3.3.1 Drained biaxial test and results . . . . .	39
3.3.2 Meso-loops evolution . . . . .	42
3.3.2.1 Proportional analysis of different loops . . . . .	44

3.3.2.2	Area change of different loops . . . . .	47
3.3.3	The existence of elastic and plastic phases in meso-scale . . . . .	50
3.3.3.1	Elasticity and plasticity in the meso-scale . . . . .	50
3.3.3.2	Elastic energy and plastic dissipation . . . . .	51
3.3.3.3	Plastic volumetric strain in dense packed assemblies . . . . .	53
3.3.3.4	Effect of elasticity on volumetric evolution . . . . .	54
3.4	Force-chain interaction with meso-loop in biaxial loading path . . . . .	55
3.4.1	Macroscopic responses and mesoscopic evolutions . . . . .	56
3.4.2	Force-chain induced meso-loop differentiation . . . . .	59
3.4.2.1	Evolution on <i>FCL</i> and <i>NFCL</i> . . . . .	59
3.4.2.2	Conversion correlations amongst structures . . . . .	61
3.4.2.3	Volumetric behavior . . . . .	65
3.4.3	Effect of confining structures on force-chains . . . . .	67
3.4.3.1	Confining structures and force-chain movability . . . . .	67
3.4.3.2	Stress anisotropy of confining loops . . . . .	68
3.5	The critical state meso-structure in localized and diffuse failure modes . . . . .	72
3.5.1	Drained biaxial test and results . . . . .	75
3.5.2	Failure modes and shear band width in specimens . . . . .	76
3.5.3	Critical state void ratio $e$ . . . . .	80
3.5.4	Meso-structure signature of the critical state . . . . .	82
3.5.4.1	Meso-loops characteristics . . . . .	83
3.5.4.2	Force-chain characteristics . . . . .	87
3.5.4.3	Discussion: the homology of localized and diffuse failure modes . . . . .	94
3.6	Conclusion . . . . .	96
3.6.1	Meso-loop evolution during biaxial loading . . . . .	96
3.6.2	Force-chain interaction with meso-loop along biaxial loading path . . . . .	97
3.6.3	The critical state meso-structure in localized and diffuse failure modes . . . . .	99
<b>4</b>	<b>A Multi-scale Approach Constitutive Model</b> . . . . .	<b>101</b>
4.1	Reviews on the micro-directional model and the H-directional model . . . . .	102
4.1.1	The micro-directional model . . . . .	103
4.1.2	limitations of micro-directional model . . . . .	106
4.1.3	H-directional model . . . . .	108
4.2	Modified H-directional model . . . . .	112
4.2.1	Constitutive relations . . . . .	113
4.2.2	Model performances . . . . .	116
4.2.3	Prospectives on improving the H-directional model . . . . .	123
4.3	Conclusion . . . . .	125
<b>5</b>	<b>General Conclusion</b> . . . . .	<b>129</b>
5.1	Conclusion . . . . .	129
5.2	Open issues and perspectives . . . . .	132

# List of Figures

1.1	Force fabric in the granular assembly made up of photoelastic material, in a simple shear test. The brightness of light lines presents the force magnitude (Zhang et al., 2008). . . . .	9
1.2	Contact network composed of contact branches in the 2D granular assembly. Black continuous lines are contact branches, gray disks are grains. . . . .	9
2.1	Calculation cycle of <i>DEM</i> . . . . .	20
2.2	Elasto-frictional contact law: (a) components in the contact; (b) elasto-frictional behavior in the tangential direction. . . . .	22
2.3	Biaxial test model in <i>DEM</i> . . . . .	25
3.1	Contact variables of a two-particle pair. . . . .	31
3.2	General homogenization scheme for multi-scale approaches of the granular material. . . . .	33
3.3	The inflection angle $\theta$ in two configurations ( $\theta_0$ in configuration 0 and $\theta_t$ in configuration $t$ ). Continuous fold lines link two outer particle centers to the middle particle center, dashed fold line in configuration $t$ refers to the original position of the fold line in configuration 0. . . . .	36
3.4	The area tessellation by branch network. . . . .	37
3.5	One identified cycle . . . . .	38
3.6	Algorithm of detecting cycle . . . . .	38
3.7	Evolutions with respect to axial strain $\varepsilon_2$ of (a) deviatoric stress ratio $q/p_0$ , (b) volumetric strain $\varepsilon_v$ , (c) coordination number $Z$ (d) total number of loops $N_l$ . . . . .	41
3.8	Four categories of loops. . . . .	42
3.9	Evolutions of $\omega_6$ and $\omega_{7+}$ against axial strain $\varepsilon_2$ in specimen (a) $\phi_0 = 0.148$ (b) $\phi_0 = 0.171$ (c) $\phi_0 = 0.187$ . . . . .	43
3.10	Evolutions in specimen $\phi_0 = 0.148$ with respect to axial strain $\varepsilon_2$ of (a) deviatoric stress $q/p_0$ and volumetric strain $\varepsilon_v$ , (b) proportions of different loops compared with the volumetric strain $\varepsilon_v$ ; the vertical dashed line is the guide line crossing the volume minimum. . . . .	44
3.11	Evolutions in specimen $\phi_0 = 0.171$ with respect to axial strain $\varepsilon_2$ of (a) deviatoric stress $q/p_0$ and volumetric strain $\varepsilon_v$ , (b) proportions of different loops compared with the volumetric strain $\varepsilon_v$ ; the vertical dashed lines respectively cross the $\omega_3$ maximum and the volume minimum. . . . .	45
3.12	Evolution in specimen $\phi_0 = 0.187$ with respect to axial strain $\varepsilon_2$ of (a) deviatoric stress $q/p_0$ and volumetric strain $\varepsilon_v$ , (b) ratio of different loops compared with the volumetric strain $\varepsilon_v$ . . . . .	46
3.13	Evolution of area ratio $a_i$ of different loops against axial strain $\varepsilon_2$ in specimen (a) $\phi_0 = 0.148$ (b) $\phi_0 = 0.171$ (c) $\phi_0 = 0.187$ . . . . .	48

3.14	Evolution of average area $\bar{A}_i$ of different loops against axial strain $\varepsilon_2$ in specimen (a) $\phi_0 = 0.148$ (b) $\phi_0 = 0.171$ (c) $\phi_0 = 0.187$ . . . . .	49
3.15	Evolution of incremental elastic and plastic energy, compared with the evolution of $\varepsilon_v$ , in terms of the axial strain $\varepsilon_2$ , in specimen (a) $\phi_0 = 0.148$ (b) $\phi_0 = 0.171$ . . . . .	52
3.16	Evolution of plastic volumetric strain $\varepsilon_v^p$ and total volumetric strain $\varepsilon_v$ in terms of axial strain $\varepsilon_2$ in specimen (a) $\phi_0 = 0.152$ (b) $\phi_0 = 0.172$ . . . . .	53
3.17	Evolution of volumetric strain $\varepsilon_v$ of specimens with different elastic parameters with respect to axial strain $\varepsilon_2$ . . . . .	54
3.18	Evolutions of the ratio of loops $\omega_i$ , of the number of buckling events $N_b$ (upper), of the stress ratio $q/p_0$ and of the volumetric strain $\varepsilon_v$ (lower) with respect to axial strain $\varepsilon_2$ , for dense (a) and loose (b) specimens. . . . .	57
3.19	Evolution of $\omega_{6+}$ and of buckling events number $N_b$ (including fitting quartic polynomial) with respect to $\varepsilon_2$ in the loose specimen. . . . .	58
3.20	Illustration of the force-chain loop (force-chains are in dark grey; reminding particles are grey; FCL are highlighted by the transparent shadow). . . . .	59
3.21	Evolutions of the ratio of loops $\omega_i$ and of the number of buckling events $N_b$ (left) with respect to axial strain $\varepsilon_2$ . FCL in dense specimen (a), NFCL in dense specimen (b), FCL in loose specimen (c) and NFCL in loose specimen (d). . . . .	60
3.22	$\omega_3^{FCL}$ varies as function of $\omega_{6+}^{FCL}$ , grey line is the linear fit of scalar points. . . . .	62
3.23	Phases on loading path for (a) dense specimen and (b) loose specimen. . . . .	63
3.24	Pearson's $r$ between $d\omega_3$ and $d\omega_i$ ( $i = 4, 5, 6+$ ) in three phases of the dense specimen for (a) FCL and (b) NFCL. . . . .	63
3.25	Pearson's $r$ between $d\omega_3$ and $d\omega_i$ ( $i = 4, 5, 6+$ ) in two phases of the loose specimen for (a) FCL and (b) NFCL. . . . .	64
3.26	An illustration of the total area and the solid area (shadowed) in a set of loops (inside ABCDEFG). . . . .	66
3.27	Evolutions of void ratio $e$ of FCL, NFCL and total area in (a) dense and (b) loose specimens with respect to $\varepsilon_2$ . . . . .	66
3.28	Confining structures and force-chain movability. . . . .	67
3.29	Quartiles of $\log(\theta_b)$ of 3-particle sets for different levels of $N_i$ ( $i = 3, 4, 5, 6+$ ) for (a) $\varepsilon_2 = 0.018$ in the dense specimen and (b) $\varepsilon_2 = 0.050$ in the loose specimen. . . . .	69
3.30	Force-chain life-cycle. . . . .	70
3.31	An illustration of calculating the loop stress tensor $\tilde{\sigma}_{ij}^L$ . The loop considered here is <i>loop 0</i> (or loop ABCDE), $\tilde{\sigma}^{CD}$ is the total area of <i>loop 0</i> and <i>loop 1</i> . . . . .	71
3.32	Evolutions of normalized deviatoric meso stress $D^{meso}$ with respect to $\varepsilon_2$ in (a) dense and (b) loose specimens. . . . .	71
3.33	Evolutions of stress (a), strain (b) and void ratio $e$ (c) with respect to axial strain $\varepsilon_2$ , in specimens S1, S2, S3 and S4. . . . .	76
3.34	$ \Delta u $ nephogram ( $10^{-5}$ m) for specimen S1 (a), S2 (b), S3 (c) and S4 (d). Shear bands are bounded by grey lines with width $2\delta$ . . . . .	77
3.35	The profile of diagonal shear band, framed between two dashed lines. The shear band is assumed to extend symmetrically from diagonal (the continuous line from left-bottom to right-top corner in this figure), and the extension distance is denoted by $\delta$ . A coordinate $\alpha$ is set perpendicularly to the diagonal, as shear band lower and upper boundaries respectively correspond to $\alpha = -\delta$ and $\alpha = \delta$ . . . . .	78
3.36	For specimens S1 (a), S2 (b) and S3 (c), the variation of $\langle \varepsilon_{11} \rangle$ (scattered points) on reference line, which (being parallel with the specimen diagonal) moves along coordinate $\alpha$ . Scattered point are fitted by the solid line. Vertical dashed lines denote shear band boundaries. . . . .	79

3.37	Meso-loops inside prescribed boundaries (upper-left) and the illustration of the total area ( $ABCD$ ) and the solid area (shadowed) of one quadrilateral meso-loop (lower-right). . . . .	80
3.38	With respect to axial strain $\varepsilon_2$ , evolution of global void ratio $e$ and void ratio inside shear band $e^*$ for specimens S1 (a), S2 (b) and S3 (c), comparing with evolution of $e$ in specimen S4. . . . .	82
3.39	With respect to axial strain $\varepsilon_2$ , evolutions of meso-loop ratios $\omega_3$ (a), $\omega_{6+}$ (b), $\omega_4$ (c) and $\omega_5$ (d) in area S1*, S2*, S3* and S4. . . . .	83
3.40	Evolution of $D_H$ as function of $\varepsilon_2$ in analyzing area S1*, S2*, S3* and S4 (a); S1, S2, S3 and S4 (b). Evolution of $I_H$ as function of $\varepsilon_2$ in analyzing area S1*, S2*, S3* and S4 (c); S1, S2, S3 and S4 (d). . . . .	86
3.41	Force-chain distribution (in light blue) and buckling particles (in red) for specimens (a) S1, (b) S2, (c) S3 and (d) S4 . . . . .	88
3.42	Age density distribution of all 3-particle sets in specimens (a) S1, (b) S2, (c) S3 and (d) S4 at strain state $\varepsilon = 0.200$ . Distribution in S4 is exponentially fitted by a continuous line. The value of $p$ is divided into two parts: contributions given by inside shear band area (denoted by asterisk superscript, $p^*$ ) and by outside shear band area (denoted by superscript "osb", $p^{osb}$ ). . . . .	90
3.43	Age density distributions and their fitted lines of all 3-particle sets in shear band area of specimens (a) S1, (b) S2 and (c) S3 at strain state $\varepsilon = 0.200$ . . . . .	93
4.1	General homogenization scheme for multi-scale approaches. . . . .	103
4.2	Deviatoric stress and volumetric strain evolution in terms of axial strain, in the calibration along a symmetric drained triaxial loading path, involving unloading and reloading stages. . . . .	107
4.3	The hexagonal element of the H-directional model. . . . .	109
4.4	local kinematic variables in a hexagon . . . . .	110
4.5	local static variables in a hexagon . . . . .	110
4.6	Configuration of the hexagon with local kinematic and static variables. (a) local kinematic variables; (b) layout of particles in the hexagon subjected to external forces; (c) local static variables . . . . .	114
4.7	The stress and volumetric strain response along a drained biaxial loading path, using the modified H-directional model with parameters setting as $\phi_g = 30^\circ$ , $e_0(\vec{n}) = 0.40$ and $p_0 = 200kPa$ . line 1 - $\varepsilon_1 = 0.000$ , line 2 - $\varepsilon_1 = 0.125$ , line 3 - $\varepsilon_1 = 0.250$ , line 4 - $\varepsilon_1 = 0.500$ , line 5 - $\varepsilon_1 = 1.000$ , line 6 - $\varepsilon_1 = 2.000$ and line 7 - $\varepsilon_1 = 4.250$ . . . . .	117
4.8	Angular distributions of local variables in strain states, corresponding to lines in Figure 4.7. In each sub-figure, three figures are shown: the angular distribution of the average local stress $\tilde{\sigma}_n(\theta)$ and $\tilde{\sigma}_t(\theta)$ (left); the plastic and tensional orientations (center); the evolution of $\alpha_3$ in terms of orientations (right). . . . .	118
4.9	In drained biaxial test, evolutions of stress ratio in terms of axial strain in specimens of (a) be initialized with various $p_0$ ( $\phi_g = 30^\circ$ and $e_0(\vec{n}) = 0.40$ ); and (b) various $\phi_g$ ( $e_0(\vec{n}) = 0.60$ and $p_0 = 200kPa$ ). . . . .	121
4.10	A divergence on the stress response between a loose ( $e_0(\vec{n}) = 0.50$ ) and a dense ( $e_0(\vec{n}) = 0.63$ ) specimen, subjected to undrained biaxial test. The gray dashed line is the Mohr-Coulomb surface drawn by drained biaxial tests. $\phi_g = 33^\circ$ and $p_0 = 200kPa$ . . . . .	122
4.11	The stress response of a specimen, when subjected to proportional loading path with different $R$ ( $\varepsilon_2 = R\delta\varepsilon_1$ ). The gray dashed line is the Mohr-Coulomb surface drawn by drained biaxial tests. $\phi_g = 30^\circ$ , $e_0(\vec{n}) = 0.55$ and $p_0 = 200kPa$ . . . . .	123

- 4.12 The evolution of the ratio of the number of the  $L_{6+}$  over  $L_3$  in terms of the void ratio  $e$  in the shear band area of S1, S2 and S3 and in the whole area of S4 . . . . . 124

# List of Tables

2.1	Parameters in the simulation. . . . .	26
3.1	Parameters in the simulation. . . . .	40
3.2	The initial porosity of three specimens. . . . .	40
3.3	Volumetric lowest values and their corresponding $\varepsilon_2$ for different specimens. . . . .	54
3.4	The initial porosity of specimens. . . . .	56
3.5	Specimens and corresponding initial void ratio. . . . .	75
3.6	Mean value and standard deviation of buckling events $N_b$ in critical state . . . . .	94
4.1	Simulation parameters . . . . .	116



# Chapter 1

## General Introduction

### 1.1 Background: micro-structure of the soil and multi-scale approach

A vast majority of human activities, so far, are limited on the ground by the gravity, and a vast majority of artificial structures are established with contacting to the earth. The soil, covering an enormous proportion of the land surface on the earth, considered to be the “skin of the earth”, is a kind of important material we should deal with in engineering practices of various types, such as civil engineering, environmental engineering, mining engineering, shore engineering and etc.

Being a big material class, the soil contains numerous members, classified according to different criteria, such as the class of the parent material, the grain size distribution and the consolidation history. Otherwise, as composed of gas, fluid and solid to be a three phases system, the soil behaves sensitively to the initial states of three phases, and the way three phases evolve along the loading path. The combination of these factors gives rise to a wide variation of the mechanical properties of the soil, among not only different kinds of soil but also different initial states and various applied loading paths. Up to date, the knowledge on the soil is limited and insufficient, especially when compared with the increasing need of human constructions and activities. Understanding soil’s features in different conditions and circumstances and developing models to simulate its behaviors, therefore, appear to be the fundamental topics for scientists and engineers in the geomechanics community.

The soil, consisting of soil grains, is basically a member of the granular material, which is a more general family involving the snow, the coal, different kinds of powder and etc. The constituents of granular materials, as what its name indicates, are discrete grains varying in size and shape. The granular system is simply governed by the frictional nature (with or without a cohesion) on the contact points and the given boundary conditions. However, when it assembles a great number of grains together into a complex system, a series of complex behaviors may consequently emerge, e.g. a highly incrementally non-linear constitutive behavior (Darve, 1990; Darve et al., 1995b), the existence of the non-associate flow rule, and the existence of a bifurcation domain within the plastic limit (Darve et al., 2004; Nicot et al., 2009). Besides, considering the importance of the granular material in application to diverse industries (Rhodes, 1990), such as civil engineering, pharmaceutical industry and agriculture, it has evoked great interest in the mechanics community in last decades. In this thesis, the soil, or called granular soil, is investigated and discussed in the general framework of granular materials.

Benefiting from the advancing of the measurement technique toward the microscopy, plentiful new techniques are introduced to observe the micro-structure of granular materials, such as electron microscope, photoelastic material and X-ray. Researchers are gradually capable of clarifying microscopic essences beneath macroscopic behaviors of the granular material. In dedications to this way, numerous features in the micro-scale are successively discovered, the fundamental roles played by different kinds of micro-structures in the material's mechanical behavior are successively recognized.

The material fabric and its decisive influence on the macroscopic mechanical properties have been a popular topic since the pioneering work of Oda (1972a,b,c). Considered as the core of stress-strain relation, the material fabric exists to be the bridge between the stress and strain. Furthermore, two kinds of self-organization of grains (or contacts), the force-chain and the loop, are observed to be prevalent micro-scale structures in granular materials and highlighted to be significant features with mechanical meanings. Force-chains are quasi-linear chains formed by grains transmitting forces of magnitude larger than the average value. It is the strong phase of the force network, as between these chains are regions of the low force carriage, in which grains are shielded by their neighbors vaulting or arching above (Kondic et al., 2012). The force-chain system, contributing most in sustaining external loading, is largely responsible of the force transmission in the specimen. The massive buckling of force-chains betoken a global loss of the material's sustainability against external loading, i.e. the instability of the material. Loops are the

elementary cells of the granular assembly enclosed inside by contact branches. Since the whole area of the granular assembly can be seamlessly tessellated into loops, they are elementary entities of the material's volume, therefore, strongly relating to the global volumetric behavior.

Another important work in the geomechanics is to develop constitutive models, which try to give mathematical relations for simulating the behavior of the material as close to the reality as possible. Last decades have seen many phenomenological models, which build constitutive relations by means of mathematically characterizing the different observed phenomena. This kind of model normally has to involve an exceeding number of parameters, whereas most of these parameters lack the physical background. With the advances in micro-scale investigations, more and more macroscopic phenomena are attributed to the microscopic characteristics of the material. Many researchers then turn to make the attempt of embedding the discovered micro-physics into the constitutive relation. This naturally requires the technique for changing scales between micro and macro, giving birth to the multi-scale approach. To this approach, problems of the constitutive modeling turn from how to properly formulate observed macroscopic phenomena to how to exactly characterize the basic micro-physics underlying the macroscopic phenomena and to sophisticatedly link them to macroscopic properties. This, reversely, brings forward a higher demand on investigating the micro-structure of the granular soil. Along the reasoning line of this approach, investigations and discussions in this thesis unfold.

## **1.2 Constitutive modeling for granular material: knowledge and problems**

### **1.2.1 micro-structure investigation**

The way and tool employed for implementing the experiment and measuring results may vary from one research to another, whereas all independent information in a granular assembly is no more than the static properties on contacts, i.e. the contact force, and kinematic properties on particles, i.e. the particles' position and velocity. Various analyses are then made on the basis of this information.

### 1.2.1.1 Material fabric and its evolution

In the granular material subjected to the quasi-static loading, two fabric systems are significant to the mechanical behavior: the material fabric and the force fabric. The material fabric refers to the contact network composed of all contact branches, while the force fabric is the network through which forces pass the material. In practice, the material fabric is the basis of the force fabric and, reversely, the force fabric can reconstruct the material fabric. The evolution and interaction of these two fabrics are essential microscopic ingredients of the granular assembly.

Oda (1972a,b,c) in a succession of works first highlighted the importance of the material fabric. By taking the tomography on sections of resin-glued sand sample subjected to the drained triaxial loading path, he measured the material fabric and quantitatively presented orientations of individual contacts into a density distribution  $E(\theta, \beta)$ , where  $\theta$  and  $\beta$  are two coordinates in the spherical coordinate system, determining the contact orientation.  $E(\theta, \beta)$  enabled the material fabric to be concisely characterized and compared between different strain states.  $E(\theta, \beta)$  was observed to increase its anisotropy with the increasing axial strain, the direction of this anisotropy was coincident to that of the axial strain. In his researches, the significant effect of the fabric anisotropy on the material's global mechanical properties was revealed in three aspects: (1) both the stress and the volumetric performances of the material were sensitive to the initial fabric anisotropy; (2) the stress anisotropy, i.e. the stress ratio, and stress-dilatancy was quantitatively related to the fabric anisotropy; and (3) the strain localization domain was highly associated with a localized value of the fabric anisotropy.

Hajime (1974) performed a special simple shear test, using cylindrical rods made up of the photoelastic material. The density distribution  $E(\theta)$  of contacts in preferred orientation  $\theta$  in 2D space and the contact forces were measured. By employing these microscopic quantities, he proposed the relation between the shear resistance ( $\tau/\sigma_N$ : the ratio the shear stress over the normal stress) and the dilatancy ratio ( $d\varepsilon_N/d\gamma$ : the incremental ratio the normal strain over the shear strain). In a similar test but employing oval rods, Oda et al. (1982) observed that before stress peak, contacts were built preferentially to the direction parallel to the major loading direction. A groundbreaking point which has to be mentioned is that the role of particles' rotation in granular material's deformation was highlighted, the traditional assumption that attributes shear deformation to the inter-particle sliding was doubted.

The orientational density distribution of contacts in both 2D ( $E(\theta, \beta)$ ) and 3D space ( $E(\theta)$ ) is not a function but a set of directional data in a finite length. This causes the inconvenience in mathematically manipulating it, especially in deriving constitutive relations. In the early 1980s, several solutions were proposed.

Oda et al. (1980) proposed to use the ellipsoid function approximating  $E(\theta, \beta)$ , by adjusting three parameters indicating the length of ellipsoid's axes. This function of the quadratic form can be associated to a second order tensor with a clear physical meaning. The reduction of the number of parameters was discussed in axis-symmetrical loading case. Satake (1982) introduced a general method for characterizing cracks' preferring orientation in the geomaterial. The fabric tensor  $H_{ij}$  was built by taking into account the orientation of all cracks. It can be adopted in the granular material, if seeing the contact as the crack. It was expressed as below,

$$H_{ij} = \int_0^{2\pi} \int_0^{\pi} E(\theta, \beta) n_i n_j \sin\theta \, d\theta d\beta, \quad (1.1)$$

where  $\vec{n}$  is the contact normal, the unit vector along contact orientation. The deviator of the fabric tensor and the inclination of the major principal axis respectively indicate the degree of the fabric anisotropy and the fabric rotation. In the simple shear test, Oda et al. (1982) discovered that the rotation of principal axes of stress tensor tended to be coaxial to that of the fabric tensor  $H_{ij}$ . Following the coaxiality between stress tensor and fabric tensor, Mehrabadi et al. (1982) derived a stress-fabric relation by defining the stress in terms of fabric invariants, expressed as below,

$$\sigma_{ij} = \alpha H_{ij} + \beta H_{kl} H_{lk}, \quad (1.2)$$

where  $\alpha$  and  $\beta$  are material parameters. In the aspect of building the stress-fabric relation, Bathurst and Rothenburg (1990); Quadfel and Rothenburg (2001) proposed stress-fabric formulas respectively in assemblies of spherical and ellipsoidal particles.

Ken-Ichi (1984) proposed to approximate the contact orientational density distribution by the Fourier extension with items more than second order truncated. The formula for 3D data was expressed as below,

$$E(\theta, \beta) = \frac{1}{4\pi} \left[ 1 + \frac{a}{4} (3 \cos 2\theta + 1) + 3b \sin^2 \theta \cos 2\beta \right], \quad (1.3)$$

where  $a$  and  $b$  are two parameters. This formula can be alternatively written in a form involving Cartesian tensor:

$$\begin{aligned}
 E(\theta, \beta) &= D_{ij}n_i n_j, \\
 \overline{\overline{D}} &= \frac{1}{4\pi} \begin{bmatrix} 1+a & 0 & 0 \\ 0 & 1-a/2+3b & 0 \\ 0 & 0 & 1-a/2-3b \end{bmatrix}, \\
 \vec{n} &= \cos\theta \vec{i} + \sin\theta \cos\beta \vec{j} + \sin\theta \sin\beta \vec{k},
 \end{aligned} \tag{1.4}$$

where  $\vec{n}$  is the contact normal. The 2D data's formula was also given,

$$E(\theta) = \frac{1}{2\pi}(1 + a \cos 2\theta), \tag{1.5}$$

where  $a$  is an adjustable parameter. The associated tensor in Cartesian coordinate system  $\overline{\overline{D}}$  were expressed as follows,

$$\begin{aligned}
 E(\theta) &= D_{ij}n_i n_j, \\
 \overline{\overline{D}} &= \frac{1}{2\pi} \begin{bmatrix} 1+a & 0 \\ 0 & 1-a \end{bmatrix}, \\
 \vec{n} &= \cos\theta \vec{i} + \sin\theta \vec{j},
 \end{aligned} \tag{1.6}$$

This method is commonly adopted to approximate the contact orientational distribution, because there are only a few number of parameters and the error is relatively small. In a similar form, the contact force distribution (a characterization of force fabric) can be also approximately characterized, such as in 2D case (Cambou, 1993),

$$\begin{aligned}
 f_n(\theta) &= \bar{f}(1 + a_n \cos 2\theta), \\
 f_t(\theta) &= -\bar{f} a_t \sin 2\theta,
 \end{aligned} \tag{1.7}$$

where  $f_n(\theta)$  and  $f_t(\theta)$  are respectively the normal and the tangential force on contacts along the direction indicated by inclination  $\theta$ , and  $\bar{f}$  is the mean normal force over all contacts.

Rothenburg and Bathurst (1989) investigated the evolution of the material fabric and the force fabric in the 2D biaxial test, the material fabric parameter  $a$  and force parameters  $a_n$  and  $a_t$  are traced during loading. A relation between deviatoric stress and these fabric parameters was theoretically derived and then experimentally proven, as given below,

$$\frac{\sigma_1 - \sigma_2}{\sigma_1 + \sigma_2} = \frac{1}{2}(a + a_n + a_t), \quad (1.8)$$

where  $\sigma_1$  and  $\sigma_2$  are respectively the axial and the lateral stress eigenvalues. Azéma et al. (2007), in the 2D numerical biaxial test on the pentagons assembly, also investigated the evolution of  $a$ ,  $a_n$  and  $a_t$  and examined the equation 1.8. Their Results supported the equation 1.8.

In aforementioned investigations, interests were only placed on expressing the stress quantities in terms of fabric parameters. The knowledge in the aspect of how the strain is related to the fabric evolution remains limited. However, this is crucial for obtaining sound constitutive relations. There are two questions needing to be answered: how the global strain directs the fabric evolution; and how the global strain is derived from the deformations on material fabric.

Calvetti et al. (1997) investigated the first point based on the results from the shear test on 2D assemblies of rods. The evolution of the material fabric was investigated in different kind of shear tests, with an emphasis on comparing the variations of contact numbers in different directions. Results showed that contacts were preferentially created in contractant directions and destructed in the dilatant ones. Then the following formula was given,

$$\frac{\delta\omega(\vec{n})}{\omega(\vec{n})} = a(\delta\bar{\varepsilon} : \vec{n}) \cdot \vec{n}, \quad (1.9)$$

where  $a$  is an adjustable coefficient for different materials,  $\vec{n}$  is the contact normal indicating the contact direction.

However, all methods above in describing material fabric are incompetent of solving the second point, because in these methods, contacts are considered independently in the orientational distribution (or function), presenting no organization and relative displacement among each other. Whereas the strain in granular assemblies is derived from the relative displacement not only between contacting grains but also among neighboring contacts. This means that the strain should be derived in a scale competent of characterizing the organization among contacts, in the other word, a scale larger than single contact scale. On the other side, as far as the force fabric was exploited, scientists gradually realized that the force transmission in the granular material also presents an

organization in a scale much larger than the single contact scale. This is the force-chains, which will be mentioned in next subsection. It is far from possible to correctly formulate the evolution of the force fabric only in a orientational function. Therefore, both material and force fabric are required to be investigated in a scale larger than the single contact scale but, of course, smaller than the macro-scale, i.e. the so-called meso-scale. In this meso-scale, force-chains and meso-loops (will be introduced later) can be identified, as ways of characterizing respectively the force fabric and the material fabric.

### 1.2.1.2 Structures in a meso-scale

#### Force-chains

Due to the disordered packing, forces in granular media are transmitted in a prominent heterogeneity pattern (Cambou et al., 2009). This phenomenon was first noticed in several investigations of the shearing test on the photoelastic material (Dantu, 1968; Drescher and De Jong, 1972). In a similar scene as in Figure 1.1, forces were observed not to distribute homogeneously in the material but to follow some column-like paths which formed a structural network, showing a pronouncedly more heterogeneous and anisotropic pattern than that of the material fabric. This material feature was not further investigated until the middle of 1990s. Jaeger et al. (1996) investigated the forces particles applied on the boundaries in a triaxial test through measuring prints of particles on the carbon paper set on the boundaries. A decreasing exponential density distribution of force magnitude was found.

Radjai and Roux (1995); Radjai et al. (1998) distinguished between strong force network and weak one according to the average force, and investigated the organization of these two networks. The exponential density distribution was observed to only exist in strong network, while the weak network (complementary to strong network) distributed in a uniform or power-law shape (Radjai et al., 1996; Mueth et al., 1998). Further researches confirmed the exponential density distribution to be a prevailing feature of granular material subjected to the external loading, as properties of weak network were shown to be sensitive to the grain size distribution and the initial state (Mueth et al., 1998; Radjai et al., 1999; Antony, 2000; Blair et al., 2001; Erikson et al., 2002; Silbert et al., 2002; Mueggenburg et al., 2002; Majmudar and Behringer, 2005; Azéma et al., 2007). More generally saying, the existence of a persistent heterogeneous force distribution can be the definition of the solid phase of the granular material, being distinct from the fluid

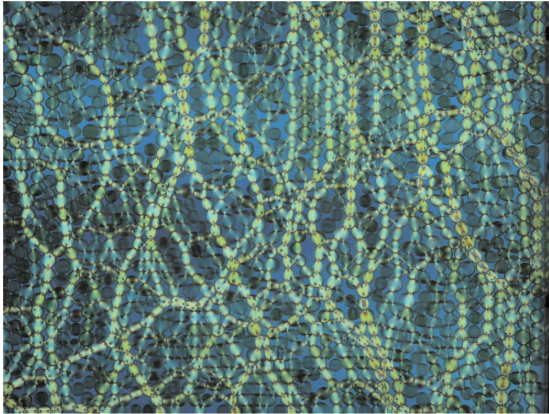


*Figure 1.1: Force fabric in the granular assembly made up of photoelastic material, in a simple shear test. The brightness of light lines presents the force magnitude (Zhang et al., 2008).*

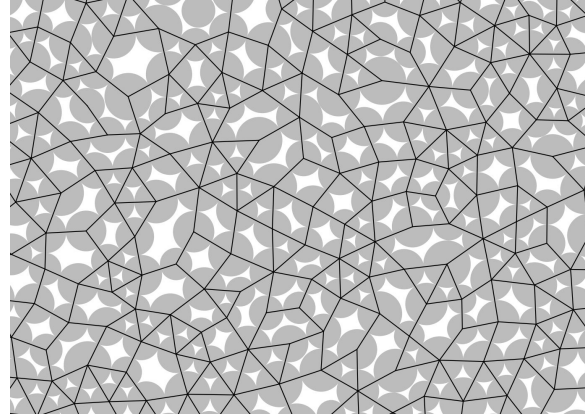


*Figure 1.2: Contact network composed of contact branches in the 2D granular assembly. Black continuous lines are contact branches, gray disks are grains.*

and gas phases, where heterogeneities cannot be long-lasting (Jaeger et al., 1996). In later researches, the jamming transition, a concept similar to the phase transition, was observed to be highly associated to the formation of the heterogeneous force distribution (Behringer et al., 2008; Kondic et al., 2012).

In this context, the strong network is distinguished from the weak network, then the concept of force-chain was prepared on the basis of the strong network to define those quasi-linear columns, consisting of contacts of the force magnitude greater than the average.

Further investigations have shown the significant role the force-chain plays in the macroscopic behaviors of the granular material. Iwashita and Oda (2000); Oda and Iwashita (2000), in numerical biaxial tests with the particle rolling resistance, investigated micro-scale properties of granular assemblies with shear bands. They noticed the formation of shear bands strongly referred to the massive generation of force-chains during the hardening process and their collapse in the softening process, accompanied with a volumetric dilatancy. Based on results of the numerical biaxial test, Tordesillas (2007) analyzed the evolution of the void ratio around force-chains and the damage pattern of force-chain. Some evidences about the link between force-chains and stress-dilatancy were found. This intriguing work shed a light to answer the question that how the volumetric variation on the material fabric influences the force fabric evolution. However, a

reasonable answer requires a more precise investigation on how force-chains and their surrounding structures interact with each other. A priori, force-chains' surrounding fabric should be characterized in a clear way with physical meanings. The meso-loop, which will be introduced in the following, provides a promising way in this aspect.

### **Meso-loops**

Satake (1992) introduced an approach to associate discrete mechanical properties to the continuum-mechanical ones. In this approach, as shown in Figure 1.2, the contact network seamlessly tessellates the material area into loops, which are enclosed by contact branches and involve inside fan-shaped sections of particles and voids surround by particles. Therefore, voids can be correctly quantified inside loops by local kinematical properties. This approach gave a way of characterizing the material fabric by considering the microscopic volumetric nature in the scale of the loop, namely a meso-scale. Then the loop can be also called the meso-loop.

Bagi (1993, 1996); Nguyen et al. (2012) expressed the stress on the meso-scale as a volume average of the tensorial product of the contact forces and the contact branches. This way of defining the meso-scale stress was satisfying only in the static or quasi-static state, otherwise, an inertial term should be involved according to the expression given by Nicot et al. (2013). Bagi (1993, 1996); Kruyt and Rothenburg (1996); Cambou et al. (2000); Kruyt (2003) proposed several approaches to derive the average strain of the material from relative displacements on contacts and geometrical quantities of loops. Results proved that the global strain can be well presented from the local kinematics of the meso-loops. Nguyen et al. (2009, 2012) gave a definition of the strain on the meso-loop. This meso-scale strain facilitates researchers to make the analysis on the meso-scale, by characterizing the meso-scale kinematics into a continuum-mechanical form which researchers are familiar with.

### **Problems in the meso-structure investigation**

There are two problems on the fabric investigation in the meso-scale, which have to be stated here and need to be investigated in this thesis:

1. As a way of describing the material fabric, the meso-scale topology and its evolution give important information of the granular system. [Kruyt and Rothenburg \(2014\)](#) statistically analyzed the critical state features of meso-loops in several aspects. Results showed that in critical state, the loops' geometrical anisotropy was highly depending on the side number and the orientation of loops. [Arévalo et al. \(2010\)](#) investigated the evolution of the topology of a polydispersing granular assembly subjected to an isotropic compression. The number of triangles, the meso-loop with three sides, increased substantially at the transition point from the dynamic state to the static state, and kept increasing afterwards. The result suggested that triangles played a special role in the transition between the dynamic to the static state.

Meso-loops in different shapes or inclined in different orientations present the prominently distinction on the micro-mechanical behavior. Therefore, data such as the proportion of meso-loops in different shapes or the preferring inclination of meso-loops are also physically meaningful to the granular system, and can be strongly associated to the material's macroscopic behavior. This is a promising way to attribute material's macroscopic behavior to the topology of its fabric. However, only a few of researches has been dedicated to this direction ([Arévalo et al., 2010](#); [Kruyt and Rothenburg, 2014](#)).

2. In another aspect, a fundamental problem in the micro-structure investigation of the granular material is how the force fabric (force-chains) and the material fabric (meso-loops) interact with each other. When force-chains and meso-loops are correspondingly the local static and kinematical elements in the granular material, the interplay between them appears to be the basic ingredient of the local constitutive behavior. The observation and formulation on this behavior will give birth to the local constitutive relation. [Tordesillas et al. \(2010, 2014\)](#) investigated the evolution of the surrounding meso-loops around force-chains. Triangles associated to force-chains were observed to substantially depopulate and transform to meso-loops with a larger side number. This may contribute to the volumetric dilatancy. The way how triangles were transformed to other ones was discussed. However, even though pioneering works have been done, knowledge on this aspect is still very limited.

### 1.2.2 Constitutive modeling based on the fabric

As the knowledge in terms of the micro-structure of the granular material was approaching the physical essence, scientists started to attempt building the constitutive relation with micro-mechanical considerations. One kind of approach derives the constitutive relation still in a phenomenological framework, such as in an elasto-plastic framework, but with considering the role of the fabric by embedding fabric-related parameters into the formulations. [Li and Dafalias \(2012\)](#) extended the critical state theory ([Schofield and Wroth, 1968](#)) by an additional requirement to a constant fabric in the critical state, other than the conventional requirement to the constant stress and volumetric strain. Following this way, several studies ([Zhao and Guo, 2013](#); [Guo and Zhao, 2013](#)) dedicated to investigate the critical state fabric anisotropy. The critical state relation between the fabric anisotropy parameters and the hydrostatic pressure was given. Several constitutive relations ([Gao and Zhao, 2012](#); [Gao et al., 2014](#)) were built on the basis of this framework by involving fabric anisotropy parameters. This kind of approach only adjusted the phenomenological framework by considering some parameters which have micro-physical meaning. However, the macroscopic quantities were derived not from their microscopic essences but still from empirical relations.

On the contrary, the multi-scale approach uses changing scale techniques to sophisticatedly relate the macroscopic quantities to the static and kinematic aspect of the fabric. [Chang and Misra \(1989\)](#); [Chang et al. \(1992\)](#), in their pioneering work, built a constitutive model for sand. In this model, incremental stress and strain are respectively connected to the contact force and the contact relative displacement on the basis of the contact fabric distribution  $E(\theta, \beta)$ , which was initially given. After that, various constitutive models ([Chang et al., 1990](#); [Yin et al., 2011b,a](#); [Chang, 2014](#)) were born for different kinds of soil, in similar methods as what was proposed by [Chang and Misra \(1989\)](#); [Chang et al. \(1992\)](#). The difference only lied in the form of the initial density distribution for the contact fabric. [Nicot et al. \(2005\)](#) adopted the fabric evolution law (equation 1.9) given by [Calvetti et al. \(1997\)](#) into the constitutive relation, in order to solve the fabric evolution in terms of the incremental strain during the loading path. [Emeriault and Cambou \(1996\)](#) clarified the general framework of deriving the constitutive relation for the granular material, involving three parts: the strain localization (or averaging) scheme, to determine the local kinematical quantities from the global strain (or reverse); the local constitutive relation, to give the local static quantities according to local kinematic quantities (or reverse); and the stress averaging (or localization) scheme, to solve the global stress from local

quantities (or reverse). In this work, representation theorem ([Spencer, 1987](#)) was applied to formulate the relation between the local kinematics and the global strain. Combining with the stress homogenization scheme, a micro-mechanical model was derived from a non-linear elastic model, the Hertz-Mindlin model ([R. D. Mindlin, 1953](#)).

### Problems in multi-scale constitutive modeling

As we already know, both the force and material fabric only exist in the meso-scale and above, any smaller scale will blind us to capture intact force and material fabrics, much less to completely characterize the local behavior between these two fabrics. This means that the local constitutive relation can be only derived on the meso-scale. Given that the techniques of obtaining the stress and the strain respectively from the force fabric and loops' kinematics are getting mature, to obtain a satisfying local constitutive relation in the meso-scale is the only missing link to build a sound constitutive model. [Nicot and Darve \(2011b\)](#) built a constitutive relation by introducing hexagons, instead of individual contacts, as elements of the fabric. These hexagons, consisting of six contacts symmetrically forming a loop, were an embodiment of the meso-loop, namely, an entity in the meso-scale allowing the relative displacement among contacts to be presented. However, this was only the first attempt to derive the constitutive relation from the meso-scale, there were still numerous significant details missed, mainly in three aspects: the symmetric layout of the hexagon disables the model to receive a shear strain; the force fabric is not presented, any force-chain related element has not been considered; and the evolution of the angular distribution of hexagons has not been fully considered.

## 1.3 Objectives

To build a constitutive model which is competent of simulating the complex behavior of the soil requires a comprehensive observation, an accurate perception and then a sophisticated formulation on the microscopic essence of the macroscopic appearance. On one side, new observations on the fabric of the granular material have highlighted the significance of the meso-scale and suggested a bright perspective of constitutive modeling in the meso-scale. However, on the other side, progressing along this road is largely hindered by the limited knowledge on the fabric behavior of the granular material in the meso-scale. The aim of this thesis is to build a constitutive model on the basis of the knowledge obtained from the investigation to the mesoscopic mechanical

behavior of the granular material. This aim can be divided into two steps: based on the results of the numerical simulation using DEM (discrete element method), to investigate the mechanical behavior of force-chains and meso-loops (their evolution, mutual interaction and their role in macroscopic mechanical behavior), as a cumulation of the micro-mechanical knowledge for further constitutive modeling; and to develop a constitutive model using multi-scale approach on the basis of the knowledge obtained from the first step. These two steps are detailed as below.

### **Micro-structure analysis in 2D granular material**

The objective of the micro-structure analysis can be subdivided into three parts. All analysis is based on the results of numerical simulations using DEM.

The first part is to investigate the evolution of some significant features of meso-loops along the drained biaxial test from different initial states. In this part, basic evolutionary characteristics of the material fabric characterized by meso-loops will be quantitatively investigated, the degree and the way the evolution of meso-loops influences the macroscopic mechanical behavior of the granular material need to be clarified.

The second part is to investigate the interaction between force-chains and their confining meso-loops along drained biaxial loading path. The aim is to specify two points: how the force-chains (the force fabric) rebuild their surrounding meso-loops (the material fabric) during loading path; and how the latter influences the behavior of the former.

The last part is to characterize the critical state fabric on the meso-scale of granular material in both localized and diffuse failure modes. In this part, features of the meso-structure in the critical state will be investigated, aiming to find an identical meso-structure in the failure area of the granular assemblies, which are undergoing either localized or diffuse failure.

### **Constitutive modeling using a multi-scale approach**

In constitutive modeling, the objective lies in two sides: (1) to modify the H-directional model (Nicot and Darve, 2011b) by breaking the axis-symmetric configuration of the hexagon and enabling the model to work under the shear strain, and then testify this extended model; (2) to give suggestions for further extending the model on the basis of the knowledge obtained from the micro-structure investigations.

## 1.4 Outline of this thesis

The work of the thesis is organized as below:

In the chapter 1, a general introduction is given for the thesis. The importance to study the granular soil behavior and the necessity to make the micro-mechanical investigation and to build the constitutive model for granular material are emphasized at the beginning. Then the history of the micro-mechanical research and the constitutive modeling using multi-scale approach is introduced by highlighting some important contributions in these two aspects. The necessity to introduce the meso-scale and meso-structures in both the micro-mechanical investigation and the constitutive modeling is claimed. Limitations and problems in existing researches or methods are discussed. At the end, the objectives and plan of this thesis are described

In the chapter 2, DEM is employed to implement numerical test of the granular material. At first, a brief introduction to the discrete element method is given, involving the key procedures in the computation of DEM and some basic formulas. Then as a preparation for the micro-mechanical investigation of the granular material in the chapter 3, numerical biaxial tests using DEM are performed. The procedure and parameters of these tests are specified.

In the chapter 3, the meso-structures and the role they play on the mechanical behavior of the granular material are investigated. Three key questions are answered: how force-chains and meso-loops evolve; how these two kinds of meso-structure interplay with each other; how the evolution and interaction of meso-structures lead to some significant behaviors on the macro-scale. At first, some basic micro-mechanical concepts are described, involving the definition of two significant meso-structures, the meso-loop and the force-chain. Then based on results of numerical tests, micro-structure analyses are implemented from three aspects. A priori, the general evolution pattern of the meso-loops and its connection to the volumetric behavior are investigated. Then the interaction between the force-chains and the meso-loops and how it leads to the volumetric dilatancy are investigated. Finally, the micro-structure basis of the critical state mechanics in localized and diffuse failure modes is studied. All presented investigations in this chapter are based on 2D simulations using DEM.

In the chapter 4, the modified H-directional model, a model developed in the framework of multi-scale approaches, is proposed in extension of the H-directional model (Nicot and Darve, 2011b). A review is first given on the H-directional model and its predecessor, the micro-directional model (Nicot et al., 2005). The evolution of these two

preceding constitutive models is described and their drawbacks are discussed. Then the H-directional model is modified in terms of its shortcoming, giving birth to the modified H-directional model. This modified model is, subsequently, validated. At the end, several ways for further extending the H-directional model are suggested on the basis of the knowledge obtained from chapter 3. The framework to insert the triangle elements into the model is given.

In the last chapter, the main conclusions of this thesis are summarized, followed by comments on open issues and prospectives for future developments.

## 1.5 Conclusion

In the discussion of this chapter, the importance on the topic of the thesis and the necessity to investigate the meso-structures and build the constitutive model on the basis of the meso-scale were explained. Then main objectives and the plan of the thesis are described. Main points in this chapter are summarized as below.

Both the force and material fabric are highlighted, as playing a fundamental role in material's macroscopic behavior. Accurately characterizing and formulating these two fabrics and the interaction between them are essential tasks to build a constitutive model capable of simulating the complex behaviors of granular materials. Meanwhile, these two fabrics exist in the meso-scale and can be respectively characterized in the form of the force-chains and the meso-loops. The constitutive relation, therefore, should be only derived on the meso-scale. This brings two objectives to which the thesis will dedicate: to investigate the behavior of the granular material on the meso-scale, especially the evolution of force-chains and meso-loops, the interaction between them and the roles they play in the macroscopic mechanical properties of the granular material; and to develop a constitutive relation accounting for the fabric evolution in the meso-scale.

## Chapter 2

# Numerical Modeling by Discrete Element Method

All Materials in small enough scales are composed of discrete elements, which are separated by space. For example, in gases, liquids and solids, as they are made up of atoms, an atomic scale can be identified; the soil consists of soil grains, rock and concrete have fractures, then corresponding micro-scales can be distinguished with respect to the scale of the discontinuity. In the application of simulating materials, to avoid solving interactions and kinematic equations of every discrete element, a continuum assumption should be made in a rational scale, over which the material can be seen as continuous and a value can be measured representatively to the whole. This scale is the representative elementary volume (*REV*), defined by the Hill-Mandel condition (Hill, 1963; Ostoja-Starzewski, 2007). In a scale bigger than *REV*, called macro-scale, representative mechanical quantities, such as the stress and the strain, can be measured by the experiment and then correlated with each other by a constitutive model, while the continuum mechanics is adopted. In a scale smaller than *REV*, the randomness, due to the existence of the discontinuity, may come to an effect on the mechanical quantities. Despite there is a random texture, however, a periodicity may be identified or statistical homogeneity and ergodicity of the micro-structure may be valid, enabling a homogenization from microscopic properties to macroscopic ones. This gives rise to a better understanding the mechanisms beneath the constitutive behavior of the material, and gives us the opportunity to build a constitutive model more realistic and more obedient to the micro-mechanical essence.

In this thesis, to build the constitutive model of the granular material on the micro-mechanical basis requires scales smaller than  $REV$ , where the material is considered as an assembly of discrete elements. Consequently, the discrete element method  $DEM$  should be employed to calculate motions and interactions of discrete elements. In this chapter, general knowledge and some key formulas in  $DEM$  are introduced in section 2.1. As a preparation for the micro-mechanical investigation of the granular material, a numerical biaxial test using  $DEM$  is mentioned in section 2.2 in terms of the procedure and parameters used in the test.

## 2.1 Introduction of discrete element method

Discrete Element Method ( $DEM$ ), developed by Cundall (1971) and later improved by Cundall and Strack (1979), is a best known and well-developed numeral method to calculate motions and interactions of a set of discrete elements. With increasingly powerful computing capability,  $DEM$  becomes widely accepted as an effective and efficient method to solve mechanical problems. Many extensions have been made in order to tackle different mechanical situations: for calculating the continuum deformation inside elements, methods coupling with finite element method ( $DEM-FEM$ ) have been proposed Itasca and Code (2011); Mahabadi et al. (2012, 2014,?); in terms of fluid-solid coupling,  $DEM$  has been coupled with Lattice Boltzmann Method ( $LBM$ ) (Ladd, 1994a,b; Ladd and Verberg, 2001; Feng and Michaelides, 2004; Feng et al., 2007, 2010; Leonardi et al., 2012a,b) and Computational Fluid Dynamics ( $CFD$ ) (Tsuji et al., 1993; Xu and Yu, 1997; Kawaguchi et al., 1998; Kafui et al., 2002). The range of the  $DEM$  application has been expanded to involve more and more physical and engineering procedures, making it a big family of methods and a reliable tool to simulate the reality.

In  $DEM$ , the entire information of a complex system is expressed by no more than interaction and element motion quantities. Moreover, following a certain homogenization scheme, these local quantities can be averaged, to link to corresponding macro-scale quantities. In this way, the link between the micro-scale and the macro-scale behavior is established. Then, how a macroscopic phenomena derives from microscopic events or properties and how a microscopic parameter affects the macroscopic behavior can be analytically investigated. Consequently,  $DEM$  becomes not only an engineering simulator, but also a powerful scientific tool, allowing researchers to explore the micro-mechanical characteristics of the material.

Before adopting this method, it is necessary to be aware of its limitations, basically existing in two aspects:

- Due to the contact detecting procedure, the simulation duration is almost exponentially increasing with the number of elements, inducing a large limitation by the power of the computational processor. Many attempts have achieved to cut the computing duration, involving the improvement of the contact detecting algorithm (Hubbard, 1996; Jung and Gupta, 1996; Klosowski et al., 1998; Munjiza and Andrews, 1998), multi-processor parallel computation (Battenberg and Wessel, 2009; Munjiza and Cleary, 2009; Shigeto and Sakai, 2011; Xu et al., 2012) and Graphics Processing Unit (*GPU*) parallel computation (Nishiura and Sakaguchi, 2011; Washizawa and Nakahara, 2013). Even though there are achievements in this aspect, it is far from being mature and widely spread;
- For a material simulated by *DEM*, global parameters of the material cannot directly derive from local parameters of elements. This may turn to a time-consuming calibration between the numerical and the experimental model.

Methods of solving the dynamics of discrete bodies involve two families: contact dynamics (Jean, 1999; Brogliato and Acary, 2008; Brogliato, 2012) and molecular dynamics (Streett et al., 1978; Tuckerman et al., 1992; Smith, 2005). In the contact dynamics, the discrete system consists of rigid bodies, which is governed by the purely frictional interactions on contacts and mathematically solved by the non-smooth mechanics theory. In the molecular dynamics, the interaction among discrete bodies, either the rigid or the soft ones, is defined by a force field constituted by contacting or non-contacting forces (Cundall and Strack, 1979; Wei-Xin Ren, 1999; Debunne et al., 2000; Johnson and Holzapfel, 2003; Heard, 2008). *DEM* belongs to the molecular dynamics where the force field is constituted by contact forces, which have an elastic or elasto-plastic nature. It is the application of the molecular dynamics to granular materials. In this thesis, *DEM* is adopted, which will be introduced in the remaining part of this section.

### 2.1.1 Calculation cycle

For the molecular dynamics approach, the objective of *DEM* is to determine contact forces and particle motions of each particle in a duration  $\Delta t$ . At the initiation of a time step  $t_0$ , positions and velocities of all particles at time  $t_0$  are known. Contact forces during time step  $[t_0, t_0 + \Delta t]$  and positions and velocities of all particles at the end of this time step  $t = t_0 + \Delta t$  are determined in following 4 steps:

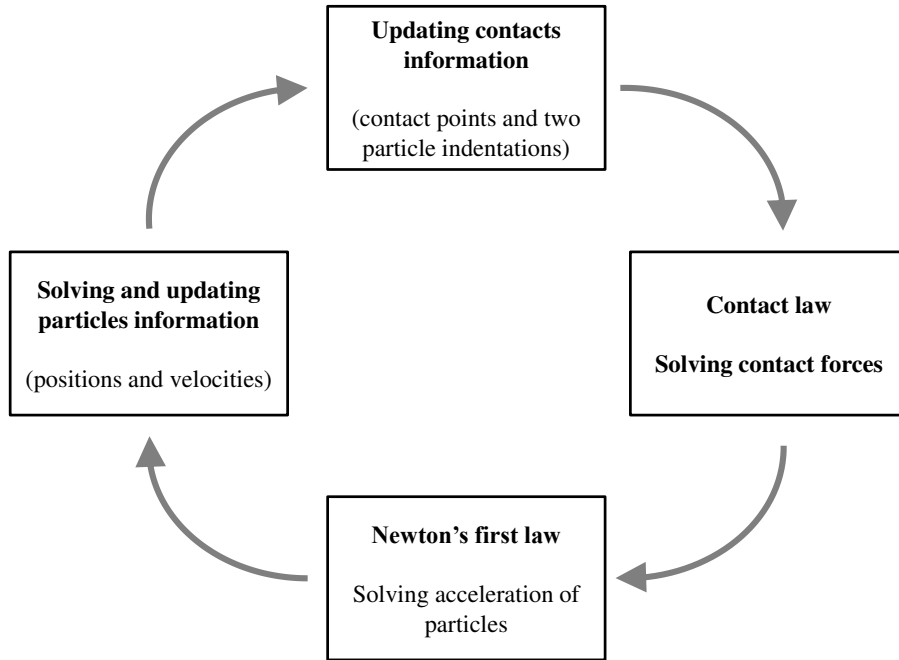


*Figure 2.1: Calculation cycle of DEM.*

- Updating contacts and their corresponding indentations of particles at  $t_0$ , according to particle's positions at  $t_0$ ;
- Calculating and storing all contact forces from the indentations calculated in step 1, by applying the contact law;
- Integrating all applied contact forces of each particle, and calculating the acceleration of them according to Newton's second law;
- Calculating and updating positions and velocities of all particles by integrate the acceleration during  $\Delta t$ .

Then the particle positions and velocities at the end of this time step turn to the initial variables of the next time step. The circulation therefore can repeat and continue under control, as shown in Figure 2.1.

### 2.1.2 Contact law

The macroscopic behavior of the medium modeled by *DEM* is largely dependent on the local mechanical behavior of particles. The local behavior is described through the contact law, a relation between the contact force and the relative displacement between two particles in the contact.

The contact law can be abstracted as a function, in which the contact force ( $\vec{F}$ ) is determined by the relative position between two particles in the contact  $\vec{u}$  and the relative velocity between them  $\dot{\vec{u}}$

$$\vec{F} = f(\vec{u}, \dot{\vec{u}}). \quad (2.1)$$

For models uncoupling normal and tangential behaviors, normal and tangential forces ( $F_n$  and  $F_t$ ) are given by

$$\begin{aligned} F_n &= f_n(u_n, \dot{u}_n), \\ F_t &= f_t(u_t, \dot{u}_t), \end{aligned} \quad (2.2)$$

where subscripts  $n$  and  $t$  denote normal and tangential directions.

The most common contact law used in *DEM* is the elasto-frictional law, introduced by [Cundall and Strack \(1979\)](#). It assumes that when a contact occurs, fictitious linear springs with friction coming into effect, with one spring in the normal direction to the contact plane (stiffness  $k_n$ ) and another spring in the tangential direction to the contact plane (stiffness  $k_t$ ), as shown in Figure 2.2a. The friction is an ideal one of the friction angle  $\varphi$ , the tangential behavior of the contact is plotted in Figure 2.2b. These components maintain valid until two particles in the contact are apart. No tensile force is allowed in the normal direction. As a result, this local elasto-frictional behavior will lead to a global elasto-plastic behavior of the material.

The incremental form of normal and tangential behaviors is expressed by

$$\begin{aligned} dF_n &= k_n \cdot du_n & \text{and} & & F_n > 0, \\ dF_t &= k_t \cdot du_t & \text{and} & & |F_t| \leq F_n \cdot \tan(\varphi), \end{aligned} \quad (2.3)$$

where  $k_n$  and  $k_t$  are respectively normal and tangential contact elastic moduli.

To maintain the condition  $|F_t| \leq F_n \cdot \tan(\varphi)$ , there is a test scheme in every time step. A correction will be added on  $F_t$ , once the condition is violated.

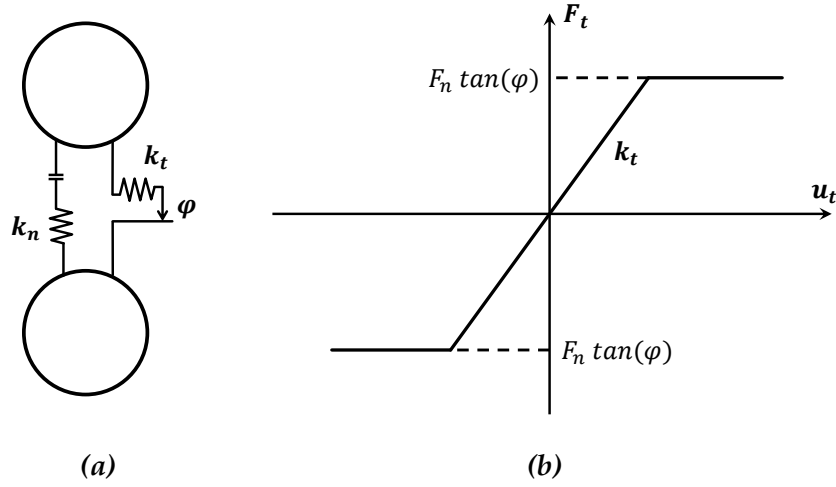


**Figure 2.2:** Elasto-frictional contact law: (a) components in the contact; (b) elasto-frictional behavior in the tangential direction.

Practically, contact elastic moduli are determined by the stiffness of two particles,

$$k_n = \frac{k_n^i k_n^j}{k_n^i + k_n^j}, \quad (2.4)$$

$$k_t = \frac{k_t^i k_t^j}{k_t^i + k_t^j}$$

Superscript  $i$  and  $j$  denote the ID of particles.

### 2.1.3 Calculation of the particle displacement

When the integral force  $F_i$  and the integral moment  $M_i$  are known, the acceleration on the particle center  $\ddot{x}$  and the angular acceleration  $\ddot{\omega}$  are solved by the Newton's second law

$$\ddot{x}_i = \frac{F_i}{m}, \quad (2.5)$$

$$\ddot{\omega}_i = \frac{M_i}{J},$$

where  $m$  and  $J$  are respectively the mass and the moment of inertia of the particle. For spherical element, the latter is equal to  $2mR^2/5$ .

Following the mid-point loading scheme,  $\ddot{x}_i$  and  $\ddot{\omega}_i$  are assumed to be constant during the time interval  $[t - \frac{\Delta t}{2}, t + \frac{\Delta t}{2}]$ . Then the translational and angular velocity  $\dot{x}_i$  and  $\dot{\omega}_i$  are determined by

$$\begin{aligned}\dot{x}_i^{t+\frac{\Delta t}{2}} &= \dot{x}_i^{t-\frac{\Delta t}{2}} + \ddot{x}_i^t \Delta t, \\ \dot{\omega}_i^{t+\frac{\Delta t}{2}} &= \dot{\omega}_i^{t-\frac{\Delta t}{2}} + \ddot{\omega}_i^t \Delta t.\end{aligned}\tag{2.6}$$

$\dot{x}_i$  and  $\dot{\omega}_i$  are assumed to be constant during the time interval  $[t, t + \Delta t]$ . Then the translational and angular displacement  $x_i$  and  $\omega_i$  at time  $t + \Delta t$  are given by

$$\begin{aligned}x_i^{t+\Delta t} &= x_i^t + \dot{x}_i^{t+\frac{\Delta t}{2}} \Delta t, \\ \omega_i^{t+\Delta t} &= \omega_i^t + \dot{\omega}_i^{t+\frac{\Delta t}{2}} \Delta t.\end{aligned}\tag{2.7}$$

Then the particle position at time  $t + \Delta t$  can be updated. Meanwhile, translational and angular velocities at the middle time point  $t + \frac{\Delta t}{2}$  are stored for the calculation in the next time step.

### 2.1.4 Computational stability condition

The computational stability is an important consideration in *DEM* simulation. In a stable computation, the error is bounded and controlled, ensuring a stable result. On the contrary, the non-stability leads to an unboundedly propagation of error, while errors amplifyingly cumulate without control step by step, resulting in a strong unstable outcome. In most algorithms of *DEM*, an explicit scheme is adopted, where the stability of the computation is conditional to the length of the time step  $\Delta t$ .

The admitted  $\Delta t$  to a stable solution, called critical time step  $\Delta t_c$ , is dependent on the time of the wave propagation in the medium. The granular system modeled in *DEM* is comprised of finite elements and springs. For a particle, which has a mass  $m$  and is connected with other particles via springs of the stiffness  $k$ , the characteristic oscillation period  $T$  is equal to  $2\pi\sqrt{\frac{m}{k}}$ . Then the critical time step  $\Delta t_c$  of the whole granular system must be strictly less than the minimum characteristic period over all particles.

Taking the rotation into account,  $\Delta t_c$  is estimated to be proportional to the min value between the translational time step  $\Delta t_c^T$  and rotational time step  $\Delta t_c^R$ , expressed as follow:

$$\Delta t_c = C_t \min(\Delta t_c^T, \Delta t_c^R) = 2\pi C_t \min\left(\sqrt{\frac{m}{k_n}}, \sqrt{\frac{J}{k_r}}\right),\tag{2.8}$$

where  $k_n$  and  $k_r$  are respectively the normal and the rotational stiffness of particles.

### 2.1.5 Yade-DEM software

The *Yade-DEM* software (Šmilauer and Chareyre, 2010; Šmilauer et al., 2010a,b) is used to implement *DEM* numerical simulations in the work of this thesis.

Yade is a extensible open-source *DEM* code, developed in C++. This project is initiated by Kozicki and Donzé (2008, 2009) and on the basis of the molecular dynamic code *SDEC* (Spherical Discrete Element Code), (Donzé and Magnier, 1997). It is programmed in an objective oriented platform allowing users to modify and extend.

*Python* is used as the operation environment in *Yade*. Gifted with advantages of an interpreted language, *Python* environment features *Yade* a great facility in terms of simulation control, post-processing, data mining and data analysis. Especially, the convenience on inquiring particles and interactions relevant variables largely simplifies the data mining process in this thesis.

## 2.2 Biaxial tests in DEM

In this section, a series of numerical drained biaxial tests using *DEM* are performed. The drained biaxial test is an usual loading path engineers often come across in the practice. In this loading path, the stress and the volume of the material can increase and decrease, giving a diverse variation on the micro-structure. All tests are implemented by the open-source *DEM* code *Yade* software. The protocol of the tests is introduced in the following subsections.

### 2.2.1 Parameters

To clarify the basic evolution pattern of the micro-structure requires a simple model with the number of factors constrained as few as possible. Then an elastic-friction law is adopted; the interaction between two contacting particles incorporates normal and tangential springs with respective stiffness  $k_n$  and  $k_t$ . Non-cohesive friction comes into effect when slide occurs,  $\varphi$  denotes the inter-particle friction angle.

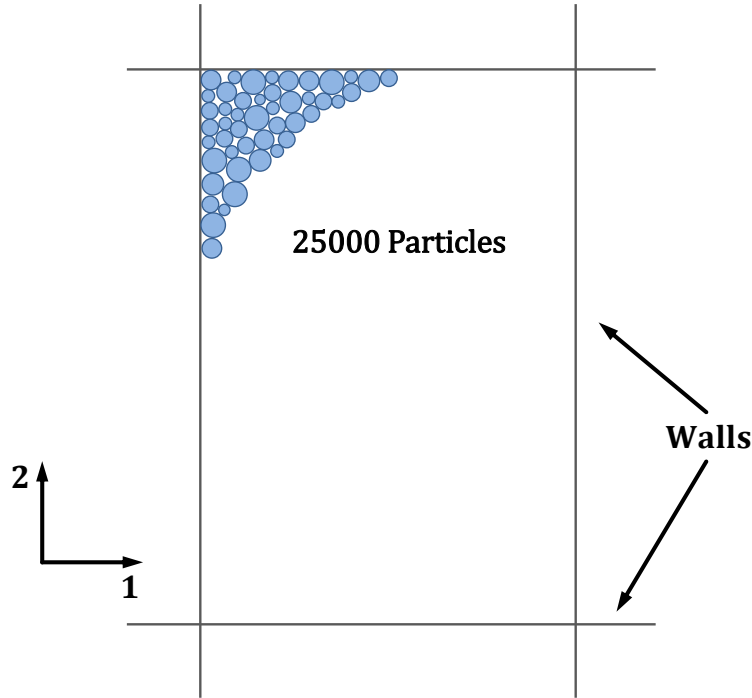


Figure 2.3: Biaxial test model in DEM.

In granular assemblies, the occurrence of the crystallization compels particles to form an uniform crystallizing pattern, dispelling the micro-structure diversity and the disordered grains packing. To avoid it, particles are randomly generated, with radii obeying an uniform distribution, dispersing from  $0.75D_{50}$  to  $1.25D_{50}$ , where  $D_{50}$  is the mean grain radius.

As illustrated in Figure 2.3, all particles are ranged in a frame of frictionless walls as height  $h = 1.35$  m, width  $w = 0.9$  m. *Axis-2* and *axis-1* respectively refer to axial and lateral directions. Relevant parameters are listed in table 2.1.

### 2.2.2 Applying confining load and Consolidating

Before applying the deviatoric loading, specimens need to be confined to the prescribed initial pressure  $p_0$  ( $p_0 = 100$  kpa), and then to be consolidated into different porosities with the fixed confining pressure. In *DEM* software, there are two schemes of isotropically compressing the specimen. The first is the conventional scheme, which is to impose a equivalent incremental strain on boundaries of both directions. The second is a internal compacting scheme, which maintains the confining pressure and equally grows the radii of all particles. It is worth noting that the incremental radius is equal for

*Table 2.1: Parameters in the simulation.*

Parameter	Value
Particle number	25000
Model size	0.90 m × 1.35 m
Particles radii range	[0.75 $D_{50}$ , 1.25 $D_{50}$ ]
$p_0/k_n$	$10^{-4}$
$k_t/k_n$	0.5
Particle density	2600.0 kg/m <sup>3</sup>
$\phi$	30°
Particle-wall friction	0°
Confining pressure	100 kpa
Loading rate	0.01 s <sup>-1</sup>
damping coefficient	0.01 s/kg

every particle in a time step, being independent from any particle or interaction variable. Practically, this does not change the shape of the distribution, but imposes an increment in  $D_{50}$ . In the thesis work, the internal compacting scheme is adopted. After reaching the initial confining pressure  $p_0$ , to install specimens with targeted porosities, the confining pressure is maintained, while the friction angle gradually drops and the particle size grows. Porosity  $\phi$  and void ratio  $e$  are given by

$$\begin{aligned}\phi &= \frac{V_{void}}{V_t}, \\ e &= \frac{V_{void}}{V_t - V_{void}},\end{aligned}\tag{2.9}$$

where  $V_{void}$  is the void volume and  $V_t$  is the total volume of specimen.

### 2.2.3 Drained biaxial loading

Then specimens are subjected to a biaxial test with a constant confining pressure (100 kpa) and an axial compression of a constant strain rate (0.01 s<sup>-1</sup>). The computation lasted until 20% of axial strain to guarantee that specimens reached the steady state, i.e. the “critical state” (Roscoe et al., 1958; Schofield and Wroth, 1968). Then on the basis of the simulation results, micro-structure analyses in different aspects were carried out.

In micro-mechanical studies of chapter 3, according to different purposes, specific specimens are chosen in terms of porosity or whether there is a strain localization. This will be mentioned at the beginning of each specific investigation.

## 2.3 Conclusion

This chapter gives a knowledge of the used code and experiment preparation for the investigation in the chapter 3

An introduction on *DEM* is given in this chapter. The general concept and the main classifications of *DEM* are presented. Main steps in the calculation of *DEM* and fundamental equations in these steps are specified.

Test parameters and the protocol of the biaxial test on the 2D granular material, implemented by *Yade*, are demonstrated, as the preparation for the micro-mechanical investigation of the granular materials.



## Chapter 3

# Micro-structure Analysis in 2D Granular Material

Granular assemblies exhibit a very complex spectrum of constitutive features, which have drawn great attentions in the mechanical community in last few years: the strong nonlinear constitutive response, the definitive non-associated flow rule, and the existence of a bifurcation domain within the plastic limit surface, in which a variety of failure modes can be encountered (Darve et al., 2004; Nicot et al., 2009). The mechanical behavior of the granular material essentially originates from its micro-mechanical basis: the microscopic topology, the fabric distribution and evolution, and development and conjugation of intermediate clusters, etc. Especially, the intermediate clusters are observed to organize several particles (or contacts) to become evolution “partners” (groups), in the sense of the force transmission or the deformation. These clusters naturally appear in a scale being different from either the micro-scale, a single contact scale, or the macro-scale, in which the material can be considered as homogeneous. The word “intermediate” indicates this intermediate scale between the macro and the micro scale, i.e. the mesoscopic scale, called the meso-scale. Then the clusters in the meso-scale are generally designated the “meso-structures”.

Two patterns of meso-structure can be grasped in 2D granular assemblies: (1) the column-like cluster (called force-chain), which consists of grains (or contacts) carrying major forces in the material, taking charge of force transmission in the assembly (Dantu, 1968; Drescher and De Jong, 1972; Radjai et al., 1996; Mueth et al., 1998; Howell et al., 1999; Peters et al., 2005; Tordesillas, 2007); and (2) the loop-like cluster (hereafter called meso-loop), composed of a set of contacting grains forming a closed loop (Satake, 1992; Bagi, 1996; Kruyt and Rothenburg, 1996; Kuhn, 1999; Nguyen et al., 2009, 2012; Kruyt

and Rothenburg, 2014). In a quasi-static condition, force-chains line up along the major loading direction. Some of them may turn to a buckling configuration when subjected to exceeding loading, that probably disables them to carry the loading, i.e. the force-chain instability. Massive buckling events, as a result, correspond to a decrease of the material sustainability or a so-called “*stress softening*”. In practice, force-chains are confined by meso-loops. Stability of force-chains is therefore ensured by these confining structures (Tordesillas et al., 2010, 2014). The close interaction between force-chains and meso-loops is crucial for the mechanical response of granular material, and naturally, the morphology of these two meso-structures determines the mechanical property of the granular material.

In this chapter, the meso-structures and the rule they play on the mechanical behavior of the granular material, will be highlighted. Endeavors are made to answer three key questions: how meso-structures evolve? how two kinds of meso-structure interplay with each other? how the meso-structure evolution leads to some significant behaviors in the macro-scale? Some basic micro-mechanical measurements are described in section 3.1. Concepts of two significant meso-structures, the meso-loop and the force-chain, are led into the thesis in section 3.2. Then based on results of numerical tests, micro-structure analyses are implemented from various aspects: in section 3.3, the general evolution pattern of the meso-loops is presented; in section 3.4, the interaction between the force-chains and the meso-loops is investigated; section 3.5 aims to clarify the micro-structure basis of the critical state mechanics in localized and diffuse failure modes. All presented investigations in this chapter are based on 2D simulations using *DEM*, with the test procedure described in section 2.2.

### 3.1 Micromechanics of granular material

Granular body is an assembly of semi-rigid particles. The behavior of this assembly is defined by the particles’ kinematics and the contact law between particles. In the micro-scale, two-particle pairs, consisting of two contacting particles, are elements of this system. The contact of each two-particle pair is characterized by the contact force as the static variable and the relative displacement as the kinematic variable.

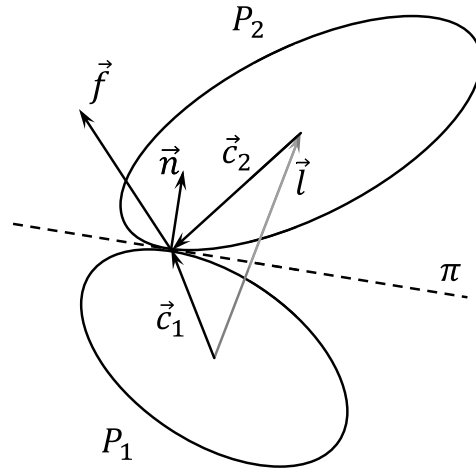


*Figure 3.1: Contact variables of a two-particle pair.*

Figure 3.1 illustrates a two-particle pair and different contact variables in its contact.  $\vec{f}$  is the contact force, the branch vector  $\vec{l}$  links centroids of the two particles, the unit vector  $\vec{n}$  is the contact normal, being perpendicular to the contact plane  $\pi$ , two contact vectors  $\vec{c}_1$  and  $\vec{c}_2$  link their respective grains centroid to the contact point. As spherical particles are employed,  $\vec{c}_1$ ,  $\vec{c}_2$ ,  $\vec{n}$  and  $\vec{l}$  converge to lay on the same line, then:

$$\begin{aligned}\vec{l} &= \vec{c}_1 - \vec{c}_2, \\ \vec{n} &= \frac{\vec{l}}{|\vec{l}|}.\end{aligned}\tag{3.1}$$

### 3.1.1 Description of the fabric

The coordinate number  $Z$  is the average number of contact shared by one particle. This quantity, evaluating the degree of the particles' connectivity, is given by:

$$Z = \frac{2N_c}{N_p},\tag{3.2}$$

where  $N_c$  and  $N_p$  are respectively the number of contacts and particles in the assembly.

$Z$  refers to the compact degree of the material, closely related to the density and the porosity of the material. Several empirical formulas have been found (Athanasίου-Grivas and Harr, 1980; Chang et al., 1990). A group of dense packing grains has a relative high  $Z$ , the contrast is in a loose material, a relative low  $Z$  will be observed. A sufficient  $Z$  is necessary for a granular assembly to maintain the equilibrium; an assembly consisting of particles insufficiently supported by their neighbors will turn to the dynamic state.

In the micro-scale, the granular fabric is basically a set of contacts oriented along different directions. Finding a variable, which is able to quantify the distribution of the contact orientations, is necessary to characterize the fabric. This variable can be a distribution, the contact directional distribution  $\omega(\theta)$ , or a tensor variable, the fabric tensor  $\underline{H}$ .

**Contact directional distribution**  $\omega(\theta)$  gives the probability density of contacts oriented along the direction  $\theta$  ( $\theta \in [0, \pi)$ ), such that the probability of a contact  $c$  oriented along the interval  $[\theta, \theta + \Delta\theta]$  is given by

$$P(\theta, \Delta\theta) = P(\theta \leq \theta_c \leq \theta + \Delta\theta) = \omega(\theta)\Delta\theta, \quad (3.3)$$

then the corresponding probability density function  $\omega(\theta)$  is expressed as

$$\omega(\theta) = \lim_{\Delta\theta \rightarrow 0} \frac{P(\theta, \Delta\theta)}{\Delta\theta}, \quad (3.4)$$

the number of contacts being in the sector  $[\theta, \theta + \Delta\theta]$  will be

$$N(\theta, \Delta\theta) = N_c \cdot P(\theta, \Delta\theta) = N_c \cdot \omega(\theta)\Delta\theta. \quad (3.5)$$

**Fabric tensor**  $\underline{H}$  gathers the directional information in contacts into a tensor, enabling it to be representative of the fabric anisotropy. Several kinds of fabric tensors can be built, when considering different contact variables (Satake, 1982):

- contact fabric tensor

$$H_{ij} = \int_{\theta} \omega(\theta) n_i n_j d\theta = \langle n_i n_j \rangle, \quad (3.6)$$

- branch fabric tensor

$$H'_{ij} = \int_{\theta} \omega(\theta) l_i l_j d\theta = \langle l_i l_j \rangle, \quad (3.7)$$

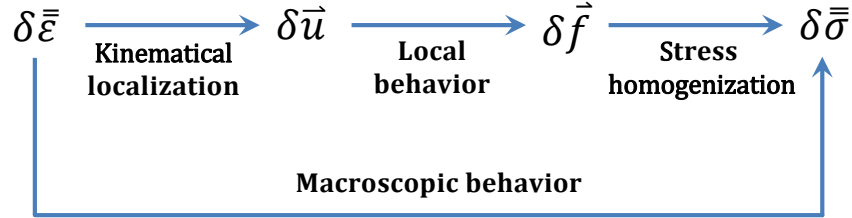


Figure 3.2: General homogenization scheme for multi-scale approaches of the granular material.

- combined fabric tensor

$$H''_{ij} = \int_{\theta} \omega(\theta) n_i l_j d\theta = \langle n_i l_j \rangle, \quad (3.8)$$

where  $n_i$  and  $l_i$  are respectively the contact normal and the branch vector in the direction  $\theta$ , subscripts  $i$  (or  $j$ ) represents the  $i$ th (or  $j$ th) component of the given vector.

Otherwise, since  $n_i$  is a unit vector,  $n_i n_i = 1$ , given  $\int_{\theta} \omega(\theta) d\theta = 1$ , thus  $tr(\underline{H}) = H_{ii} = 1$ .

### 3.1.2 Static and kinematic homogenization

The ultimate aim embedded in micro-mechanical research is to build a constitutive model, being capable to describe significant mechanical features of the granular material. Two macroscopic variables, stress and strain, are needed to be related by taking microscopic variables (contact forces and particles' movement) into account. This requires a multi-scale approach to connect variables in both scales. The general changing scale scheme of this approach is shown in Figure 3.2. In essence, micro-mechanical researches offer knowledges on the local behavior, the homogeneity methods enables the stress and the strain to be respectively expressed by the local static and kinematic variables. Deriving macroscopic variables from corresponding microscopic ones, is called "homogenization" procedure, and the contrast is "localization".

The static homogeneity refers to averaging the micro-scale variables into the stress, in a volume larger than the representative elementary volume *REV*. It can be solved by the Love formula (Love, 2013; Christoffersen et al., 1981; Mehrabadi et al., 1982):

$$\sigma_{ij} = \frac{1}{V} \sum_{c=1}^{N_c} f_i^c l_j^c, \quad (3.9)$$

where  $f_i^c$  and  $l_j^c$  are respectively the  $i$ th component of the contact force and the  $j$ th component of the branch vector in the contact  $c$ ,  $V$  is the volume of the analyzed domain.

The multi-scale approach of the constitutive modeling has to incorporate additional assumptions, in order to avoid solving the dynamic equation of each particle. The contact directional distribution and the fabric tensor describe the material fabric in a way, following the assumption that contact is individual from each other. It is a strong assumption in terms of the problem which will be mentioned in the kinematic homogenization. However, the convenience of the Love formula lies in that it also allows contacts to be considered separately, as there is not any information about the relative positions among contacts in its expression. Therefore, it is a good match between Love formula and the fabric description aforementioned.

The nature of the strain contains the relative displacement among points in the medium (particles or contact points). In granular medium, this relative displacement derives from two parts: (1) the displacement of contact branches or the relative displacement between particles in contact; and (2) the relative displacement among contact points or the relative displacement among neighboring particles without contact. Therefore, the construction of the strain out of the micro-scale kinematic variables does not agree with the assumption of individual contacts, as the contribution of latter part to the global strain is neglected. More important is that the latter part is significant for the global strain, as the fabric rearrangement is observed to prevail and persist in the material, even during the phase seen as elastic (please find evidences in section 3.3). Hence, considering contacts separately from each other probably leads to a large underestimation of the global strain. With regard to this, for 2D, many kinematic homogenization methods have been developed, involving two main streams: the best-fit methods (Cundall and Strack, 1979; Liao et al., 1997; Cambou et al., 2000) and equivalent continuum methods (Bagi, 1993, 1996; Kruyt and Rothenburg, 1996; Cambou et al., 2000), their details have been comprehensively introduced in the book “Micromechanics of Granular Materials” by

Cambou et al. (2009). Generally saying, the former obtains the strain in one geometrical point by best fitting particles' relative displacements in its neighborhood. According to different tessellation schemes, the latter builds the strain on the basis of divided elementary polygons, i.e. meso-loops, which will be introduced in section 3.2.

## 3.2 Meso-structure: force-chains and meso-loops

Two significant constitutive features of the granular material have been observed: (1) a granular assembly can increase (hardening phase) or lose its strength (softening phase) according to the initial state and the loading path. (2) The assembly volume can contract or dilate according to the initial state and the loading path. Correspondingly, two fundamental meso-scale features are recognized and connected to two aforementioned macroscopic features: (1) column-like structures as the force transmission tunnels to carry the most external loading, which form and buckle over the loading path and (2) grain loops, in 2D case, composed of a set of contacting grains forming closed cell-like loops. They are the aforementioned "meso-structures": force-chains and meso-loops. The concepts and methods to distinguish them will be presented in this section.

### 3.2.1 Force-chains

As a well-known feature of the granular material, due to the disordered packing, the grain media presents a strong heterogeneity in terms of the force transmission, when subjected to external loading (Cambou et al., 2009). The strongly inhomogeneous distribution of contact forces was first observed in the shearing test on the photoelastic material (Dantu, 1968; Drescher and De Jong, 1972; Howell et al., 1999). A decreasing exponential density distribution of force magnitude was found by analyzing prints of particles on the carbon paper set on the boundary (Jaeger et al., 1996). Later researchers, taking the advantage of numerical simulations, reveal that this exponential distribution only exists in the strong network, which consists of contacts with magnitude greater than the average (Radjai and Roux, 1995), while the weak network (complementary to strong network) is distributed in a uniform or power-law shape (Radjai et al., 1996; Mueth et al., 1998). In this context, the strong network is distinguished from the weak network, then the concept of force-chain was prepared on the basis of the strong network to define those quasi-linear columns, consisting of contacts with force magnitude greater than the average.

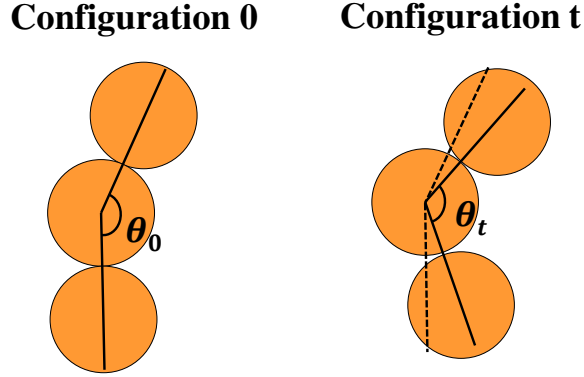


**Figure 3.3:** The inflection angle  $\theta$  in two configurations ( $\theta_0$  in configuration 0 and  $\theta_t$  in configuration  $t$ ). Continuous fold lines link two outer particle centers to the middle particle center, dashed fold line in configuration  $t$  refers to the original position of the fold line in configuration 0.

The concept of force-chain, herein, includes four characteristics which can be used to identify force chains: (1) all contact forces stronger than the average; (2) a geometrical linearity, that means column-like structure must exist; (3) a force transmission linearity, the major force transmission path must be in an approximately identical direction with the force-chain series; (4) at least three particles in the chain. One of the algorithms to identify the force-chain from the whole sample was proposed by (Peters et al., 2005). The particle stress tensor, which is in line with the wide accepted average scheme to build the stress on discrete element basis, is introduced as follows.

$$\tilde{\sigma}_{ij}^p = \frac{1}{V} \sum_{c=1}^{N_c} f_i^c c_j^c, \quad (3.10)$$

where  $N_c$  denotes the number of contacts imposed to the analyzed particle,  $f_i^c$  is the  $i$ th component of contact force in the contact  $c$ ,  $c_j^c$  is the  $j$ th component of the contact vector from the particle center to the contact point in the contact  $c$ . The compression positive convention is adopted. If  $\tilde{\sigma}_1^p$  is the major eigenvalue of one particle, particles with  $\tilde{\sigma}_1^p$  smaller than the average of major eigenvalue  $\langle \tilde{\sigma}_1^p \rangle$  of the whole sample are deleted from force-chain candidate list. For remaining particles, the direction of major eigenvalue  $\tilde{\theta}_1^p$  is considered to be the main force transmission direction. Then several algorithms proceed to seek force-chain particles satisfying qualifications (2), (3), (4). A complete detail can be found in (Peters et al., 2005).

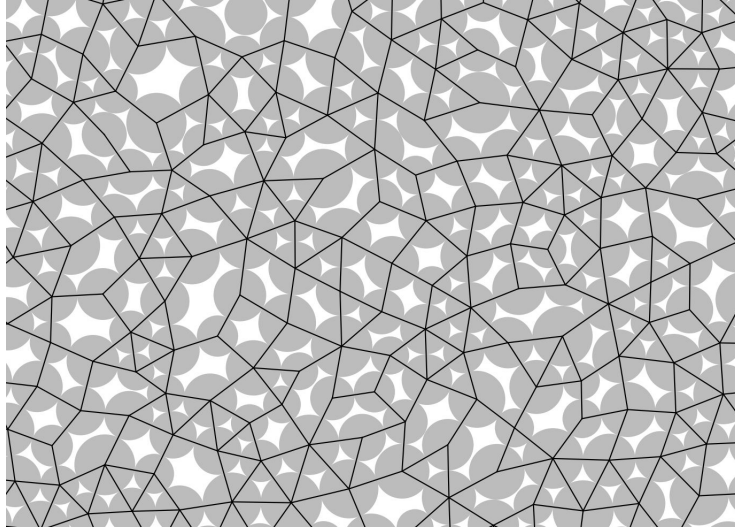


*Figure 3.4: The area tessellation by branch network.*

How the buckling columns can be determined is another important consideration. The force-chain is a priori subdivided in 3-particle sets, a series formed by three force-chain particles linking head to end. The inflection angle  $\theta$  of each 3-particle set (illustrated in Figure 3.3) is defined as the opening angle of the fold line formed by segments linking two outer particle centers to the middle particle center. During one considered time interval, the inflection angle of current configuration  $\theta_t$  of each 3-particle set is compared with that of the last configuration  $\theta_0$ , to obtain the buckling angle  $\theta_b$  such that  $\theta_b = \theta_0 - \theta_t$ . The condition of a buckling event is given by  $\theta_b > \theta_c$ , where  $\theta_c$  is a given threshold (Tordesillas, 2007).

### 3.2.2 Meso-loops

At any quasi-static state of the loading path, in which the inertia of the system is low enough to be omitted, the particles position and the contact data compose the entire information of the transient state. Thus, there exists a convenient way to map the granular assembly by the contact network linking the particle centers, where the topological structure at the meso-scale can be described by the polygons enclosed by this kind of contact network (Satake, 1992), as illustrated in Figure 3.4. Before tessellating the area, particles with no contact or only one contact to their neighbors are excluded. By using remaining contact branches, the assembly is discretized into sub-domains defined inside closed polygonal lines, i.e. meso-loops. Following is the algorithm to detect cycles in this thesis.

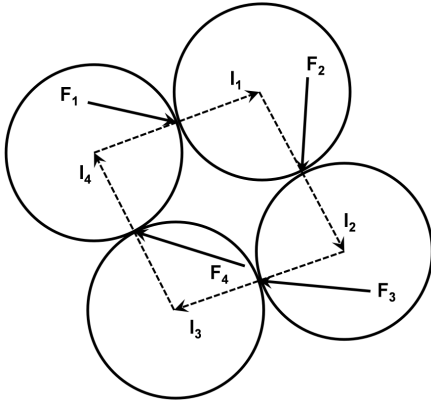


Figure 3.5: One identified cycle

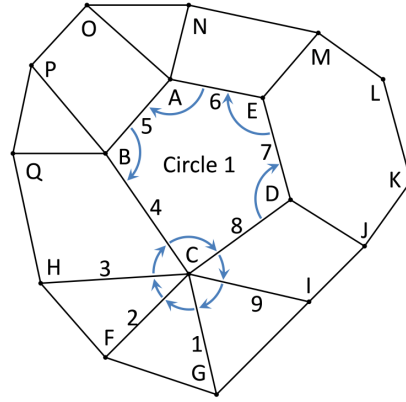


Figure 3.6: Algorithm of detecting cycle

All information obtained from the simulation structure comprise numbered point data and contact data. As shown in Figure 3.5, each point represents a particle center denoted by alphabets and each segment represents a contact denoted by arabic numerals linking two particles in contact. The data processing involves 4 steps (illustrated in Figure 3.6): (1) orderly recording all clockwise angles in the format [head contact, end contact, linking particle], for example particle C: [4, 8, C], [8, 9, C], [9, 1, C], [1, 2, C], [2, 3, C], [3, 4, C]; (2) gathering angles over all particles to form a container of angle, for any contact as a head contact, only two end contacts can be found belonging two different particles, like 8 with [8, 9, C], [8, 7, D]; (3) picking up any angle in the container (like [4, 8, C]) and matching head of another angle to its end (not sharing same particle, like [8, 7, D]), then continuing until capturing the initial contact of this cycle, in the showing case, the end-to-head angle lists are recorded [4, 8, C], [8, 7, D], [7, 6, E], [6, 5, A], [5, 4, B] to finish the detection of this cycle, then it is presented by its boundary contact [4, 8, 7, 6, 5]; (4) deleting all discovered angles in the container, searching for another cycle until the container to be empty.

### 3.3 Meso-loops evolution during biaxial loading

The main interests in the mesoscopic loops appear in three forms: (1) deriving the macroscopic continuum mechanical properties from the local static and kinematic quantities of an assembly of loops at a certain strain state; (2) the evolution of loops in terms of different initial states and loading paths; (3) the interaction between loops and the force-chain instability at the meso-scale. On the first point, the basic multi-scale constitutive modeling scheme inevitably involves the homogenization process (Cambou

et al., 1995), which is the way local variables (contact force and contact displacement, correspondingly) are averaged into macro variables in continuum-mechanics context (stress and strain). In this aspect, different schemes for approximating macroscopic stress and strain on meso-scale basis have been developed. Nguyen et al. (2012) gave the definition of the loop stress, Nguyen et al. (2009); Kruyt and Rothenburg (1996); Bagi (1996) respectively proposed equivalent-continuum approach and best-fit approach for approximating the global strain out of the local kinematics of loops. Even though loops' quantities of granular assemblies on transient state have been well investigated, however, how loops evolve during the loading path from different initial states remains unclear. To understand this, a view on the evolution of loops over the loading path is required.

The aim of this section is to investigate the evolution of some significant features of grain loops along the drained biaxial test from different initial states. In subsection 3.3.1, mechanical responses of three drained biaxial tests are recalled. In subsection 3.3.2, loops are a priori categorized into groups according to their side number. Geometrical features of these categories are then investigated. The intimate relation between mesoscopic structures evolution and macroscopic mechanical behavior of specimens is revealed. At the end of subsection 3.3.2, an inconsistency is noticed between the macroscopic volumetric evolution and the meso-loop evolution. The macroscopic volume contracts in the early phase of test, while the evolution of loops on the meso-scale tends to be dilatant, as small, dense loops are massively transformed to big, loose loops. Considering that the evolution of loops is basically a kind of plastic process, in order to explain this inconsistency, we should clarify the role the elastic phase plays on the total volume in the early phase of test. In subsection 3.3.3, the elastic and plastic phases of granular material are investigated in terms of the energy and the plastic volumetric strain.

### 3.3.1 Drained biaxial test and results

Specimens are prepared according to parameters given in subsection 2.2.1 and recalled in table 3.1. Three specimens of different initial porosities  $\phi_0$  (given by equation 2.9) are chosen. They are initially dense, intermediate and loose, ordered according to their respective  $\phi_0$  in table 3.2. It is worth emphasizing that the so-called dense and loose specimens have respectively the densest and loosest porosities, which the material can reach in the sample preparation. In addition, another specimen neither too dense nor too loose is chosen as an intermediate specimen.

*Table 3.1: Parameters in the simulation.*

Parameter	Value
Particle number	25000
Model size	$0.90\text{ m} \times 1.35\text{ m}$
Particles radii range	$[0.75 D_{50}, 1.25 D_{50}]$
$k_n$	$p_0/k_n = 10^{-4}$
$k_t/k_n$	0.5
Particle density	$2600.0\text{ kg/m}^3$
$\varphi$	$30^\circ$
Particle-wall friction	$0^\circ$
Confining pressure	100 kpa
Loading rate	$0.01\text{ s}^{-1}$

*Table 3.2: The initial porosity of three specimens.*

Specimen	$\phi_0$
Dense	0.148
Intermediate	0.171
Loose	0.187

Three specimens are then subjected to drained biaxial loading path. Evolutions of the deviatoric stress ratio  $q/p_0$  of specimens in terms of axial strain  $\varepsilon_2$  is shown in Figure 3.7a, where  $q = \sigma_2 - \sigma_1$ ,  $\sigma_1$  and  $\sigma_2$  are correspondingly the axial stress and the lateral stress. Figure 3.7b, Figure 3.7c and Figure 3.7d respectively illustrate evolutions of the volumetric strain  $\varepsilon_v$ , the coordination number  $Z$  (determined by equation 3.5, introduced in section 3.1) and the total number of loops  $N_l$  in terms of axial strain  $\varepsilon_2$ , where  $\varepsilon_v = -(\varepsilon_1 + \varepsilon_2)$ .

In Figure 3.7a and 3.7b, specimens present a typical stress and strain response from dense to loose ones. Stress peak and softening are found in both dense specimen  $\phi_0 = 0.148$  and intermediate specimen  $\phi_0 = 0.171$ . The dense specimen has the highest stress peak and largest stress softening, while loose specimen  $\phi_0 = 0.187$  shows consistently stress hardening until the steady stress. At the stress steady state, all samples gradually turn to oscillate around roughly the same value. In terms of the volumetric strain, the dense specimen has the lightest contractancy and the largest dilatancy, while the loose specimen shows a continuous contractancy. The volumetric diagram exhibits a typical disparity from dense to loose specimen. The different volumetric evolution may lead to a different evolution pattern of the meso-loop, which is expected to be sensitive to the volumetric variation. This will be investigated in subsection 3.3.2.

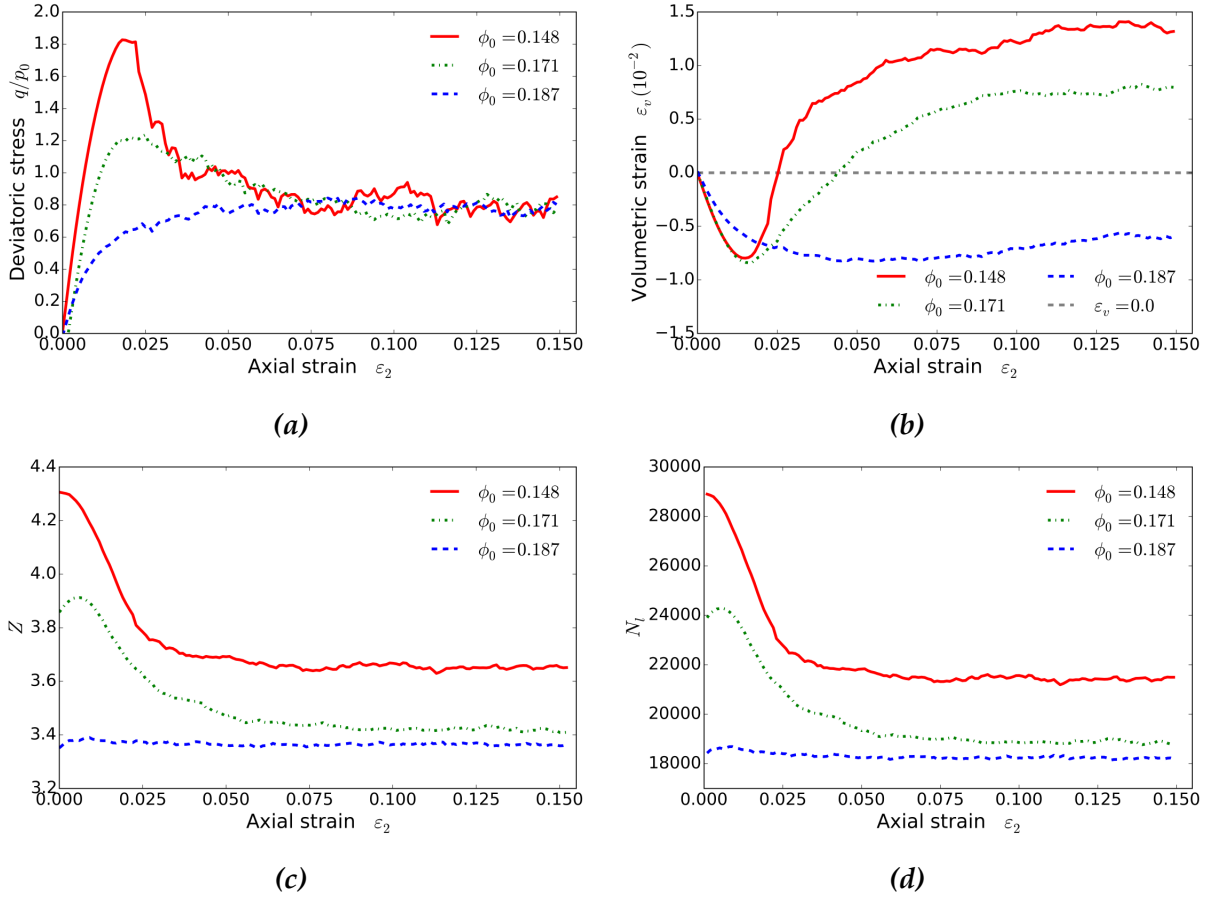


**Figure 3.7:** Evolutions with respect to axial strain  $\varepsilon_2$  of (a) deviatoric stress ratio  $q/p_0$ , (b) volumetric strain  $\varepsilon_v$ , (c) coordination number  $Z$  (d) total number of loops  $N_l$

It is shown in Figure 3.7c that  $Z$  in the dense specimen starts with a dramatic fall from the beginning. The loose specimen has a more or less constant  $Z$ . In Figure 3.7d, the evolution of total number of loops  $N_l$  shows a similar pattern to the evolution of  $Z$ . The quantitative similarity between the total number of loops and coordination number  $Z$ , as shown in Figure 3.7c and 3.7d, can be explained by the Euler's relation for 2D topology. If  $N_p$  and  $N_c$  respectively denote the number of particles and the number of contacts, for large homogeneous assemblies, the following relation  $N_p + N_l - N_c \cong 0$  holds (Kruyt and Rothenburg, 2001), which is equivalent to  $N_l \cong N_p(Z/2 - 1)$ . As  $N_p$  is given,  $N_l$  therefore evolves similarly to  $Z$ .

In Figure 3.7c and Figure 3.7d, the non-convergent on both  $Z$  and  $N_l$  is observed. There are not convergent mechanical responses in the critical state Roscoe et al. (1958); Schofield and Wroth (1968), indicating that the inhomogeneity may exist in some specimens. This will be discussed in the section 3.5.

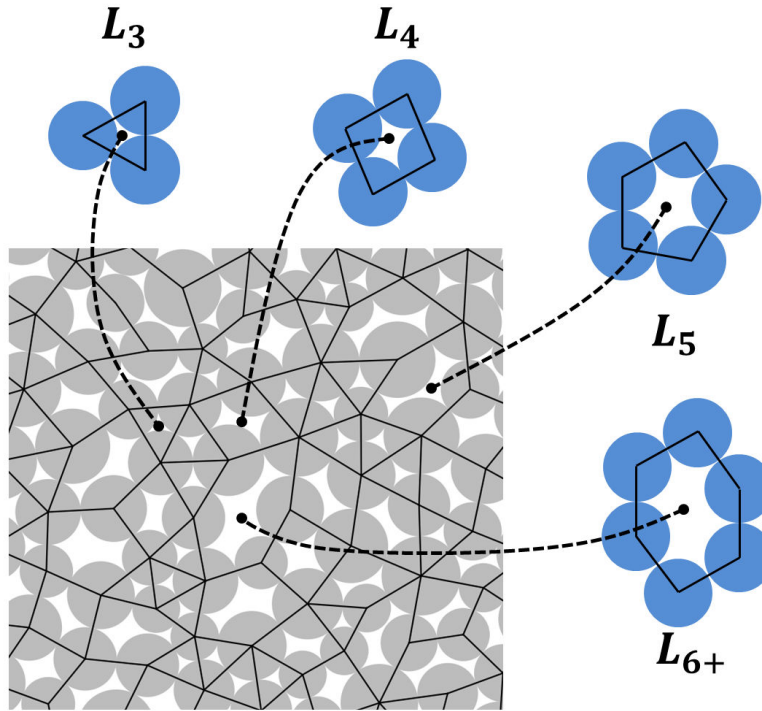
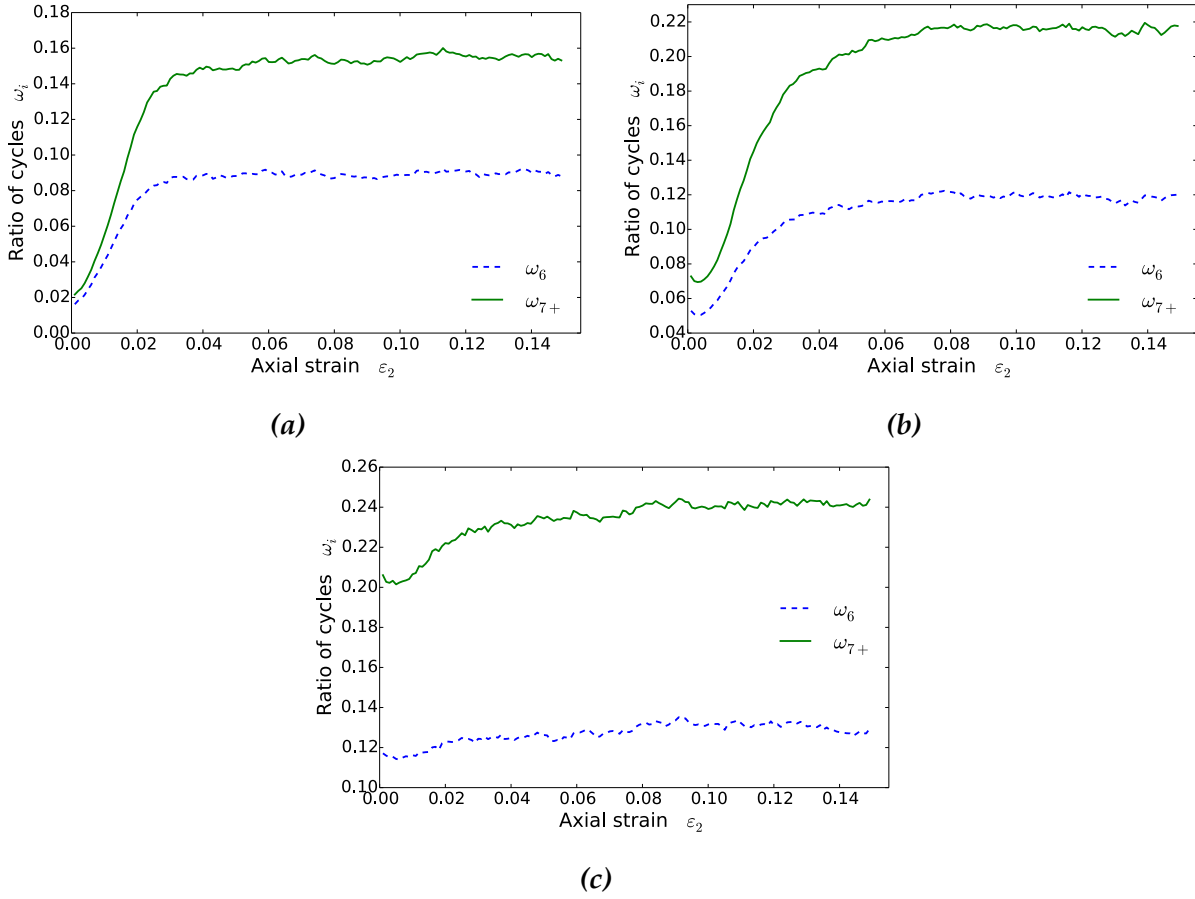


Figure 3.8: Four categories of loops.

The importance of loops lies in the fact that they can be the link between the strength and the deformation of the granular material. On one hand, as media carrying contact forces, loops sustain the external load transmitted to them. The material strength is then highly dependent on the mesoscopic topology of loops. On the other hand, given the granular assembly area is entirely tessellated into loops, the material macroscopic deformation can be interpreted on the basis of the transformation of loops. Consequently, the mechanical and geometrical features of loops should be investigated in a more elaborate way.

### 3.3.2 Meso-loops evolution

The geometrical nature differentiates the mechanical property of one loop from another. Amongst different properties of the loop, side number plays significant role on its behavior. For example, when side number increases, with larger internal void area and more freedom degree, loops tend to be looser and more deformable; the odd side loop is self-locked to inter-particle rotation. Therefore, loops are categorized on the basis of their side number,  $L_i$  denote the loop category with side number being equal to  $i$  ( $i = 3, 4, 5, \dots$ ). The proportion of 4 loop categories are calculated as  $\omega_i = N_i^{L_i} / N_l$ ,



**Figure 3.9:** Evolutions of  $\omega_6$  and  $\omega_{7+}$  against axial strain  $\varepsilon_2$  in specimen (a)  $\phi_0 = 0.148$  (b)  $\phi_0 = 0.171$  (c)  $\phi_0 = 0.187$ .

where  $N_i^{L_i}$  is the number of loops in  $L_i$ . However, in order to limit our analysis to main loops, it is convenient to define a side number  $i^*$ , from it onwards,  $\omega_i$  of larger loops evolves in a similar pattern. Indeed, if we combine loops with side number greater than or equal to 7 into one category, it can be shown that its proportion  $\omega_{7+}$  is comparable with  $\omega_6$ .

$\omega_6$  and  $\omega_{7+}$  in specimens of different  $\phi_0$  are shown in Figure 3.9 as function of axial strain  $\varepsilon_2$ . It is observed that  $\omega_{7+}$  evolves in a similar pattern as  $\omega_6$  in all specimens. To simplify the forthcoming analysis presented in this manuscript, we combine the ratios of  $L_6$  and  $L_{7+}$  into one category, hereafter called  $L_{6+}$ . Consequently, there are 4 categories of loops  $L_i$  ( $i = 3, 4, 5, 6+$ ), identified on the basis of their side number, as illustrated in Figure 3.8.

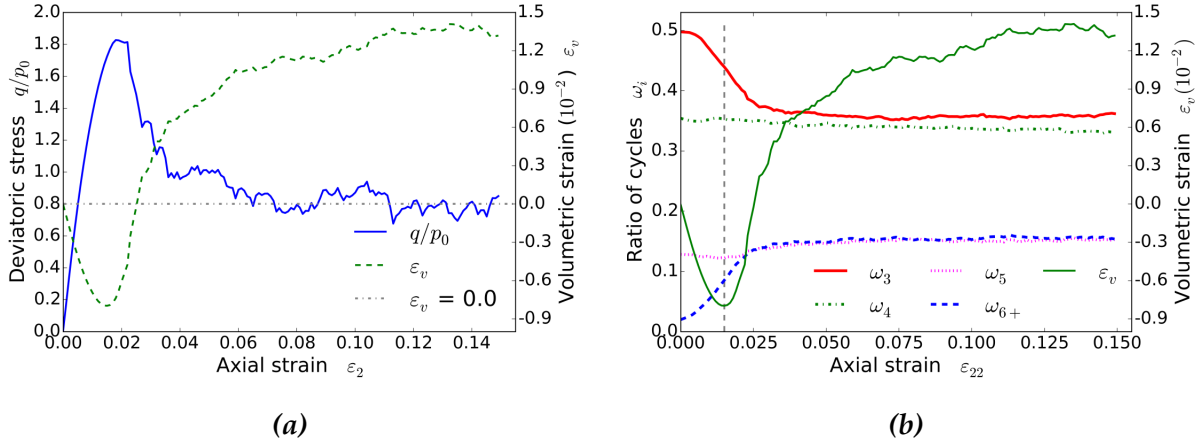


**Figure 3.10:** Evolutions in specimen  $\phi_0 = 0.148$  with respect to axial strain  $\varepsilon_2$  of (a) deviatoric stress  $q/p_0$  and volumetric strain  $\varepsilon_v$ , (b) proportions of different loops compared with the volumetric strain  $\varepsilon_v$ ; the vertical dashed line is the guide line crossing the volume minimum.

### 3.3.2.1 Proportional analysis of different loops

In this subsection, the proportions of four loop categories ( $\omega_3$ ,  $\omega_4$ ,  $\omega_5$  and  $\omega_{6+}$ ) in three specimens are analyzed and compared with their stress and volumetric evolutions. In practice, because of a progressive loading exerted on the granular assembly, its texture keeps stirred. The evolution in loop categories just gives a sensible characterization, state by state, on this kind of irreversible texture rearrangement. Therefore, it is worth emphasizing that the discussion in this subsection is, in essence, in the scope of plastic behavior of granular materials. The conception of elastic and plastic phases in meso-scale will be discussed in section 3.3.3.

Figure 3.10b shows that in a dense specimen,  $\omega_3$  and  $\omega_{6+}$  display prominently opposite ways of evolution during biaxial loading path.  $\omega_3$  decreases and  $\omega_{6+}$  increases significantly at the early stage of the test and then turn to be constant at the (stress) steady state. It is worth noting that the inflection points of both  $\omega_3$  and  $\omega_{6+}$  coincide with the minimum volume. The dramatic dilatancy that follows is concurrent with a remarkable decrease in  $\omega_3$  and increase in  $\omega_{6+}$ . In other words, a massive conversion from firm, dense structures to deformable, loose structure occurs. While the deviatoric stress drastically drops after peaking, as shown in Figure 3.10a,  $\omega_3$  and  $\omega_{6+}$  present the maximum curvatures (or second order derivatives) subsequently to reach steady values. This indicates the subsiding of the meso-loop evolution. Moreover,  $\omega_4$  and  $\omega_5$  are more or less constant, being independent to the stress and volumetric evolution.

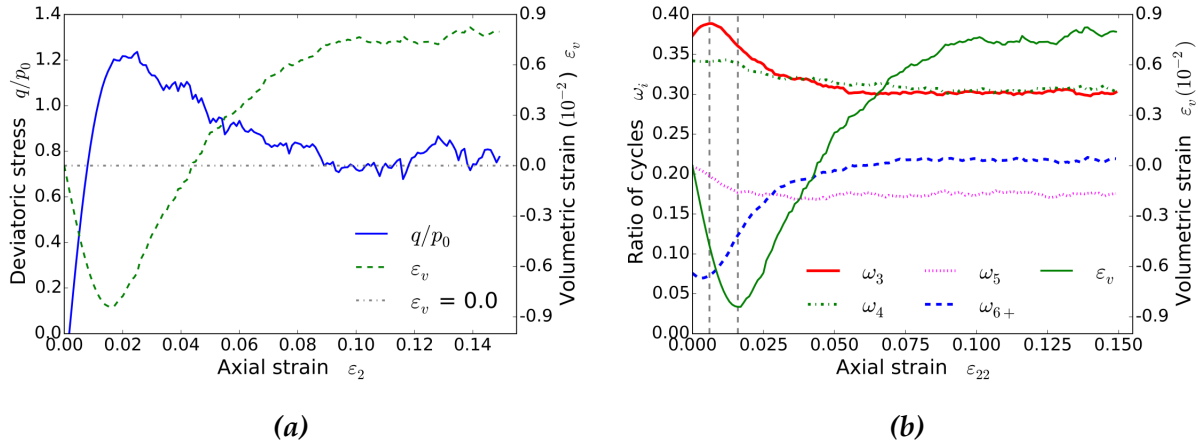


**Figure 3.11:** Evolutions in specimen  $\phi_0 = 0.171$  with respect to axial strain  $\varepsilon_2$  of (a) deviatoric stress  $q/p_0$  and volumetric strain  $\varepsilon_v$ , (b) proportions of different loops compared with the volumetric strain  $\varepsilon_v$ ; the vertical dashed lines respectively cross the  $\omega_3$  maximum and the volume minimum.

As shown in Figure 3.11, in the intermediate specimen,  $\omega_3$  also reverses the evolution pattern of  $\omega_{6+}$  as in the dense specimen.  $\omega_3$  and  $\omega_{6+}$  experience respectively a slight rise and drop at the very early phase of test and then subsequently decrease and increase to their final values. Similar to the case of the dense specimen, the inflection points of both decrease of  $\omega_3$  and increase of  $\omega_{6+}$  also appear to be simultaneous with the volumetric minimum. After that, the specimen drastically dilates with  $\omega_3$  decreasing and  $\omega_{6+}$  increasing gradually and consistently. Otherwise,  $\omega_5$  is more active than that in the dense specimen, decreasing smoothly over the loading path, while  $\omega_4$  is more or less constant in the test.

As shown in figure 3.12, in the loose specimen, similar to the case of intermediate specimen,  $\omega_5$  declines smoothly while  $\omega_3$  and  $\omega_4$  oscillate around the same level.  $\omega_{6+}$  drops slightly at the beginning to a minimum point and then increases. Particularly, ratios of all kinds of loop in the loose specimen evolve less pronouncedly than those in denser specimens.

Before interpreting the results, let us recall the bond between meso-loops geometry and their mechanical properties. In terms of density, amongst loops,  $L_3$  is the densest kind in the granular assembly, while  $L_{6+}$  is the loosest one. In terms of sustainability,  $L_3$  is the firmest among all kinds of loop, while  $L_{6+}$  is the most deformable one. With respect to these two aspects,  $L_4$ ,  $L_5$  are in the middle. After being destroyed,  $L_3$  tends to transform into loops with more sides and larger volume, leading to the dilatancy in the meso-scale; meanwhile,  $L_{6+}$  has higher ability to lead to the contractancy.

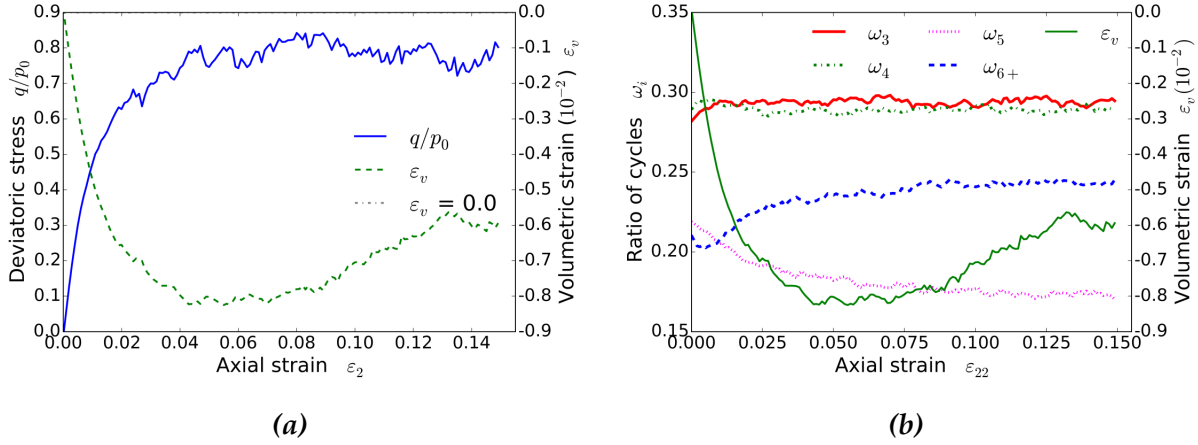


**Figure 3.12:** Evolution in specimen  $\phi_0 = 0.187$  with respect to axial strain  $\varepsilon_2$  of (a) deviatoric stress  $q/p_0$  and volumetric strain  $\varepsilon_v$ , (b) ratio of different loops compared with the volumetric strain  $\varepsilon_v$ .

Turning to the result, of the dense and intermediate specimens, two common features of the meso-loop evolution should be highlighted. First,  $L_3$  and  $L_{6+}$  are the two most active groups in terms of population variation. In fact, they form an evolutionary pair with an entirely opposite (or negatively correlated) evolution pattern from each other. This indicates that  $L_3$  and  $L_{6+}$  are closely bonded meso-loops, their mutual conversion can be representative of fabric evolution on the meso-scale. And secondly, in dense and intermediate specimens,  $L_3$  and  $L_{6+}$  are respectively continuously decreasing and increasing in their populations, that is to say, there is an enormous conversion from  $L_3$  to  $L_{6+}$ . This results in two significant mechanical features on the macro-scale: (1) a continuous and substantial conversion from firm elements to deformable elements drains the sustainability of the material, leading to stress softening; and (2) a continuous and substantial conversion from dense elements to loose elements, finally causes the volumetric dilatancy. The meso-loop, to this degree, is the basis and the origin of the stress and volumetric behavior of granular material. It can be the link between these two fundamental mechanical features.

As a result, the creation of  $L_{6+}$  and the destruction of  $L_3$  potentially direct the specimen to dilate. The word “potential” means there is not a definitive macroscopic dilatancy but an underlying tendency beneath the macroscopic phenomena, which is suggested by the meso-loop evolution. Here we denote this potential dilatant tendency the “meso-scale volumetric dilatancy” (*MV-D*). On the contrary, the creation of  $L_3$  and the destruction of  $L_{6+}$ , as what happens during  $\varepsilon_2 = [0.000, 0.006]$  for the intermediate specimen, is denoted by “meso-scale volumetric contractancy” (*MV-C*). The ensemble of *MV-D* and *MV-C* is

called “meso-scale volumetric variation” ( $MV$ ). During the major process of the biaxial test in which we observe  $MV-D$  or  $MV-C$ , the macroscopic dilatancy or contractancy also appear correspondingly. However, not all of the results seem to support this link between macro and meso evolutions. In the dense specimen, an inconsistency arises, because in the contractant phase (before grey line in Figure 3.10b), there are simultaneously decreasing  $\omega_3$  and increasing  $\omega_{6+}$ , i. e.  $MV-D$ . In intermediate specimen, there is also a slot where  $MV-D$  and global contractancy occur simultaneously, between the  $\omega_3$  peak and volume minimum, the range between two vertical grey lines in Figure 3.11b. These inconsistencies will be investigated in subsection 3.3.3.

The situation is different in the loose specimen, as there is not a substantial meso-loop transformation. To note is that  $\omega_3$  only rises slightly at the very beginning and keeps constant afterwards. This indicates that, on one hand, it is difficult to massively build  $L_3$  along the biaxial loading path, even in a contractancy phase. A merely contractancy is insufficient in bringing substantial  $L_3$  into the system. On the other hand, unlike what occurs in dense and intermediate specimens, the system cannot additionally loose  $L_3$  in a population being already low-leveled. This reveals that  $L_3$  is significant for a granular system. The granular system needs a sufficient population of  $L_3$  to maintain its internal strength. Otherwise, the quasi-static state can be hardly reached, when the system mainly consists of deformable loops ( $L_4, L_5, L_{6+}$ ).

### 3.3.2.2 Area change of different loops

Another aspect of meso-loop evolution is expressed by the area change of loops with the loading path. Here we trace the area ratio  $a_i$  of the loop category  $L_i$ , which is equal to  $A_i/A_T$ , where  $A_i$  is the total area of  $L_i$ ,  $A_T$  is the total area of all loops. We note that the area of a loop comes from the total area enclosed by its boundary formed by the contact branches.

As shown in Figure 3.13,  $a_i$  in different specimens presents more or less similar patterns as their loop ratio ( $\omega_i$ ) evolutions, as discussed in last subsection. In dense and intermediate specimens, only  $a_{6+}$  increases the volume, while  $a_3, a_4, a_5$  experience consistent drops, during the biaxial test. In the loose specimen,  $a_3$  and  $a_4$  are relatively constant during the loading path.

Furthermore, we have to know the effect that the biaxial test has on the average area of loop. Thus, the average area  $\bar{A}_i$  of  $L_i$  are plotted in Figure 3.14 as the function of axial strain  $\varepsilon_2$ . However, the quantitative descriptors of  $\bar{A}_{6+}$  cannot be compared with the values for the other loops. Because  $L_{6+}$  is not a loop kind with a given side number but a

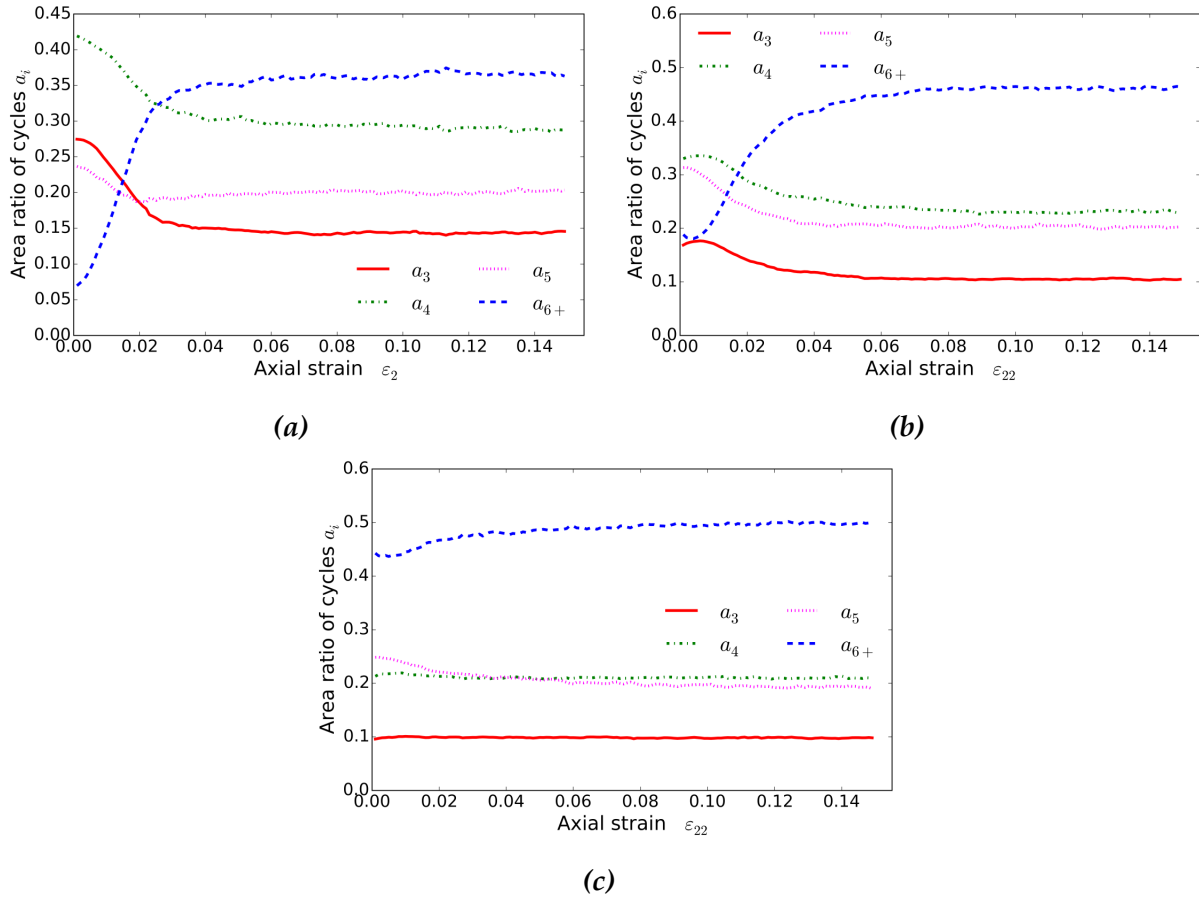


**Figure 3.13:** Evolution of area ratio  $a_i$  of different loops against axial strain  $\varepsilon_2$  in specimen (a)  $\phi_0 = 0.148$  (b)  $\phi_0 = 0.171$  (c)  $\phi_0 = 0.187$ .

set of different kinds of loops, then  $\bar{A}_{6+}$  turns to be highly dependent on the proportions of sub-families in  $L_{6+}$ . Considering that  $\bar{A}_3$ ,  $\bar{A}_4$  and  $\bar{A}_5$  should be only compared to the value of a category with comparably geometrical meaning, the difference of the average area investigation from former ones is that  $L_{6+}$  can no longer be analyzed as a group. Therefore, instead of  $\bar{A}_{6+}$ , we examine  $\bar{A}_6$  as a representative of the large loops.

As shown in Figure 3.14, it is obvious that in all specimens,  $\bar{A}_3$ ,  $\bar{A}_4$ ,  $\bar{A}_5$  are almost constant during the biaxial test,  $\bar{A}_6$  is the only category sensitive to the loading path.  $\bar{A}_6$  in three specimens drops at the early stage of the test and keeps constant in the remainder, hardly experiencing any rise. It is rational to speculate a same pattern in other kinds of large loop.

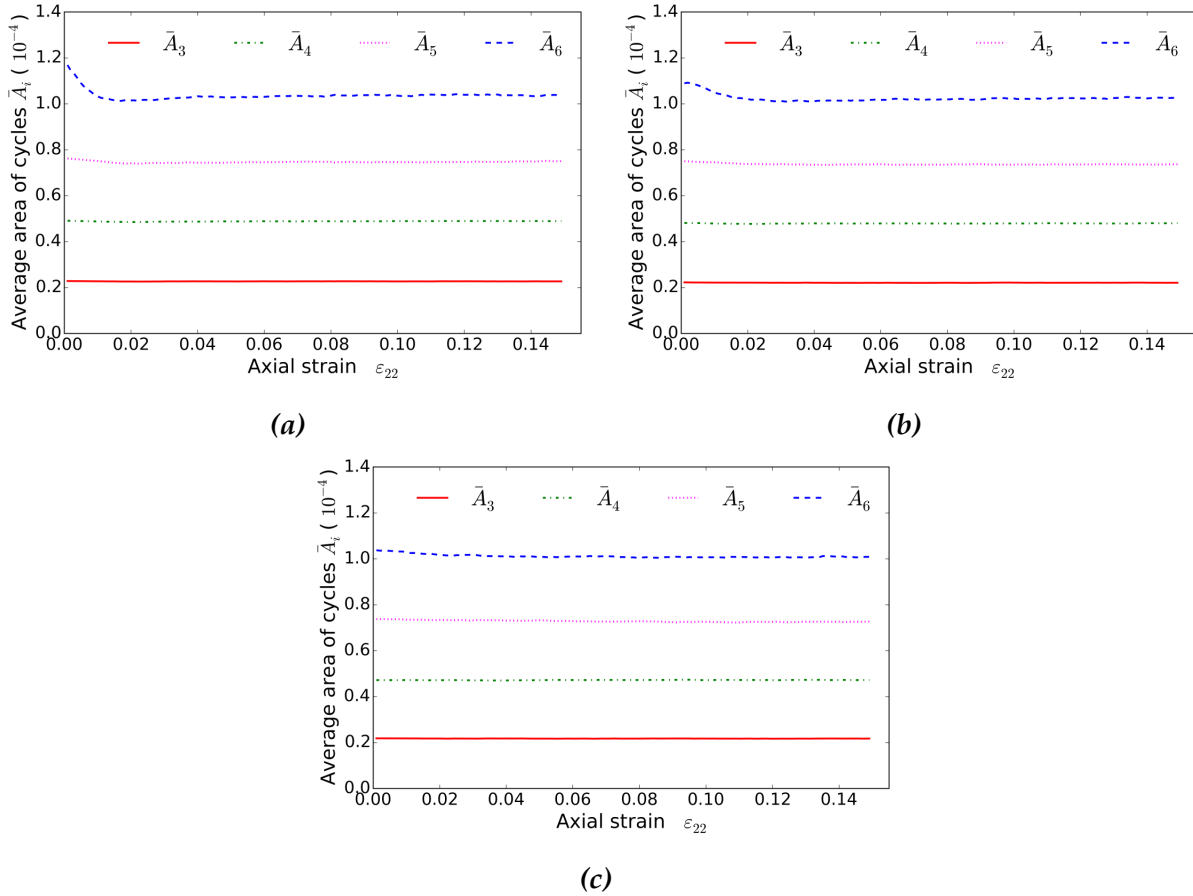


**Figure 3.14:** Evolution of average area  $\bar{A}_i$  of different loops against axial strain  $\varepsilon_2$  in specimen (a)  $\phi_0 = 0.148$  (b)  $\phi_0 = 0.171$  (c)  $\phi_0 = 0.187$ .

When overviewing the area behavior of meso-structures, we can observe several features: (1) the area ratio of different loops  $a_i$  shows a similar pattern to the evolution of  $\omega_i$ ; (2) the  $L_{6+}$  is the most active structure in terms of total area variation ( $a_{6+}$ ), and the average area of large loops is sensitive to the biaxial loading; (3) according to the evolution of  $a_i$ , only  $L_{6+}$  contributes to the global dilatancy in dense and intermediate specimens.

According to the result of  $\bar{A}_i$  evolution,  $L_6$  (probably the same for other large loops) is the kind of loop geometrically sensitive to the external loading. This means that  $L_3$ ,  $L_4$ ,  $L_5$ , on average, keep geometrically independent to the biaxial loading path and initial state. To this extent, the ratio variations of different loops ( $\omega_i$ ) can be representative of the global volumetric variation, given the average area of different loops mostly keeps constant. Meanwhile, the evolution of  $a_i$  in dense and intermediate specimens shows that only  $L_{6+}$  experiences a volume increase during the loading path while the other kinds

of loop contract. In fact, having more sides gives rise to  $L_{6+}$  the ability of transforming. That results in two possibilities: shape fine-tuning or entirely changing to other loop categories. The effect of the latter can be also seen in the variation of  $\omega_{6+}$ . Consequently, we can conclude that  $L_{6+}$  exerts the strongest influence on global volumetric variation.

### 3.3.3 The existence of elastic and plastic phases in meso-scale

In Figure 3.7c, there is a rise in the number of contacts, which occurs in intermediate and loose specimens with  $Z$  rising up from the outset. The additional contacts with increasing  $Z$ , practically, can be explained by the volume contraction in specimens, vice versa, most ranges of decreasing  $Z$  are also related to volumetric dilatancy. In other words, increase in  $Z$  corresponds to contractancy and decrease in  $Z$  corresponds to dilatancy. To this extent, the global volumetric evolution is in line with the micro-structure evolution. However, we also capture some situations where  $Z$  decreases with volume contracting in the meantime, such as  $\varepsilon_2 = [0.000, 0.015]$  of dense specimen and  $\varepsilon_2 = [0.006, 0.016]$  of intermediate specimen (Figure 3.7c). Here the micro-structure evolves against the tendency of the macroscopic volume variation. It is worth noting that this kind of contradiction also occurs in the meso-loop analysis.

According to subsection 3.3.2, in dense and intermediate specimens between peak of  $\omega_3$  and volumetric minimum (the dash line in Figure 3.10b and Figure 3.11b), a drastic drop in  $\omega_3$  and a rise in  $\omega_{6+}$  exist ( $\varepsilon_2 = [0.000, 0.015]$  in Figure 3.10b,  $\varepsilon_2 = [0.006, 0.016]$  in Figure 3.11b) along with the volumetric contractancy. The acute creation of the loose structure  $L_{6+}$  and loss of the dense structure  $L_3$  are supposed to lead to the dilatancy of the material volume, however instead, we observe contractancy.

#### 3.3.3.1 Elasticity and plasticity in the meso-scale

To investigate this inconsistency, we have to consider the elasto-plastic behavior of the granular material from a mesoscopic viewpoint. In elasto-plasticity,  $\varepsilon_v$  is divided into elastic part  $\varepsilon_v^e$  and plastic part  $\varepsilon_v^p$ . From a microscopic viewpoint, contact forces are defined at particle level (scale of two contacting particles), so that  $\varepsilon_v^e$  and  $\varepsilon_v^p$  are respectively derived from the particles penetration and the inter-particle sliding. This viewpoint leads to an underestimation of  $\varepsilon_v^p$ , as in a granular assembly,  $\varepsilon_v^p$  originates not only from the inter-particle sliding and particles rotation but also from the inter-contact (or fabric) rearrangement. In the meso-scale, the volumetric variation can be properly

defined: the penetrations between particles, which are able to rebound after loading, is connected to the elastic phase; the micro-structure rearrangement, which is represented by the evolution of different categories of loops and cannot rebound after loading, is connected to the plastic phase of the granular assemblies.

Following this line of reasoning, the aforementioned paradoxical contractancy (regardless of the dramatic  $\omega_3$  drop and  $\omega_{6+}$  rise) in dense and intermediate specimens, is assumed to be largely induced by particles penetration, which diminishes the volume of the specimen, even though loops evolution suggests dilating. In other words, in the contractancy phase where macroscopic volume evolution is inconsistent with the meso-loop evolution, particles penetration dominates the volumetric behavior of the material over the meso-loop rearrangement, leading to a macroscopic contractancy. To verify this hypothesis, an investigation on the evolution of the system energy, divided into elastic and plastic parts, is carried out. The particles penetration is intimately connected to the incremental elastic energy of the specimen, while loops rearrangement, to some degree, is related to incremental plastic energy.

### 3.3.3.2 Elastic energy and plastic dissipation

The elastic energy  $E_e$  at a strain state is given by

$$E_e = \frac{1}{2} \sum_c \left( \frac{f_n^c{}^2}{k_n} + \frac{f_t^c{}^2}{k_t} \right), \quad (3.11)$$

Where  $f_n^c$  and  $f_t^c$  denote respectively the normal and tangential forces in local coordinate system of each contact. The plastic energy in incremental form is given by

$$\begin{cases} \delta E_p = \sum_c f_t^c \cdot \delta l_t^{cp} \\ \delta l_t^{cp} = \delta l_t^c - \delta f_t^c / k_t \\ \delta f_t^c = \min \{ f_t^c + k_t \delta l_t^c, \tan \varphi_g (f_n^c + k_n \delta l_n^c) \zeta \} - f_t^c \end{cases} \quad (3.12)$$

where  $\delta l_t^c$  and  $\delta l_t^{cp}$  denote, respectively, increment and plastic increments of shearing displacement,  $\varphi_g$  is the internal friction angle between particles,  $\zeta$  is the sign of the value  $f_t^c + k_t \delta l_t^c$ .

In this subsection, the elastic energy and plastic dissipation of two specimens  $\phi_0 = 0.148$  and  $\phi_0 = 0.171$  are investigated. The increment of both elastic and plastic energy is discussed in terms of their contributions to volumetric strain.

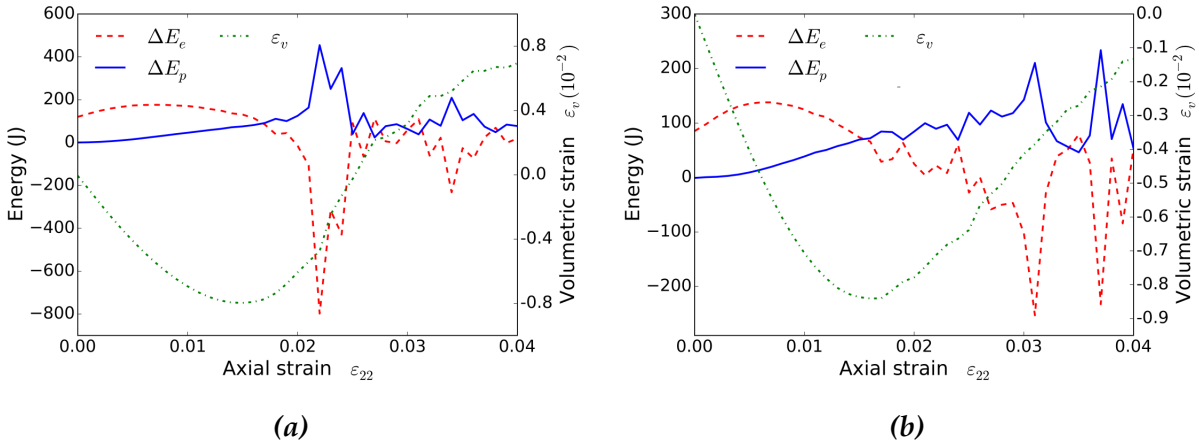


**Figure 3.15:** Evolution of incremental elastic and plastic energy, compared with the evolution of  $\varepsilon_v$ , in terms of the axial strain  $\varepsilon_2$ , in specimen (a)  $\phi_0 = 0.148$  (b)  $\phi_0 = 0.171$ .

The incremental elastic energy  $\Delta E_e$  and plastic dissipation  $\Delta E_p$  of dense specimen  $\phi_0 = 0.148$  and intermediate specimen  $\phi_0 = 0.171$ , compared with their volumetric strain  $\varepsilon_v$ , as a function of axial strain  $\varepsilon_2$ , are presented in Figure 3.15a and 3.15b respectively. Both incremental energies are calculated during each axial strain step of  $\varepsilon_2 = 0.001$ . The scale of  $\varepsilon_2$  is zoomed into  $[0.000, 0.040]$  to avoid displaying the violent oscillation of the energy.

Figure 3.15 shows that in both specimens,  $\Delta E_e$  increases from the beginning and then decreases consistently after a peak, while  $\Delta E_p$  in two specimens increases gradually from 0 J. This is followed by a dramatic drop on  $\Delta E_e$  and jump of  $\Delta E_p$ . It is worthy to note that the intersection points, where  $\Delta E_e$  is equal to  $\Delta E_p$ , coincide with the minimum volume of both specimens. The range, in which  $\Delta E_e$  overcomes  $\Delta E_p$ , covers almost throughout the volumetric contractancy.

These results support the assumption that in most contractant phase of dense and intermediate specimens, the elastic part (particle penetration) of micro-structure dominates the global volumetric behavior against the plastic part (micro-structure rearrangement). So in those elastic dominant phases, the effect of  $\varepsilon_v^p$  is erased and cannot be clearly displayed.

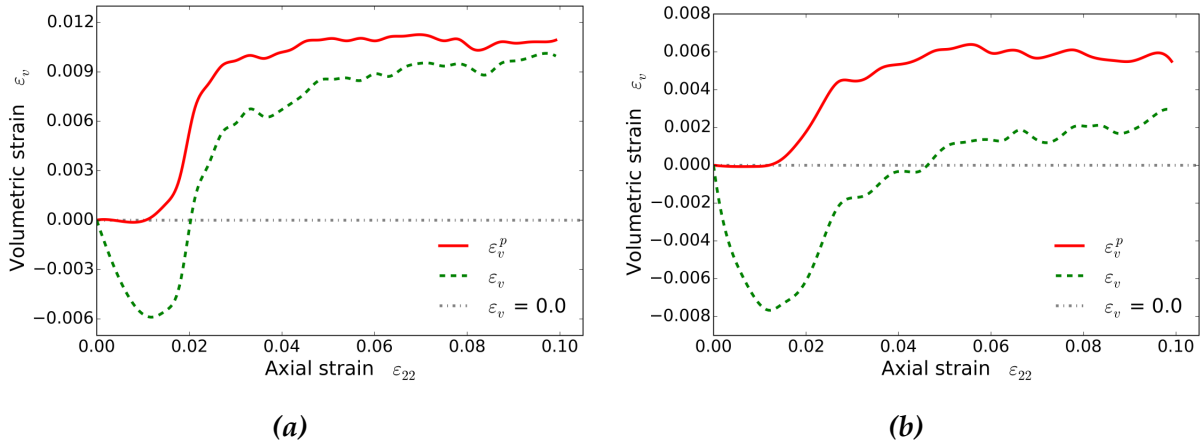


*Figure 3.16: Evolution of plastic volumetric strain  $\varepsilon_v^p$  and total volumetric strain  $\varepsilon_v$  in terms of axial strain  $\varepsilon_2$  in specimen (a)  $\phi_0 = 0.152$  (b)  $\phi_0 = 0.172$ .*

### 3.3.3.3 Plastic volumetric strain in dense packed assemblies

To further understand the plastic volumetric behavior of dense and medium granular assemblies in the contractant phase, we need to quantitatively distinguish the plastic volumetric strain  $\varepsilon_v^p$  from its elastic counterpart  $\varepsilon_v^e$ . Then two new specimens under drained biaxial loading path are performed (dense  $\phi_0 = 0.152$  and intermediate  $\phi_0 = 0.172$ ), prepared according to parameters in Table 3.1 but involving 10000 particles. At the end of each stress increment, an elastic unloading is processed, in order to reach the original stress state of this increment. The incremental plastic volumetric strain  $\Delta\varepsilon_v^p$  is herein assessed.  $\varepsilon_v^p$  is obtained by integrating  $\Delta\varepsilon_v^p$  of all increments. Then the volumetric strain  $\varepsilon_v$  is compared with its plastic part  $\varepsilon_v^p$  as below.

In dense and intermediate specimens,  $\varepsilon_v^p$  states almost null from the beginning and starts to dilate when  $\varepsilon_v$  reaches its minimum. Returning to the interest of this subsection, which is to identify  $\varepsilon_v^p$  on the contractant range, we find that almost no plastic volumetric contractancy in dense and intermediate specimens is observed. That means that in the contractant range there is scarcely any plastic volumetric component existing in  $\varepsilon_v$ . Therefore,  $\varepsilon_v$  derives only from the elastic part.

The discussion of subsection 3.3.3.2 and 3.3.3.3 demonstrates that in the contractant range of dense and intermediate specimens, the elastic volumetric strain, as the dominant part of the total volumetric evolution, governs the volumetric behavior of the specimen.

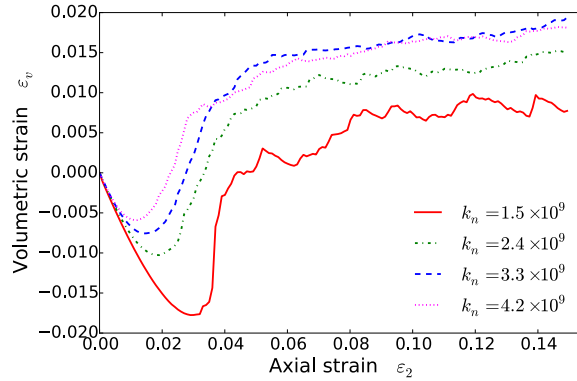


**Figure 3.17:** Evolution of volumetric strain  $\varepsilon_v$  of specimens with different elastic parameters with respect to axial strain  $\varepsilon_2$ .

### 3.3.3.4 Effect of elasticity on volumetric evolution

Since the amount of the inter-particle penetration, which dominantly affects the contractancy process, is controlled by the elastic parameters  $k_n$  and  $k_t$ , we can expect lower  $k_n$  and  $k_t$  will lead to the higher contractancy on the specimen. Following simulations thereupon are carried out to verify this expectation.

In this subsection, four dense specimens with different  $k_n$  and  $k_t$  are subjected to the drained biaxial test to compare their volumetric behavior. There are 10000 particles involved, the  $k_n$  values are set to  $k_n = 1.5 \times 10^9$ ,  $2.4 \times 10^9$ ,  $3.3 \times 10^9$ ,  $4.2 \times 10^9$  (N/m) respectively. Other parameters follow the test protocol in Table 3.1.

The volumetric evolutions in terms of axial strain  $\varepsilon_2$  are shown in Figure 3.17, volumetric minima and their corresponding  $\varepsilon_2$  are summarized in Table 3.3. The results show that as  $k_n$  decreases (the ratio  $k_t/k_n$  being constant), volumetric strain  $\varepsilon_v$  of specimens reaches its minimum lower and later. This means that the elastic parameters have strong effect on the degree of the contractancy.

**Table 3.3:** Volumetric lowest values and their corresponding  $\varepsilon_2$  for different specimens.

$k_n$ ( $1 \times 10^9$ N/m)	1.5	2.4	3.3	4.2
lowest value ( $1 \times 10^9$ )	-1.775	-1.027	-0.757	-0.590
Corresponding $\varepsilon_2$	0.029	0.019	0.014	0.012

These results meet the expectation that lower  $k_n$  and  $k_t$  will lead to the higher contractancy in the specimen. The contractancy phase at the beginning of the drained biaxial test is essentially an elastic process.

### 3.4 Force-chain interaction with meso-loop in biaxial loading path

As propagating preferentially along the major loading direction, force-chains tend to act as elastic elements in their stable configuration, constructing the sustaining part of the grain media against the external loading. The buckling of a force-chain probably leads to the loss of the sustainability in its axial direction. Practically, to be elements of the force transmission, force-chains play an essential role on ensuring the strength of the medium. The massive collapse (buckling) of force-chains, therefore, betokens the global instability of the granular assembly. On the other hand, the ability of a force-chain to maintain its linear configuration is guaranteed by the structure confining it. The degree of supporting effect offered by these confining structures differs according to their topologies. The stability of force-chains, as a result, is highly dependent on the geometrical character of the confining structure. Consequently, finding a way of characterizing the lateral structure around the force-chain is essential to understand the way force-chains interact with their neighbors and the condition of their instability. One reasonable solution is to describe the material texture into meso-loops.

The origin of the interest on the meso-loops dates back to the attempt to interpret the local discrete quantities of grains into continuum-mechanical quantities, i.e. the averaging process. The local static quantities can be conveniently linked to macroscopic stress, according to Love formula proposed in 1927 (Love, 2013; Mehrabadi et al., 1982), by holding a one-contact (or two-particle) scale. However, there is difficulty to derive the global strain from local kinematics in this scale. One-contact (or two-particle) scale, which considers contact kinematics independently from each other, is unable to completely characterize the micro-structure deformation of the granular assembly. A meso-scale is therefore introduced (Satake, 1992), on which loops are defined as enclosed inside by contact branches. In this scale, the fabric rearrangement can be featured by the geometrical evolution of loops. To date, main interests on the meso-loop stem from three aspects: (1) finding an accurate way of approximating continuum quantities (strain and stress) on the basis of the discrete static and kinematic quantities of loops (Bagi, 1996; Kruyt and Rothenburg, 1996; Kuhn, 1999); (2) characterizing the evolution of the loops in different initial states and loading paths (Kruyt and Rothenburg, 2014; Zhu et al.); (3) clarifying the interaction between force-chains and loops (Tordesillas et al., 2010, 2014). The third aspect (3) coincides with the aforementioned interest of characterizing the confining structure of force-chains.

Departing from interests in different stability-related phenomena, researches increasingly converge to investigate mechanical and geometrical features of the force-chain (Oda and Kazama, 1998; Oda and Iwashita, 2000; Iwashita and Oda, 2000; Muthuswamy and Tordesillas, 2006; Tordesillas, 2007). However, the base of how force-chains impact the material and how the confining structure, reversely, affects force-chains' stability are still mysterious. To this extent, clarifying the mechanism governing the interaction between the force-chain and its surrounding structure is of a paramount importance and, meanwhile, is a key to understand the underlying essence of stability-related phenomena in granular materials.

The aim of this section is to investigate the interaction between force-chains and their confining meso-loops along drained biaxial loading path. Numerical drained biaxial tests are performed on specimens of different initial states. Then the evolution of the number of force-chain buckling events ( $N_b$ ) and the evolution of the meso-loops are compared with macroscopic responses of each specimen, in subsection 3.4.1. In subsection 3.4.2, the way force-chains affect their confining meso-loop is investigated. Meso-structures are then distinguished into two parts: confining meso-loops (those surrounding force-chains) and reminders (those without connection to force-chains). The evolution of the former and the latter are separately statistically analyzed. In subsection 3.4.3, the confining effect of surrounding structures on force-chains is investigated, by analyzing how the status of the confining structure affects the force-chain movability. Moreover, the stress anisotropy of force-chain confining structures is discussed.

### 3.4.1 Macroscopic responses and mesoscopic evolutions

The dense and the loose specimens, which have already been analyzed in section 3.3, are also employed in this section, with their initial porosities recalled in table 3.4. The evolution of meso-structure properties are then tested, compared with their corresponding stress and strain responses.

*Table 3.4: The initial porosity of specimens.*

Specimen	Initial porosity
Dense	0.148
Loose	0.187

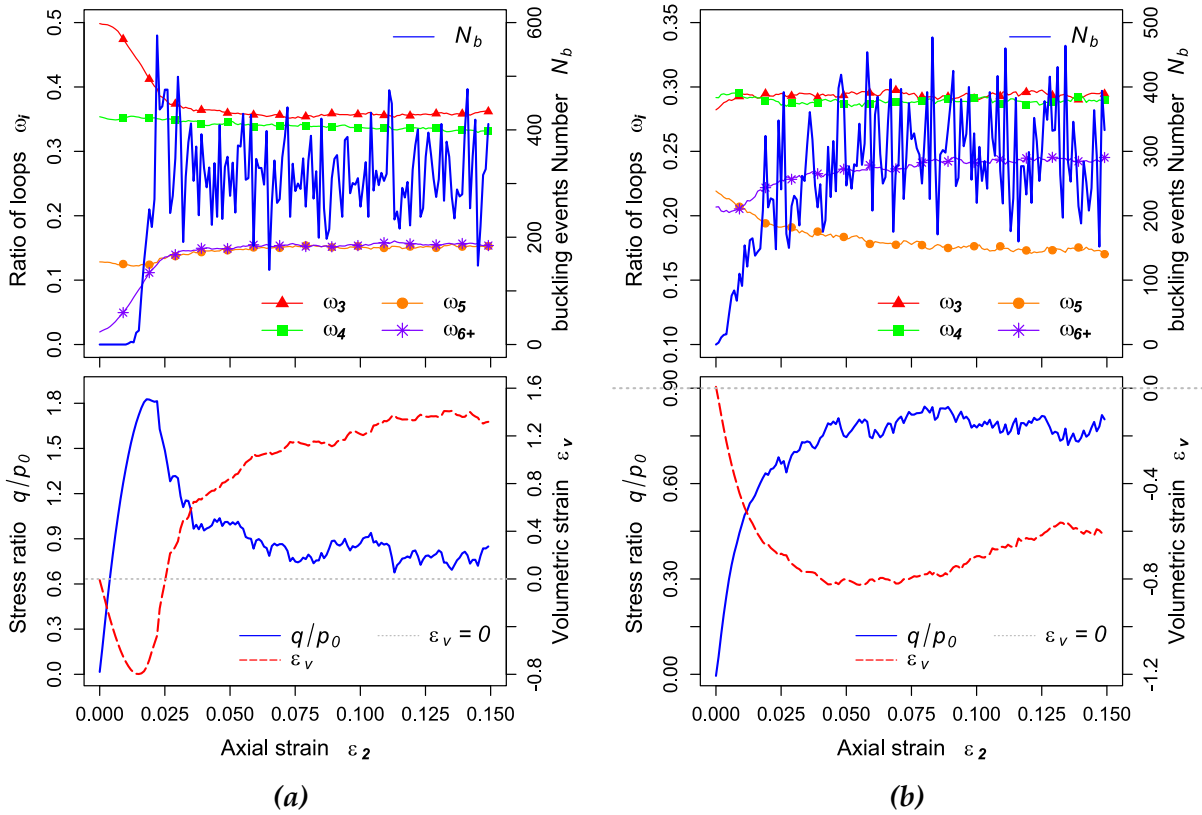


**Figure 3.18:** Evolutions of the ratio of loops  $\omega_i$ , of the number of buckling events  $N_b$  (upper), of the stress ratio  $q/p_0$  and of the volumetric strain  $\varepsilon_v$  (lower) with respect to axial strain  $\varepsilon_2$ , for dense (a) and loose (b) specimens.

The mechanical properties of different meso-loops diverge according to their geometrical nature. Among different geometrical features of loops, the side number plays a significant role on their behavior. Following the way loops are categorized in the last section (section 3.3), 4 classes  $L_i$  ( $i = 3, 4, 5, 6+$ ) are identified by employing the side number of loops.  $\omega_i$  ( $i = 3, 4, 5, 6+$ ) is the proportion of  $L_i$  over the number of all loops. In dense (Figure 3.18a) and loose (Figure 3.18b) specimens, the evolutions of  $\omega_i$  and of the number of buckling events  $N_b$  are shown with respect to axial strain  $\varepsilon_2$ , compared with the stress and the volumetric responses of specimens.

In dense specimen (Figure 3.18a),  $\omega_3$  and  $\omega_{6+}$  are the two most active categories among all kinds, developing in exactly contrary ways. The force-chain buckling starts up at the same place as the inflection point of the falling  $\omega_3$  and the rising  $\omega_{6+}$ , a little before the stress peak. Both consistent growth of  $L_{6+}$  and reduction of  $L_3$  are observed. This is finally reflected on a strong volumetric dilatancy, as large structures are continuously created with small structures perishing.

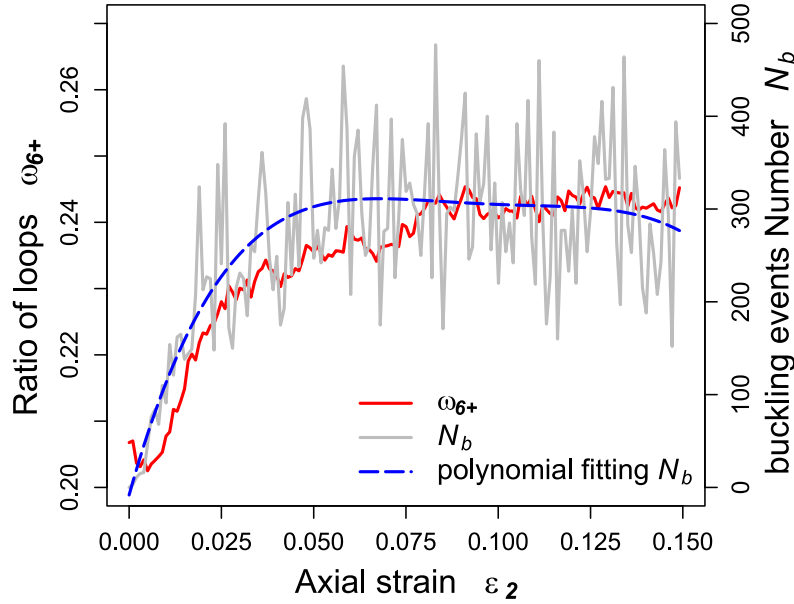


*Figure 3.19: Evolution of  $\omega_{6+}$  and of buckling events number  $N_b$  (including fitting quartic polynomial) with respect to  $\varepsilon_2$  in the loose specimen.*

In the loose specimen (Figure 3.18b),  $\omega_{6+}$  also increases its proportion among loops, except a tiny drop at the beginning, while  $\omega_5$ , oppositely, has a steady decrease.  $\omega_3$  is no longer sensitive to the biaxial loading path as in the dense specimen and keeps more or less constant, similarly to  $\omega_4$ . Especially, the force-chain buckling blasts at around  $\varepsilon_2 = 0.002$ , when  $\omega_{6+}$  also starts to increase coincidentally. An intimate correlation between  $\omega_{6+}$  and the buckling number  $N_b$  can be seen, when  $\omega_{6+}$  is compared with the quartic fitted polynomial of  $N_b$  (Figure 3.19). Meanwhile, a similar situation to the dense specimen is observed: force-chain buckling keeps a synchronous change with  $\omega_{6+}$ .

In the two above situations, the force-chain evolution is prominently dependent on the meso-loop rearrangement. Namely, it is positively correlated with  $\omega_{6+}$  and negatively correlated with  $\omega_3$ . Two questions, therefore, arise:

- Is the evolution of force-chain causally related to the meso-loop development?
- How can they interplay?

To ascertain these two questions, a more elaborate analysis is required. In subsection 3.4.2, we turn to focus on the loops close to force-chains - the area where the cross-effect between force-chains and meso-loops originally occurs.

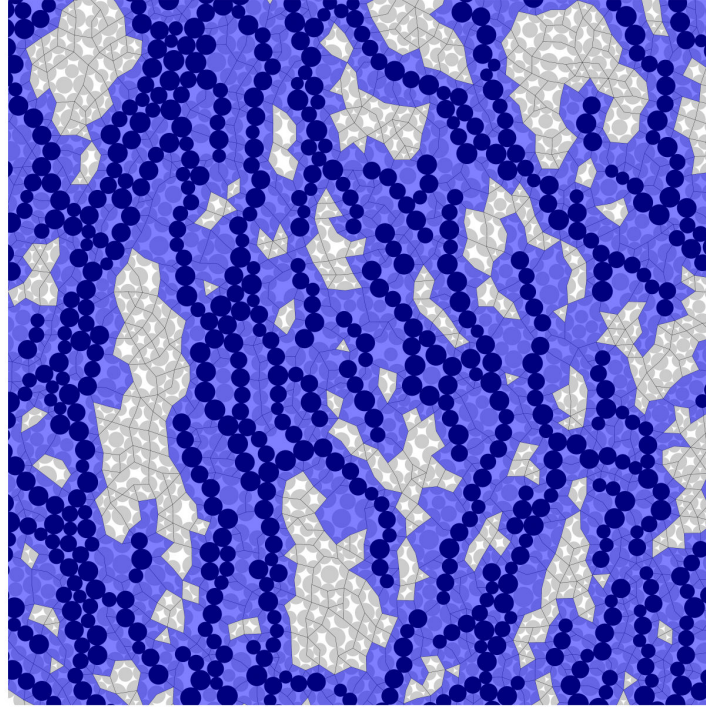


*Figure 3.20: Illustration of the force-chain loop (force-chains are in dark grey; reminding particles are grey; FCL are highlighted by the transparent shadow).*

### 3.4.2 Force-chain induced meso-loop differentiation

The granular assembly area is split into two parts, with one consisting of adjacent meso-loops around force-chains, called “force-chain loops” (*FCL*), whereas the other loops are called “not force-chain loops” (*NFCL*). As shown in Figure 3.20, *FCL* shares at least one particle with force-chain. Then properties in these two parts are analyzed to clarify whether and how (if positive) the force-chains build a special surrounding.

#### 3.4.2.1 Evolution on *FCL* and *NFCL*

The evolution of the proportion of different kinds of *FCL* ( $\omega_i^{FCL}$ ) and the buckling number  $N_b$  in terms of axial strain  $\varepsilon_2$ , is shown in Figure 3.21a (the dense specimen) and in Figure 3.21c (the loose specimen), compared with the evolution of  $\omega_i^{NFCL}$  in Figure 3.21b (the dense specimen) and in Figure 3.21d (the loose specimen).

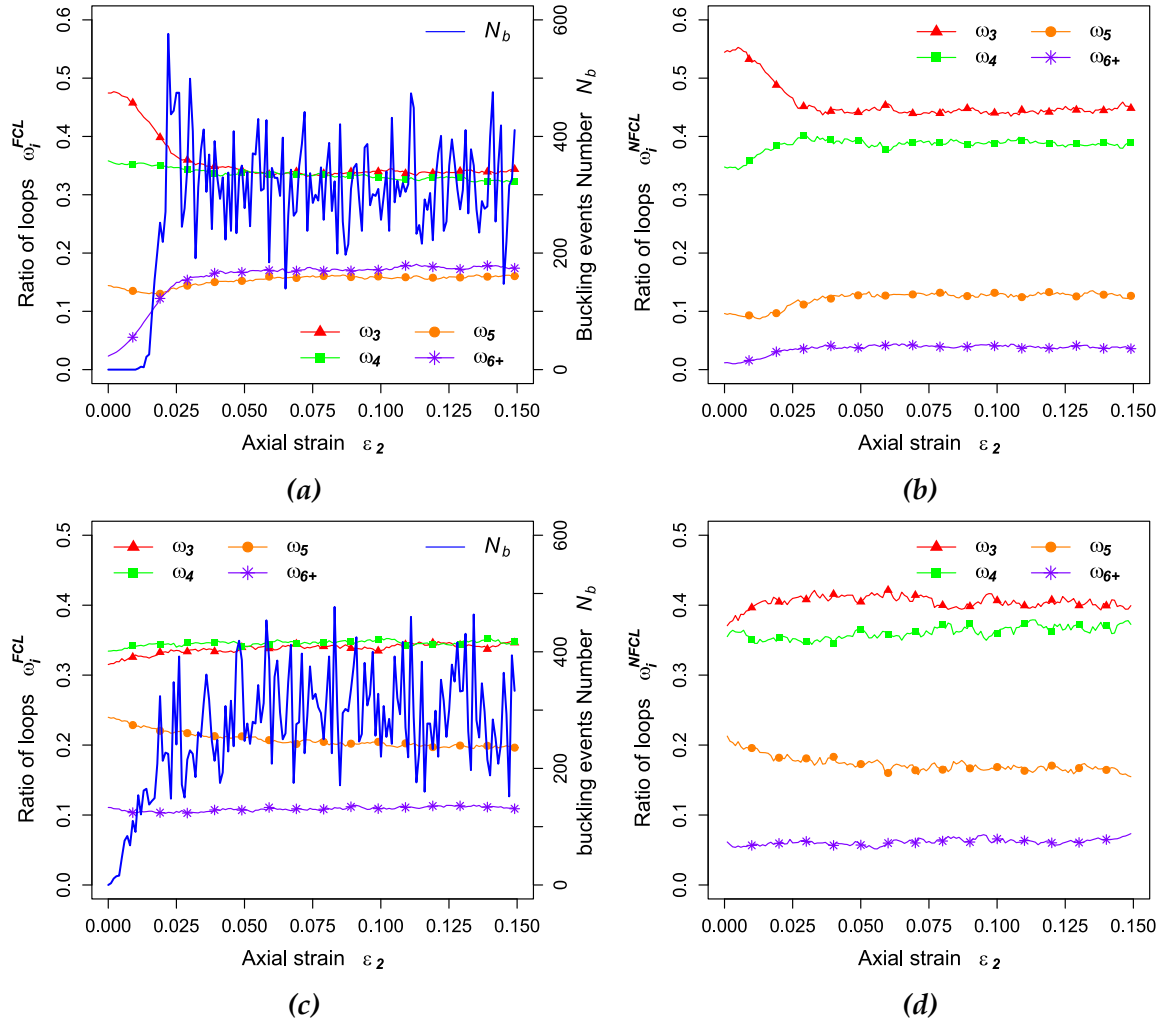


**Figure 3.21:** Evolutions of the ratio of loops  $\omega_i$  and of the number of buckling events  $N_b$  (left) with respect to axial strain  $\varepsilon_2$ . FCL in dense specimen (a), NFCL in dense specimen (b), FCL in loose specimen (c) and NFCL in loose specimen (d).

As shown in Figure 3.21a, the curves of  $\omega_i^{FCL}$  are in similar shape as those of  $\omega_i$  in Figure 3.18a. In area around force-chains,  $\omega_3^{FCL}$  and  $\omega_{6+}^{FCL}$  are observed to decrease and increase respectively with abrupt slopes, before approaching final values. On one hand, a consistent loss of firm structures and a creation of deformable structures gradually weaken the confinement of force-chains, leading to the force-chain buckling. On the other hand, the conversion from  $L_3^{FCL}$  and  $L_{6+}^{FCL}$  may also induce a volumetric expansion in the vicinity of force-chains, finally contributing to the global volumetric dilatancy.

It is worth noting that in both dense and loose specimens, significantly less  $\omega_{6+}$  and more  $\omega_3$  are observed in *NFCL* area than in *FCL* area. In dense specimen,  $\omega_{6+}^{NFCL}$  (Figure 3.21b) starts from a similar value to  $\omega_{6+}^{FCL}$ , after a slight increase, ending up at around 0.04. It is totally different from the evolution of  $\omega_{6+}^{FCL}$ , which experiences a substantial jump before stress steady state and finally stabilizes at about 0.18. There is also a consistent gap (at around 0.07) between  $\omega_3^{NFCL}$  and  $\omega_3^{FCL}$  during the whole test. In the loose specimen (Figure 3.21c and 3.21d),  $\omega_{6+}^{NFCL}$  is always about 0.03 lower than  $\omega_{6+}^{FCL}$ , while  $\omega_3^{NFCL}$  keeps the value 0.07 higher than  $\omega_3^{FCL}$ .

Huge disparity on the meso-loop distribution between *FCL* and *NFCL* indicates the existence of two absolutely different materials, diverging from the original homogeneity, under the effect of force-chains. It is prominent that in both specimens, the force-chain dominant area contains less  $L_3$  and  $L_4$  and more  $L_5$  and  $L_{6+}$  than the remaining area. Especially,  $L_3^{FCL}$  and  $L_{6+}^{FCL}$  show extremely different population levels from their corresponding values of *NFCL* area. Force-chain adjacent region, therefore, can be preliminarily considered as a locally meso-loop transformation area, where small structures transform into large ones. However, what is the exact transition pattern between different loop categories? To which extent can the variation of one kind of loop be correlated with the variation of another kind? Does the conversion relationship observed at one place (like the relation of  $\omega_3^{FCL}$  vs.  $\omega_{6+}^{FCL}$  at the beginning) keep consistently unchanged for the whole loading path, or it depends on the strain state? These questions will be discussed in subsection 3.4.2.2.

### 3.4.2.2 Conversion correlations amongst structures

The most confidential relationship between different categories observed with intuition is given by  $\omega_3^{FCL}$  and  $\omega_{6+}^{FCL}$ , which present perfect negative linear linkage with the slope being close to -1.0, see Figure 3.22. Nevertheless, merely an analysis on the total value of  $\omega_i$  is not able to figure out the subtle conversing relationship amongst different categories of loops, especially in the critical-state, when the total value of each category oscillates around a constant value. An analysis on incremental value of  $\omega_i$  ( $d\omega_i$ ) is then expected, in order to show more details on the conversion between loop categories in different phases of the loading path.

In both *FCL* and *NFCL* areas of two specimens, the loss of  $L_3$  in the fabric is basically significant and insistent over the biaxial test. According to this, the statistical analysis is aiming to investigate how a lost fraction of  $L_3$  is converted to other kinds of loop, i.e. the correlation between  $d\omega_3$  and  $d\omega_i$  ( $i = 4, 5, 6+$ ). The loading path is preliminarily

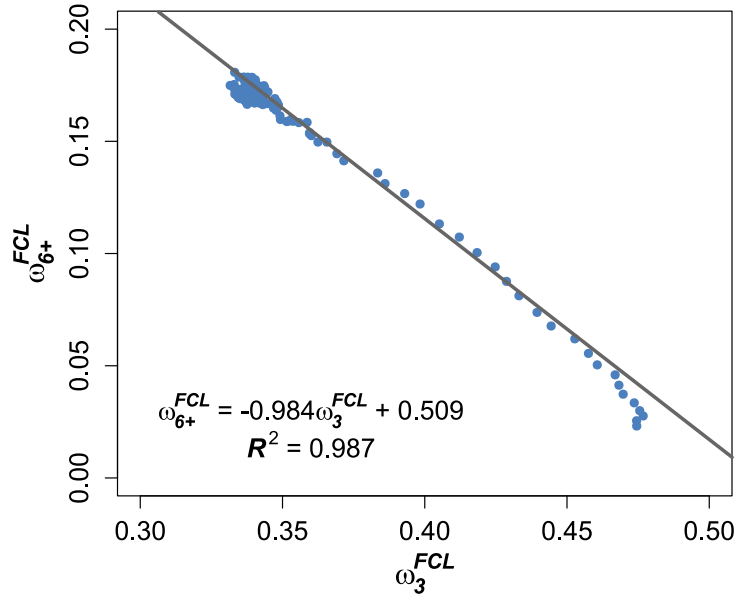


**Figure 3.22:**  $\omega_3^{FCL}$  varies as function of  $\omega_{6+}^{FCL}$ , grey line is the linear fit of scalar points.

separated into several phases. In the dense specimen, three phases can be identified: “elastic phase” ( $\varepsilon_2 = [0.000, 0.015]$ ), where the constitutive relation shows a pure elasticity with nearly no buckling occurring; “buckling phase” ( $\varepsilon_2 = [0.016, 0.060]$ ), starting from somewhere before stress peak, at which buckling events erupt, lasting until the outset of next phase; “stable phase” ( $\varepsilon_2 = [0.061, 0.150]$ ), where stress, strain and buckling events come to oscillate around a stable value. Concerning the loose specimen, as shown in Figure 3.21c, force-chains buckle from the beginning of the test; there is therefore only a small and negligible elastic initial phase. Thus, two phases “buckling phase” ( $\varepsilon_2 = [0.000, 0.070]$ ) and “stable phase” ( $\varepsilon_2 = [0.071, 0.150]$ ) can be identified for the loose specimen. The segmentation is shown in Figure 3.23.

Pearson’s correlation  $r$  (Pearson, 1895), commonly used to measure the degree of the linear correlation between two variable series, is introduced to investigate the correlation between  $d\omega_3$  and  $d\omega_i$  ( $i = 4, 5, 6+$ ), i.e. the conversing relation between  $\omega_3$  and  $\omega_i$ . The results are shown in bar plots (Figure 3.24a and 3.24b), in which bar height denotes the correlation index  $r$  of an analytical pair and I-shaped arrow is the predictive interval of  $r$  with 90% confidence. The sign of  $r$  denotes the inclination (negative or positive) of a correlation. It is worth re-iterating that the index  $r$  discussed herein evaluates the degree of the linear correlation between  $d\omega_3$  and  $d\omega_i$  ( $i = 4, 5, 6+$ ), explaining to what degree the former is depending on (or explained by) the latter.

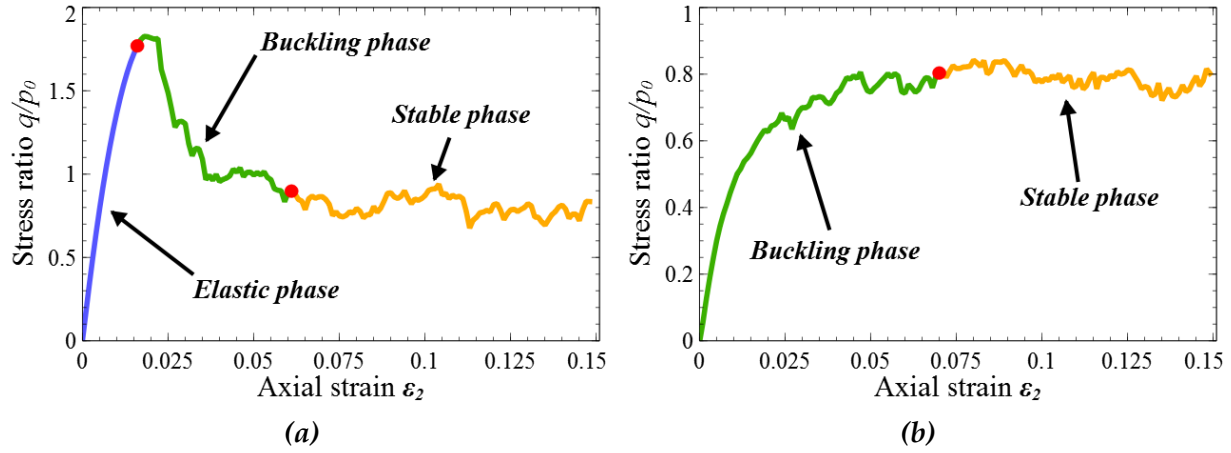


Figure 3.23: Phases on loading path for (a) dense specimen and (b) loose specimen.

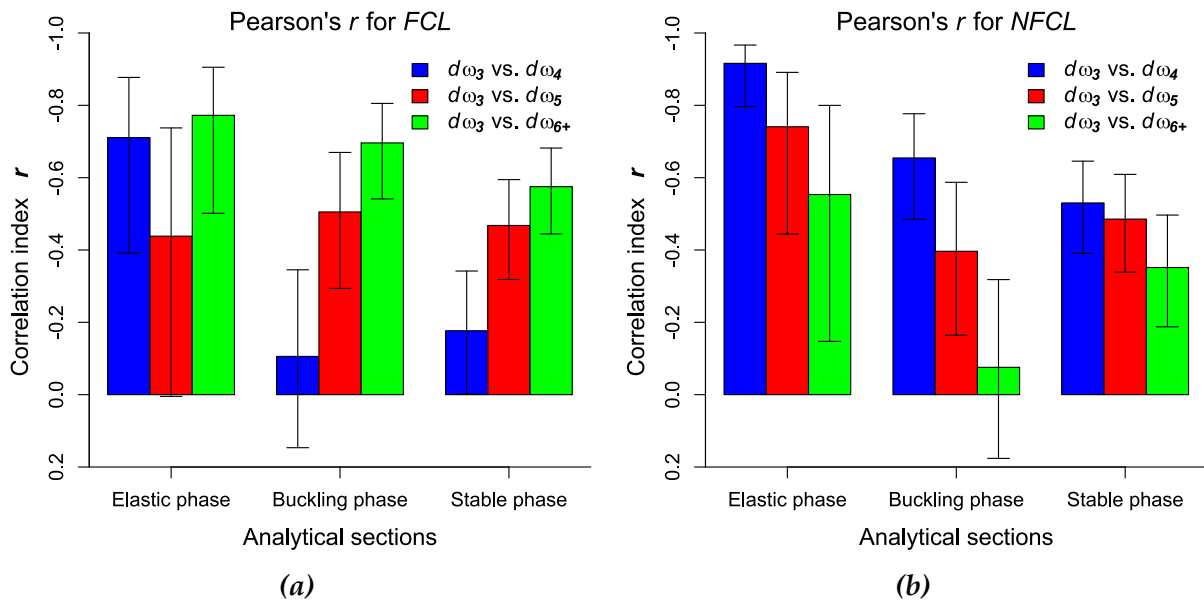
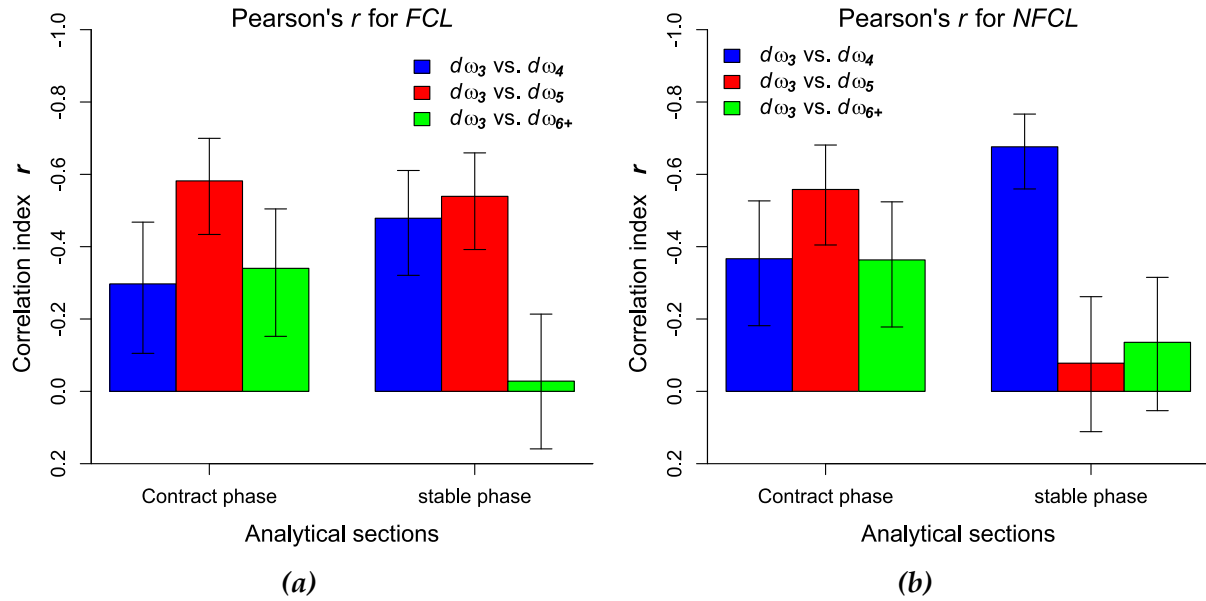


Figure 3.24: Pearson's  $r$  between  $d\omega_3$  and  $d\omega_i$  ( $i = 4, 5, 6+$ ) in three phases of the dense specimen for (a) FCL and (b) NFCL.

The results for the dense specimen, shown in Figure 3.24a, imply that in all phases,  $d\omega_3^{FCL}$  are primarily dependent on  $d\omega_{6+}^{FCL}$ , with the most concentrated predictive intervals. This is consistent with the observation in Figure 3.21a, where  $\omega_3^{FCL}$  vs.  $\omega_{6+}^{FCL}$  appears to be the most conspicuous pair, showing a clear, opposite way of evolution. In these three phases,  $d\omega_3^{FCL}$  tends to be linked to bigger loops, as  $d\omega_4^{FCL}$ ,  $d\omega_5^{FCL}$  and  $d\omega_{6+}^{FCL}$  demonstrate an orderly increasing significance of being correlated with  $d\omega_3^{FCL}$ . Mean-



**Figure 3.25:** Pearson's  $r$  between  $d\omega_3$  and  $d\omega_i$  ( $i = 4, 5, 6+$ ) in two phases of the loose specimen for (a) FCL and (b) NFCL.

while, in NFCL area (Figure 3.24b), the variation of  $d\omega_3^{NFCL}$  can be mainly explained by the variation of  $d\omega_4^{NFCL}$ , with the most concentrated predictive intervals. Otherwise, in “elastic phase” and “buckling phase”, the linkage between  $d\omega_3^{NFCL}$  and  $\omega_{6+}^{NFCL}$  displays some uncertainty, with wide confidential intervals.

In the loose specimen (Figure 3.25), in the “buckling phase”, the correlation patterns in both FCL and NFCL areas are similar; as shown in Figure 3.25a and 3.25b, in the “buckling phase”,  $d\omega_3$  vs.  $d\omega_5$  has the highest level of  $r$  (around 0.6) among pairs and the corresponding values for  $d\omega_3$  vs.  $d\omega_4$  and  $d\omega_3$  vs.  $d\omega_{6+}$  are equivalently secondary. In the “stable phase”,  $d\omega_3^{FCL}$  is mainly correlated with  $d\omega_4^{FCL}$  and  $d\omega_5^{FCL}$ , however,  $d\omega_3^{NFCL}$  is only dependent on  $d\omega_4^{NFCL}$ .

The correlation index  $r$  between  $d\omega_3$  and  $d\omega_i$  ( $i = 4, 5, 6+$ ) can be interpreted as the conversion relationships between  $\omega_3$  and the ratio of other loops. In the dense specimen, FCL area tends to convert  $L_3$  to big loops, as we see a descending preference on “ $L_3 \rightarrow L_{6+}$ ”, “ $L_3 \rightarrow L_5$ ” and “ $L_3 \rightarrow L_4$ ”, while NFCL exactly reverses this pattern, to be apt to translate  $L_3$  to small loops; for the loose specimen, in the “buckling phase”, the conversion patterns in both FCL and NFCL areas are similar. In the “stable phase”,

transports from  $L_3^{FCL}$  to  $L_4^{FCL}$  and  $L_5^{FCL}$  are more or less equivalent. However, the loss of  $L_3^{NFCL}$  in “stable phase” is almost only transferred into the  $L_4^{NFCL}$ . This is in line with the case of the dense sample, where *FCL* area, compared with *NFCL* area, is inclined to change  $L_3$  into bigger loops.

As a result, we confirm again that *FCL* and *NFCL* areas should be treated as two different materials, with regard to the meso-loop evolution. The areas far from force-chains lack the ability to generate big loops, compared with the force-chain surrounding area. In the process of volumetric expansion directed by the loading path, the force-chain acts as an intermediate agent of “sacrificing” small, firm structure (e.g.  $L_3$ ) and “creating” big, flexible ones (e.g.  $L_{6+}$ ). *FCL* area has more instinct to expand its volume, i.e. the meso-scale volumetric dilatancy (*MV-D*). Thus, the force-chain area can be seen as the main source and the major contributor to the macroscopic dilatancy.

### 3.4.2.3 Volumetric behavior

Coming back to the analysis of the volumetric change, different patterns of meso-loop evolution may lead to a density inhomogeneity inside and outside force-chain areas. Therefore, the void ratio  $e$  (respectively inside, outside force-chain areas and in total area) of specimens is plotted in Figure 3.27. It should be noted that the void ratio only concerns the area enclosed by loops, given by  $e = (V_{total} - V_{solid})/V_{solid}$ . In Figure 3.26,  $V_{total}$  (inside *ABCDEFGF*) corresponds to the total area of collective loops and  $V_{solid}$  (shadowed area) is the solid area encircled by the contact branches of these loops, where *ABCDEFGF* are respectively centers of particles.

The results show that in both dense and loose specimens, void ratio  $e$  in the force-chain surrounding area is consistently higher than that in the total and in the *NFCL* area. From a macro-scale viewpoint, this supports the conclusion that the force-chain area is more inclined to create big loops than the remaining area, dilating more than remaining area.

So far, the force-chain induced dilatancy can be treated as a kind of material self-organization around force-chains. The original homogeneous material develops its structure in close connection with the force-chains, which are congenitally heterogeneous and anisotropic. This small scale self-organization is significant, as it cumulates, conjugates and finally leads to larger scale structuring phenomena, as for example the formation of the shear band or more generally, the strain-localization (Alshibli and Sture, 2000; Oda and Iwashita, 2000; Gu et al., 2014). Otherwise, the different dilatability between the force-chain adjacent area and the area far from force-chain is assumed to

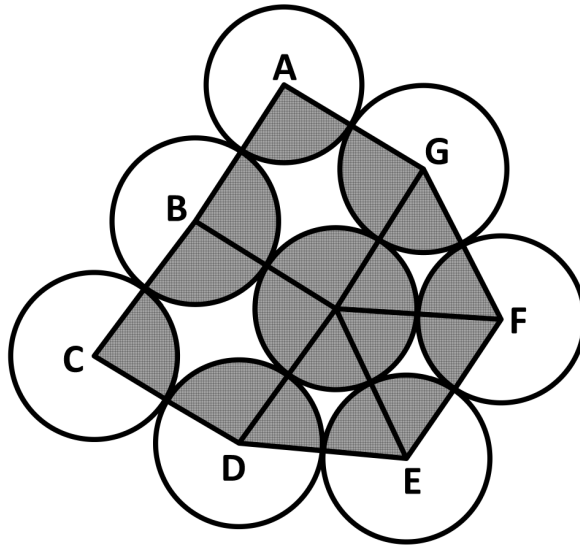


**Figure 3.26:** An illustration of the total area and the solid area (shaded) in a set of loops (inside ABCDEFG).

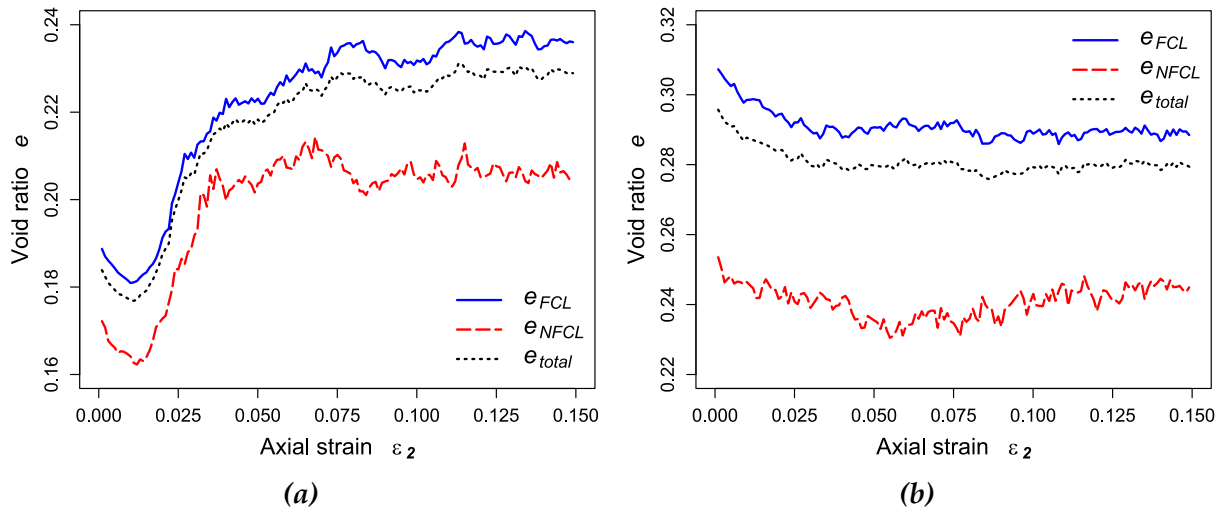


**Figure 3.27:** Evolutions of void ratio  $e$  of FCL, NFCL and total area in (a) dense and (b) loose specimens with respect to  $\varepsilon_2$ .

be attributed to the different moving pattern of these two areas. It is revealed by former researches that rotating pattern, instead of sliding, prevails in force-chain contacts (Bardet, 1994; Oda, 1997; Oda and Kazama, 1998; Tordesillas, 2007). Of course, the casual relation between moving pattern and ability of creating big structure is recommended to be investigated in detail.

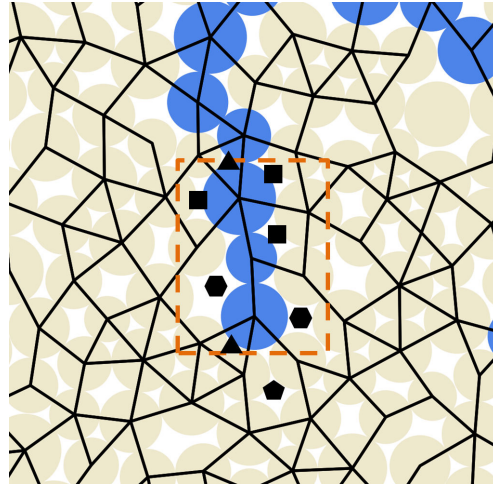


Figure 3.28: Confining structures and force-chain movability.

### 3.4.3 Effect of confining structures on force-chains

The investigation above concerns the interest of how force-chain affects the meso-loop. However, the meso-loop morphology may reversely play a role on the force-chain evolution in a certain way. From here forwards, the analysis is led in this sense.

#### 3.4.3.1 Confining structures and force-chain movability

The buckling angle  $\theta_b$ , aforementioned in section 3.2, characterizes the deformation of a 3-particle set, the force-chain element. We calculate  $\theta_b$  of all 3-particle sets and meanwhile count the number of loops  $L_i$  connected to each 3-particle set,  $N_i$  ( $i = 3, 4, 5, 6+$ ). Figure 3.28 gives an example of a 3-particle set and its connected loops, which are labeled by polygonal symbols according to their shapes. In this case, as shown by symbols,  $N_3 = 2$ ,  $N_4 = 3$ ,  $N_5 = 1$  and  $N_{6+} = 2$ .

Statistical analyses on the buckling angle  $\theta_b$  for different levels of  $N_i$  ( $i = 3, 4, 5, 6+$ ) are then implemented and presented in Figure 3.29, in order to investigate how the force-chain movability varies in terms of the composition of its surrounding meso-loops. Two strain states are chosen to be analyzed: one state in the dense specimen at  $\varepsilon_2 = 0.018$ , short before stress peak; and another state in the loose specimen at  $\varepsilon_2 = 0.050$ , when the stress tends to be stable. Four subplots correspond to four different loop categories  $L_i$  ( $i = 3, 4, 5, 6+$ ). In subplot of  $L_i$ ,  $\theta_b$  of all 3-particle sets are statistically analyzed with respect to their  $N_i$ . Taking  $L_3$  as an example, shown in the upper-left subplot of Figure 3.29a and 3.29b, all 3-particle sets have their respective  $\theta_b$  and  $N_3$ , forming data points in the space  $\log(\theta_b) - N_3$ . Then at each level (data columns) of  $N_3$ , different

statistical quantities of  $\log(\theta_b)$ , e.g. the median, are calculated. These statistical quantities of  $\log(\theta_b)$  involve five elements in each level of  $N_3$ : the first quartile  $Q_1$ , the box downside; the median quartile, the black cross-line; the third quartile  $Q_3$ , the box upside; the inter-quartile range  $IQR$  (I-shaped arrow); and the outer-quartile scattered points (Miller et al., 1965). Among these five quantities, the median quartile is the most significant element, which is the median of a data column, while other elements reflect the concentration degree of this data set at different levels. Function  $\log(\theta_b)$  is prescribed instead of  $\theta_b$ , because the density function of  $\theta_b$  distribution shapes too far from normal distribution to be statistically analyzable.

Results from loose and dense specimens are extremely similar. This indicates that the confining effect on force-chain, given by a certain surrounding meso-loop composition, is independent from the strain state and the buckling degree. The movability of force-chains tends to decrease, if they are more confined by  $L_3$ . On the contrary, they become movable, if there are more  $L_{6+}$  around them. On the whole,  $L_3$ , as well as  $L_4$ , imposes a negative effect on force-chain movability, while  $L_{6+}$  and  $L_5$  give rise to a positive effect.

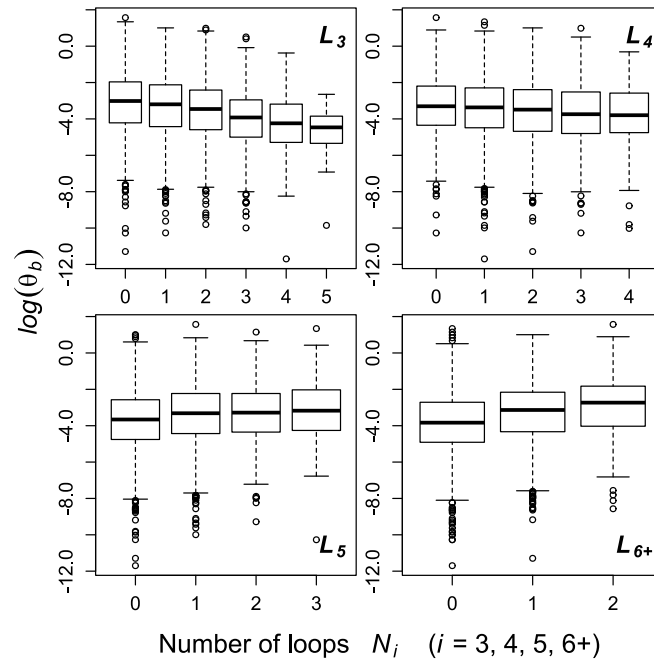
It is concluded that  $L_3$ , a kind of dense, firm meso-loop, certainly locks force-chain's kinematical freedoms and handicaps its movement, whereas  $L_{6+}$  offers force-chain more freedom degree and therefore more movability. It is in line with the results shown in Figure 3.19 and 3.21a, where the evolution of  $\omega_3$  and  $\omega_{6+}$  is respectively negatively and positively correlated with the degree of force-chain buckling. Basically, the movability of force-chains is a crucial attribution, dictating the behavior of the force-chains and, even further, the macroscopic behavior of the granular material. Even though the concept of "movability" only belongs to the ambit of kinematics, force-chains with more movability can evolve to a buckled configuration more easily and rapidly. This commonly causes a loss of their sustainability, i.e. the force-chain instability.

Finally, the life-cycle of force-chains can be displayed as a history of interaction with their confining meso-loops, as shown in Figure 3.30.

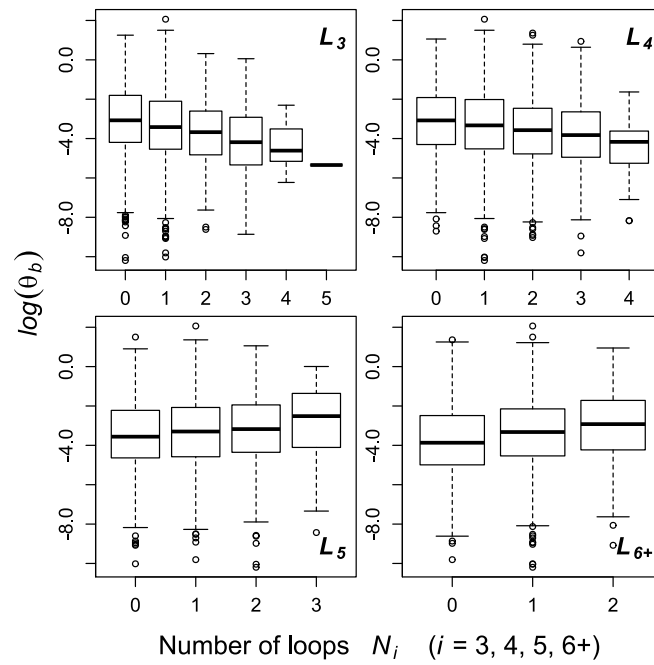
### 3.4.3.2 Stress anisotropy of confining loops

In order to measure the stress on the meso-scale, we introduce a stress tensor in the meso-scale, called loop stress tensor, proposed by SAS (1997):

$$\tilde{\sigma}_{ij}^L = \sum_{c=1}^{N_c} \frac{f_i^c l_j^c}{\tilde{v}^c} \quad (3.13)$$



(a)



(b)

Figure 3.29: Quartiles of  $\log(\theta_b)$  of 3-particle sets for different levels of  $N_i$  ( $i = 3, 4, 5, 6+$ ) for (a)  $\epsilon_2 = 0.018$  in the dense specimen and (b)  $\epsilon_2 = 0.050$  in the loose specimen.

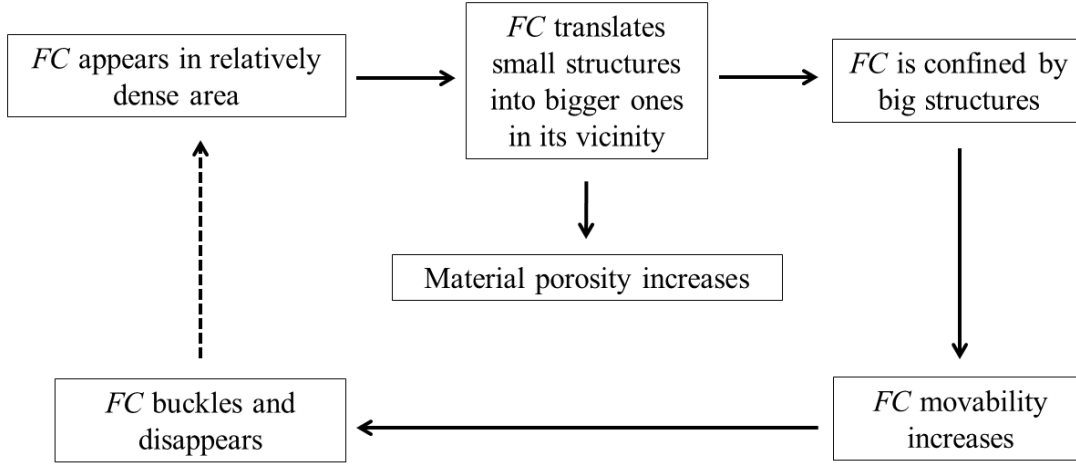


Figure 3.30: Force-chain life-cycle.

where  $N_c$  denotes the number of contacts over the considered loop,  $f_i^c$  and  $l_j^c$  are respectively the  $i$ th component of the contact force and the  $j$ th component of the contact branch on contact  $c$ ,  $\tilde{v}^c$  is the combining area of two neighboring loops sharing the contact  $c$ . In Figure 3.31, there is an illustration of calculating  $\tilde{\sigma}_{ij}^L$  of the considered loop.  $\tilde{v}^{CD}$  is the total area of *loop 0* and *loop 1*. To note is that this method of building the local mesoscopic stress tensor is only one among different ways of characterizing the local stress (Nguyen et al., 2012; Nicot et al., 2013). The normalized deviator of  $\tilde{\sigma}_{ij}^L$  is given by:

$$D^{meso} = \frac{\tilde{\sigma}_1^L - \tilde{\sigma}_2^L}{\tilde{\sigma}_1^L + \tilde{\sigma}_2^L} \quad (3.14)$$

$\tilde{\sigma}_1^L$  and  $\tilde{\sigma}_2^L$  are respectively the major and the minor eigenvalue of  $\tilde{\sigma}_{ij}^L$ . Then  $D_i^{meso}$  for each kind of force-chain loop  $L_i$  can be calculated. Its evolution as a function of  $\varepsilon_2$  is illustrated in Figure 3.32.

In both specimens,  $D_3^{meso}$  and  $D_{6+}^{meso}$  respectively stay at the lowest and highest values over the loading path.  $D_4^{meso}$  and  $D_5^{meso}$  behave extremely similarly and range between  $D_3^{meso}$  and  $D_{6+}^{meso}$ . This indicates that the area of  $L_3^{FCL}$  could be considered as in a quasi isotropically stressed environment, while the stress in  $L_{6+}^{FCL}$  structures is more anisotropically distributed. Force-chains with more  $L_3^{FCL}$ , compared with those with more  $L_{6+}^{FCL}$ , tend to transmit larger forces to their lateral environment. As a result, in stress-controlled boundary conditions, the boundary movements depend on the constitution of different kinds of meso-loops around force-chains. Specifically in drained biaxial tests, when subjected to an incrementally axial loading, force-chains in dense

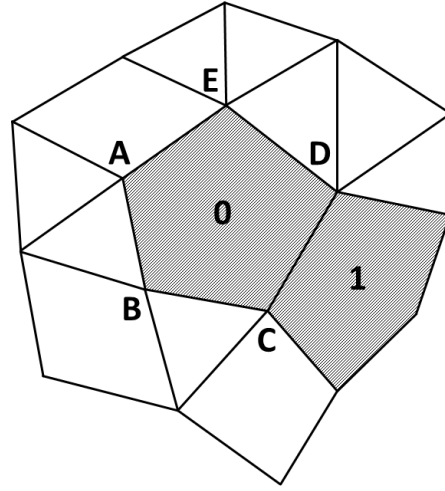


Figure 3.31: An illustration of calculating the loop stress tensor  $\tilde{\sigma}_{ij}^L$ . The loop considered here is loop 0 (or loop ABCDE),  $\tilde{v}^{CD}$  is the total area of loop 0 and loop 1.

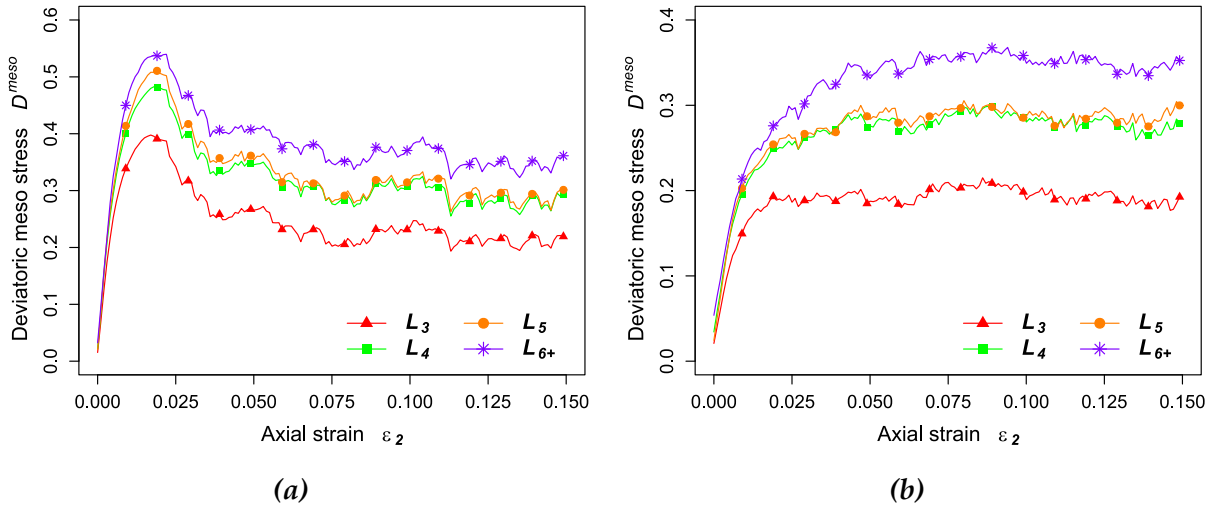


Figure 3.32: Evolutions of normalized deviatoric meso stress  $D^{meso}$  with respect to  $\epsilon_2$  in (a) dense and (b) loose specimens.

specimens, mainly consisting of  $L_3$ , impose stronger lateral forces on the side boundary than looser specimens do. Then, for dense specimens, the lateral boundaries have to move outward, in order to keep the lateral pressure constant. Whereas this is not true for loose specimens, as the lateral forces directed by the force chains is much smaller. This probably leads to a contractancy. Therefore, it is concluded that along the biaxial loading path,  $L_3^{FCL}$  leads the assembly to dilate, and  $L_{6+}^{FCL}$  leads the assembly to contract.

The mechanism described above has two significant consequences on the macro-scale:

1. According to the initial fabrics (related to the initial void ratio, together with the deposit method), a loading path will direct dilatancy or contractancy. When a dilatancy occurs,  $L_3$  loops are no longer compatible with the volume expansion, leading to a transition from  $L_3$  to  $L_6$ .
2. When the texture adjusts itself (in terms of  $L_3$  versus  $L_{6+}$ ), to match the global volumetric variation induced by boundary adjustment, the movability of force-chain also changes. When the ratio of  $L_{6+}$  increases (especially  $L_{6+}^{FCL}$  increases), the stability of force chains is no longer insured. The number of buckling force-chains increases dramatically, leading to a strength softening after stress peak.

Generally saying, there is an inherent “feedback-control” mechanism that can be observed along the biaxial loading path. The anisotropy of the force-chain surrounding area, which depends on the current composition of force-chain loops, determines the boundary motion. Reversely, the boundary motion will also change the nature of force-chain loops. As a consequence, the loading path and force-chain confining structures mutually adjust themselves to converge towards a steady state, corresponding to a certain fabric, where the proportion of different meso-loops comes to take a constant value. This leads to a constant degree of stress anisotropy and a constant specimen volume, as observed during the so-called “*Critical State*” (Roscoe et al., 1958; Schofield and Wroth, 1968).

### 3.5 The critical state meso-structure in localized and diffuse failure modes

Granular material has attracted great interest in recent decades, as an idealized model of frictional material. Its behavior diverges sensitively according to the initial state and the loading history, i.e. the initial state and a path dependence. It is also well-known that despite the diversity of the response, in the large strain of biaxial compression, the granular material evolves towards a steady state, in which a shear distortion progresses without any change in the shear stress or the material volume. This state, being independent of the initial state, is named Critical State. Since this concept was introduced by Roscoe et al. (1958) and developed as Critical State Soil Mechanics

(CSSM) by Schofield and Wroth (1968), it has been the corner stone of soil mechanics for decades, allowing researchers to build the constitutive relation for the final state of soil, as well as other granular materials (e.g. Roscoe and Purland, 1968; Wan et al., 2011; Li and Dafalias, 2012; Zhao and Guo, 2013; Gao et al., 2014).

The critical state relation in  $p'$ - $q$ - $e$  space is called critical state line (CSL). As an asymptotic state for granular assembly subjected to prescribed loading path, it gives a trinary relation among void ratio  $e$ , the mean effective stress  $p'$  and the deviatoric stress  $q$ . In the large strain,  $e$  becomes constant with  $p'$  and  $q$  stopping increasing as well. Basically, constant  $e$  is considered as the signature of the critical state. However, two questions should be asked before accepting this concept: why is  $e$  so crucial among different state quantities, and how can critical state  $e$  be related to the critical state stress? The physical meaning behind it is of great interest for researchers. Given the critical state concept is initiated on the basis of macro-scale observations, the answer should be found on a smaller scale. Viewed in micro-scale, global stress response is attributed to contact forces projected on different planes. As a result, the mechanical response of granular materials basically depends on the contact fabric arrangement (Oda et al., 1980; Rothenburg and Bathurst, 1989). Therefore, one possible answer to the former two questions may be that in the critical state, there exists a characteristic fabric in the micro-scale, which has a relatively constant void ratio and an unchanged mechanical response, disregarding the persistent shear deformation. Many attempts have been made to investigate fabric features in the shear deformation and its role in macroscopic mechanical response of granular material (Cambou, 1993; Radjai et al., 2004; Cambou et al., 2009).

In the classic critical state framework founded by Roscoe et al. (1958), the critical state is featured as an isotropic deformation pattern, when structureless state quantity, void ratio  $e$ , is introduced to characterize the material state. The pioneering work of Oda (1972a,b,c) in statistically characterizing the directional contact distribution in granular materials, highlights the existence of the shear induced anisotropic fabric in the critical state. This compels the geo-mechanics community to recognize the foundation of shearing deformation in a new way, a fabric viewpoint. Taking advantages of the new numerical tool, the discrete-element method DEM (Cundall and Strack, 1979), and the progress of experimental techniques, many later observations confirm that the shear induced fabric anisotropy prevails during or even before the critical state, acting as a signature of shear deformation (Thornton and Barnes, 1986; Rothenburg and Bathurst, 1989; Calvetti et al., 1997; Thornton and Antony, 1998; Mueth et al., 2000; Fu and Dafalias, 2011; Hasan and Alshibli, 2012; Zhao and Guo, 2013). While more fabric

features are identified in shear deformation, the critical state is expected to be of fabric dependence (Been and Jefferies, 1985). The physical essence of the shear deformation and the critical state mechanical behavior should be investigated on the micro-mechanical level, by considering the force and the material fabric of granular assemblies. In terms of describing the fabric, the necessity of taking the meso-scale viewpoint has already been explained and confirmed in previous sections. Behaviors of force-chains and meso-loops should be characterized during the granular assembly develops the shear deformation until reaching the critical state. How these behaviors on the meso-scale leads to the critical state mechanics turns to be a challenging topic.

There is another concern in practicing critical state concept when considering the material structurization. In some cases, failure occurs homogeneously without any apparent and persistent strain concentration, called “*diffuse failure mode*” (Darve and Roguiez, 1998; Darve et al., 1995a, 2004). It is also well-known that granular assembly under shearing may experience a transition from a homogeneous deformation pattern to a discontinuous one, with strain largely localizing into a system of bands, i.e. “*shear band*”. As soon as that occurs, the material is structurized into two zones: shear band domain, where strain concentrates; and remaining domain, where material undergoes an elastic unloading to release its stored elastic energy (Nicot and Darve, 2011a). This failure pattern is called “*localized failure mode*” (Rice, 1976; Bigoni and Hueckel, 1991; Bigoni, 2000; Chambon and Cailherie, 1999; Petryk, 1993; Tejchman and Górski, 2008; Vardoulakis et al., 1978; Vardoulakis and Sulem, 1995). In the presence of the structurization in specimen scale, average state quantity of the whole material is no longer valid. Instead, the state should be described separately in different parts. This notion is reminiscent of what Oda (1972a) did in investigating deformation mechanism of dense specimens under triaxial compression, where sample volume is subdivided into several parts with respect to their void ratios. The shear deformation only occurs inside the shear band when the other domain, as a whole, acts in a quasi-elastic behavior. Hence, the non-elastic property of the material largely derives from the shear band domain, where shear deformation is dominantly active. This means that the fabric base of the critical state should be discussed more inside shear band (e.g. Fu and Dafalias, 2011).

The aim of this section is to characterize the critical state fabric on the meso-scale of granular material in both localized and diffuse failure modes. 2D drained biaxial tests were carried out in different initial states, as introduced in subsection 3.5.1. According to the relative displacement fields and strain fields extracted from tests, in subsection 3.5.2, the failure mode of each specimen was determined, shear band width of localized specimens was assessed. In subsection 3.5.3, a convergent critical state void ratio is validated

in failure area of specimens instead of in whole specimen area. In subsection 3.5.4, two kinds of meso-structure, meso-loop and force-chain, are taken into account. Their different mechanical properties are investigated to clarify, from different aspects, whether there exists a convergent meso-structure in the failure area as the signature of critical state.

### 3.5.1 Drained biaxial test and results

Four specimens, S1, S2, S3 and S4, with different initial void ratios  $e_0$  (given by equation 2.9) are installed and subjected to the drained biaxial test, according to the parameters and the test protocol prescribed in section 2.2. They are listed with their corresponding  $e_0$  in table 3.5, where specimens are ascendingly ordered and numbered according to  $e_0$ . The method to assess the void ratio will be introduced in subsection 3.5.3.

*Table 3.5: Specimens and corresponding initial void ratio.*

Specimen	$e_0$
S1	0.185
S2	0.200
S3	0.246
S4	0.297

Macroscopic responses of four tested specimens are illustrated in Figure 3.33, in which stress ratio  $q/p_0$ , volumetric strain  $\varepsilon_v = -(\varepsilon_1 + \varepsilon_2)$  and void ratio  $e$  evolve as function of axial strain  $\varepsilon_2$ .

Results present typical stress and strain responses of drained biaxial test. When initial  $e_0$  increases, the specimens' stress turns from softening (specimen S1, S2 and S3) to hardening (S4) and meanwhile from dilating (S1 and S2) to contracting (S3 and S4). Densest specimen S1 sees the largest stress drop after peak, accompanied by the strongest bulk dilatancy. Stress peaks fade gradually from S1 to S3 and vanish in S4. To be the function of  $\varepsilon_v$ , the specimens' void ratio resembles  $\varepsilon_v$  evolution. Around after  $\varepsilon_2 = 0.12$ , all these macroscopic quantities calm down to a steady state with small oscillation. In agreement with what the critical state predicts, the stress ratios of four specimens converge to fluctuate at about 0.8. However, the void ratios do not converge in the end as expected. This is due to the structurization of material. As aforementioned, when localization occurs, to treat the material as a whole is no longer valid in describing mechanical state of the material. Thereupon, the localization patterns of 4 specimens will be investigated in subsection 3.5.2.

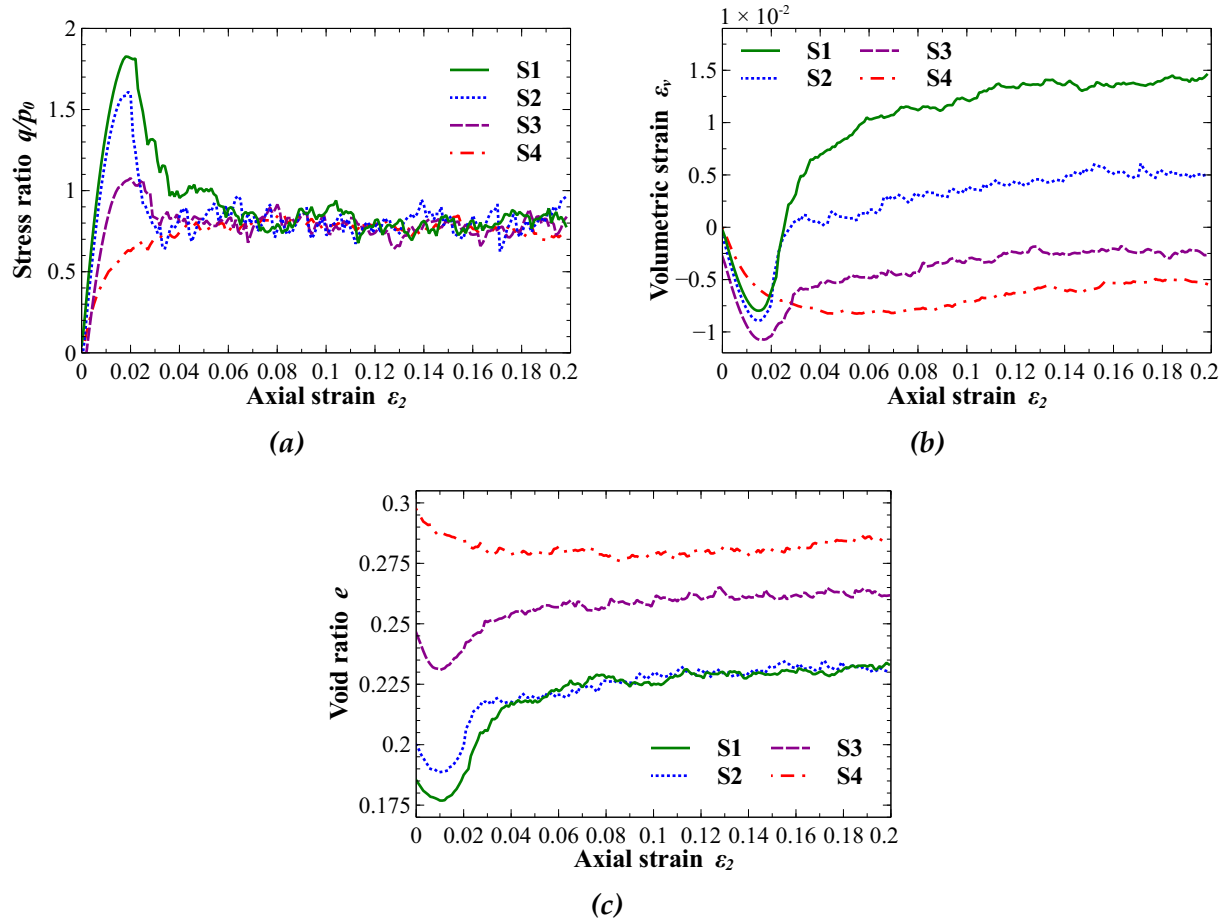


Figure 3.33: Evolutions of stress (a), strain (b) and void ratio  $e$  (c) with respect to axial strain  $\varepsilon_2$ , in specimens S1, S2, S3 and S4.

### 3.5.2 Failure modes and shear band width in specimens

The localized failure, according to its definition, refers to the state where the strain largely concentrates in partial domain of material, on the contrary to the diffuse mode. In this subsection, relative displacement between contact particles  $|\Delta u|$  (i.e. the increment of the contact vector) is used to demonstrate the failure mode in specimens. Nephograms of  $|\Delta u|$  field for all specimens are plotted in the strain state  $\varepsilon_2 = 0.150$  (see Figure 3.34), when it is assumed to be already in the critical state.

In S1, S2 and S3 (Figure 3.34a 3.34b 3.34c respectively), relative displacement blasts in a diagonal area transversing whole specimen to form a shear band. This is a typical localization failure appearing after stress peak. In fact, for the purpose of obtaining a diagonal pattern of localization linking corners of the specimen, the initial dimension of the specimens are set to  $0.90 m \times 1.35 m$ , under the enlightenment of the parameters

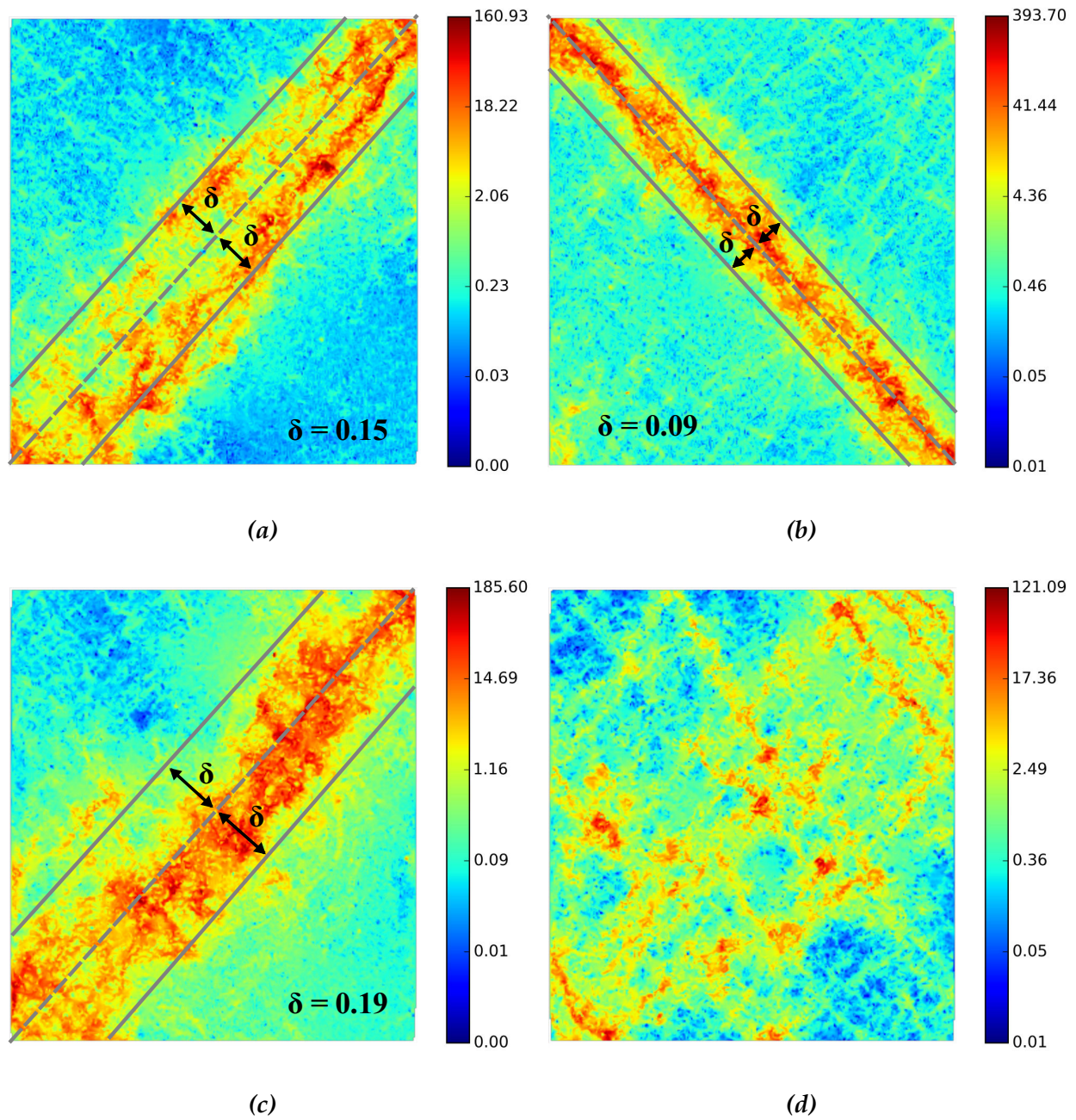


Figure 3.34:  $|\Delta u|$  nephogram ( $10^{-5}$  m) for specimen S1 (a), S2 (b), S3 (c) and S4 (d). Shear bands are bounded by grey lines with width  $2\delta$ .

used in the work by Nguyen et al. (2009). S2 has the most concentrated shear area within a narrow band, that also leads to the highest localized value of  $\Delta u$  amongst specimens, being equal to 3.9 mm. The deformation pattern in S4 (Figure 3.34d) is

significantly different, as the displacement scatters over the material. Even though an uneven displacement also exists in some banded domains, the trail of these domains is blurry and complicated. This uneven displacement is also temporary and variable, as it is found to change with different strain states. This failure pattern is quite far from the localized mode where a clear and steady shear band can be figured out once being formed. This mode is considered as a diffuse mode.

To decide the width of the shear band, the strain  $\varepsilon$  is calculated on the basis of the relative displacement field  $\Delta u$

$$\varepsilon_{ij} = \frac{1}{2} \left( \frac{\Delta u_i}{\Delta x_j} + \frac{\Delta u_j}{\Delta x_i} \right), \quad (3.15)$$

where  $\Delta x_i$  denotes the increment of the  $i$ th global coordinate,  $\Delta u_i$  is the  $i$ th component of relative displacement increment. The compressive deformation is considered to be positive. As it is observed in Figure 3.34, we assume that the shear band extends symmetrically from diagonal. The width of the shear band is indicated by  $2\delta$ , when  $\delta$  is the distance from the shear band upper or lower boundaries to the diagonal, as illustrated in Figure 3.35.

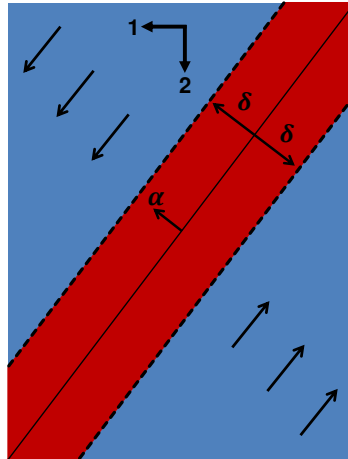


**Figure 3.35:** The profile of diagonal shear band, framed between two dashed lines. The shear band is assumed to extend symmetrically from diagonal (the continuous line from left-bottom to right-top corner in this figure), and the extension distance is denoted by  $\delta$ . A coordinate  $\alpha$  is set perpendicularly to the diagonal, as shear band lower and upper boundaries respectively correspond to  $\alpha = -\delta$  and  $\alpha = \delta$ .

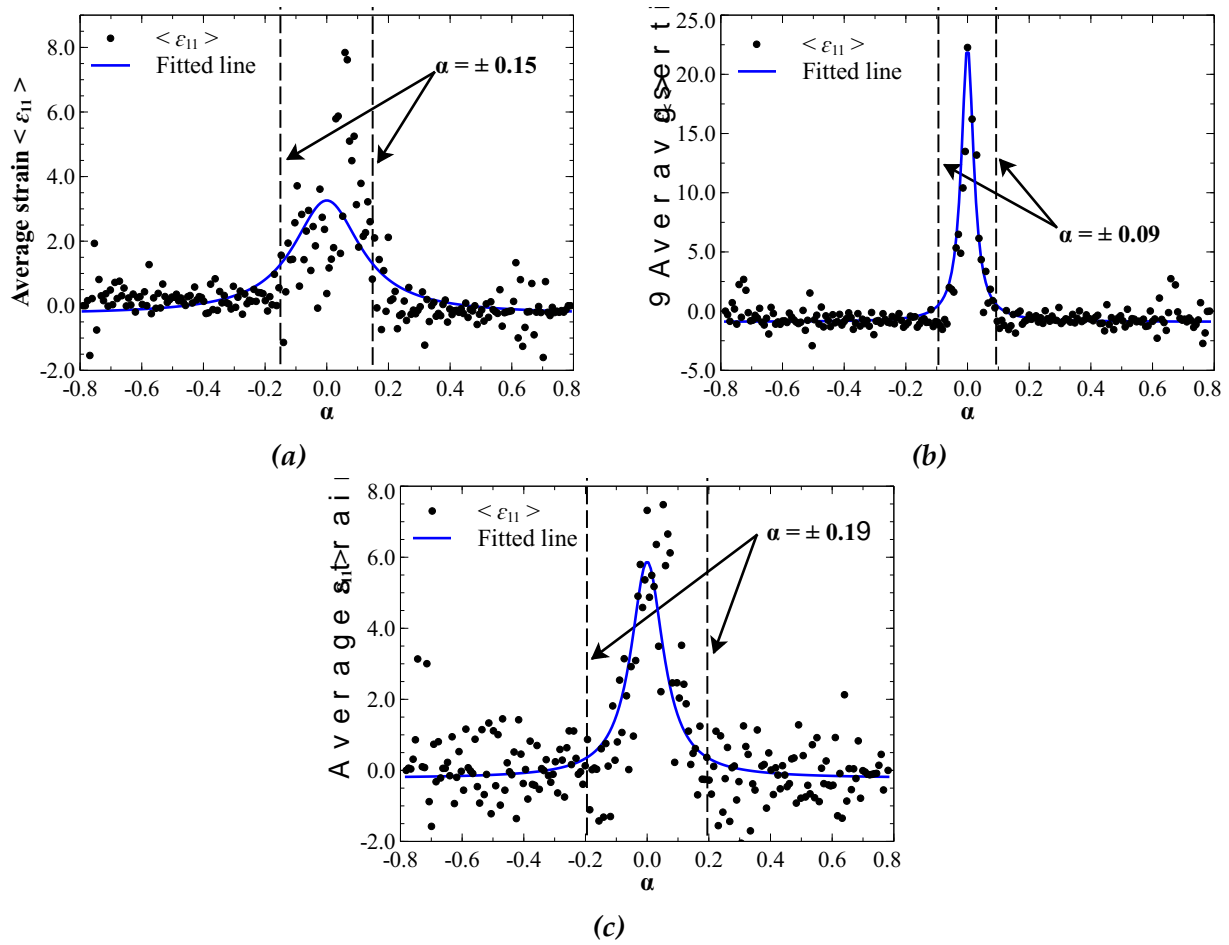


**Figure 3.36:** For specimens S1 (a), S2 (b) and S3 (c), the variation of  $\langle \epsilon_{11} \rangle$  (scattered points) on reference line, which (being parallel with the specimen diagonal) moves along coordinate  $\alpha$ . Scattered point are fitted by the solid line. Vertical dashed lines denote shear band boundaries.

A coordinate  $\alpha$  is set perpendicular to the diagonal of the specimen. To ascertain the shear band width  $2\delta$ , a reference line is drawn parallel to specimen diagonal and moves along coordinate  $\alpha$ . The evolutions of the average  $\epsilon_{11}$ ,  $\langle \epsilon_{11} \rangle$ , around this reference line are then plotted with respect to  $\alpha$  (see Figure 3.36) and fitted by an unimodal function,

$$f(x) = \frac{a}{b\pi \cdot (1.0 + (\frac{x}{b})^2)} - c. \tag{3.16}$$

Evolutions of  $\langle \epsilon_{11} \rangle$  on the axis  $\alpha$  display a prominent unimodal feature. Strain rises dramatically in the center range and oscillates near 0.0 on either side, as the center range refers to the shear band section. Furthermore, when the shear band domain undergoes a loading process with a large positive (compressive) strain, the remaining

area is rebounding as the strain is negative on average. Nevertheless, the deformation in the outside shear band area is quasi-rigid, major deformation takes place inside the shear band. Shear band boundaries are approximately determined at the place where  $\langle \varepsilon_{11} \rangle$  starts to jump. It is shown that the specimen S2 conceives the most concentrated shear band ( $\delta = 0.09$ , see Figure 3.34b and Figure 3.36b) and the highest localized strain, giving rise to the sharpest stress softening amongst specimens (shown in Figure 3.33a). On the contrary, S3 shapes a somewhat spreaded form with  $\delta = 0.19$  (Figure 3.34c and Figure 3.36c). The shear band width in S1 is estimated at  $\delta = 0.15$  (Figure 3.34a and Figure 3.36a).

The failure mode and shear band width for localized specimens have been determined; three specimens encountering localized failure (S1, S2 and S3) and one with diffuse mode (S4) are presented. As mentioned in the introduction, when material develops a non-homogeneous strain field, more attention should be payed on the failure area instead of the global area. The remaining part of this section aims to investigate the evolution of meso-structure inside these failure areas, i.e. the shear band area in localized failure specimens and the global area in the diffuse failure specimen.

### 3.5.3 Critical state void ratio $e$

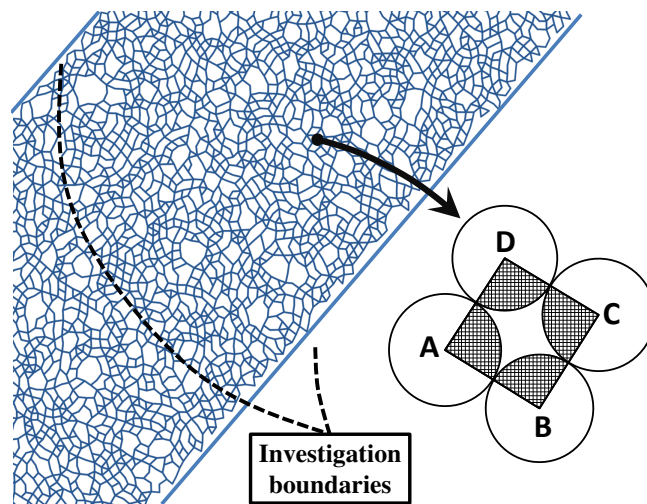


*Figure 3.37: Meso-loops inside prescribed boundaries (upper-left) and the illustration of the total area (ABCD) and the solid area (shaded) of one quadrilateral meso-loop (lower-right).*

Before entering the meso-structure observation, void ratios inside the shear band  $e^*$  in specimens  $S1$ ,  $S2$  and  $S3$  are tracked along the loading path and compared with global void ratio  $e$  of each and  $S4$ . Here and after the asterisk symbol takes the meaning of the shear band domain.  $e$  is calculated on the basis of the meso-loop, given by  $e = (A_t - A_s)/A_s$ ,  $A_t$  and  $A_s$  representatively denote total and solid area. As shown in Figure 3.37, as soon as the investigation area is defined by boundaries (shear band boundaries or specimen boundaries), meso-loops with vertices outside the boundaries are excluded. Then  $A_t$  is equal to the sum of all loop areas, and  $A_s$  is the total enclosed solid area by all loops. Figure 3.37 gives an example of the contribution from a quadrilateral loop.  $A_t$  is the interior area of  $ABCD$ , each of these 4 points is the center of one component particle enclosing this loop. Correspondingly,  $A_s$  is the shadowed area, composed of four fans shaped from the particle center to its two contact points.

As already depicted in subsection 3.5.1, large differences exist amongst critical void ratios of specimens. In Figure 3.38,  $S1$ ,  $S2$  and  $S3$  present significantly lower final  $e$  than the loosest specimen  $S4$  which corresponds to a diffuse failure. However, when looking at the situation inside the shear band, we see that the results are in agreement with the critical state theory.  $e^*$  of all  $S1$ ,  $S2$  and  $S3$  diverges apart from global void ratios  $e$  exactly at the stress peaks, from when the strain localization starts to accelerate (labeled by vertical dashed line in Figure 3.38). Larger dilatancy takes place in the shear band area than in the total area and in the outside shear band area.  $e^*$  then gradually meets  $e$  of  $S4$  during the stress softening period and oscillates around it in the critical state. The convergence of  $e$  in the critical state for all specimens is obedient to the assertion of the critical state mechanics, as an absolute void ratio can be reached in large strain independently from material initial state. However, our results suggest that in localized failure mode, this critical state void ratio is valid only in strain localization domain. Desrues et al. (1996) performed a parallel experiment, in which shear band porosity is investigated by means of X-ray computed tomography (CT) and compared with the porosity in loose samples (Bornert et al., 2010). The material porosity inside the shear band was found approaching a same value in specimens of different initial porosities. Moreover, this value also matched the steady (final) porosity of the loose specimen, in which no clear strain localization was observed. This result supports our research. The critical state  $e$  is then validated both in localized and diffuse failure modes, disregarding the heterogeneity of the material. However, two questions arise from this: what is the underlying physical meaning of the critical state void ratio, and is there any featured structure in smaller scales as the basis of this featured void ratio? This will be investigated in subsection 3.5.4.

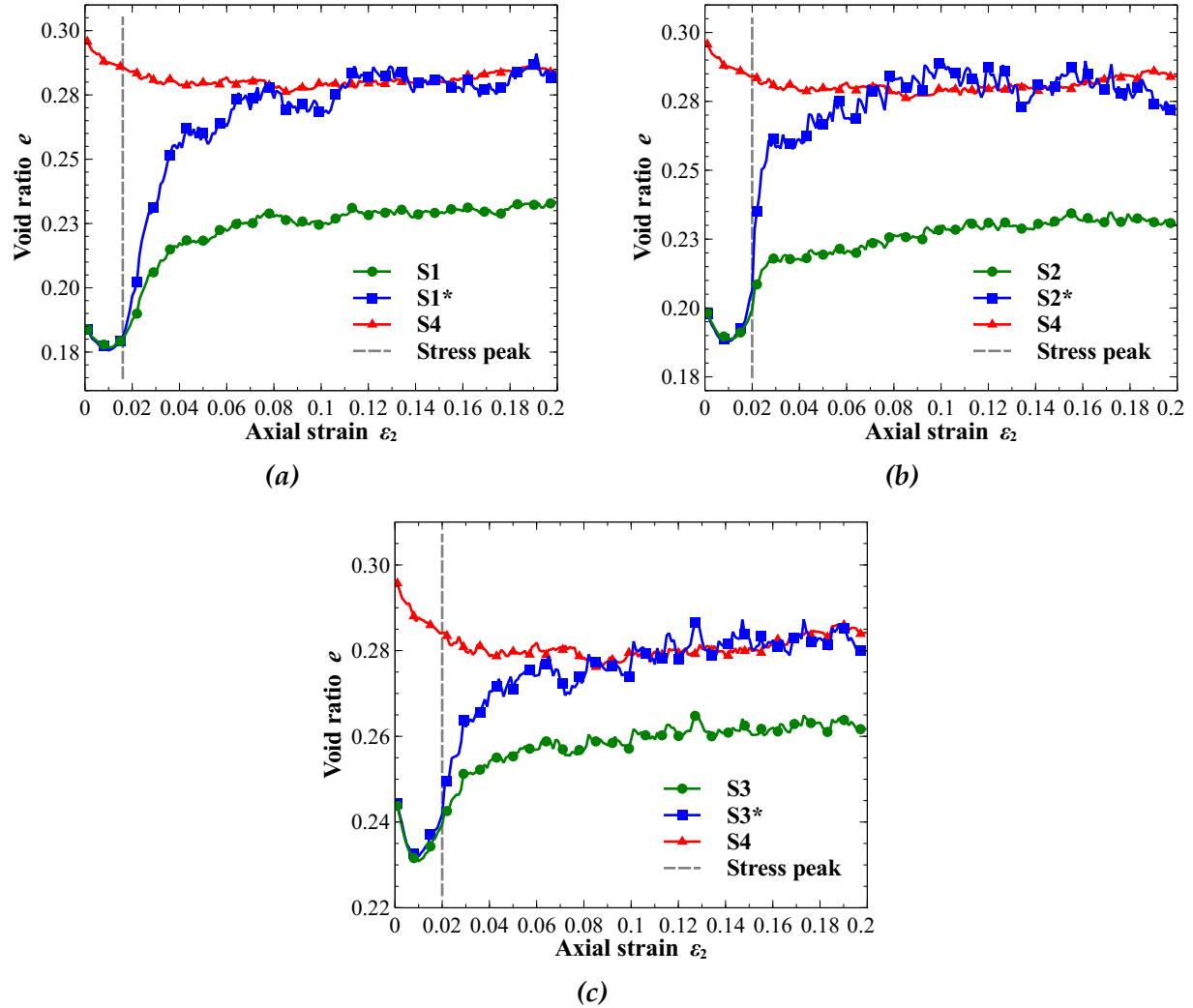


*Figure 3.38: With respect to axial strain  $\varepsilon_2$ , evolution of global void ratio  $e$  and void ratio inside shear band  $e^*$  for specimens S1 (a), S2 (b) and S3 (c), comparing with evolution of  $e$  in specimen S4.*

### 3.5.4 Meso-structure signature of the critical state

In the meso-scale, force-chains and meso-loops co-exist as two kinds of basic structure, conducting the mechanical behavior of the granular material. In attempting to find a characteristic meso-structure in the critical state, quantitative analyses are then carried out in the meso-scale.

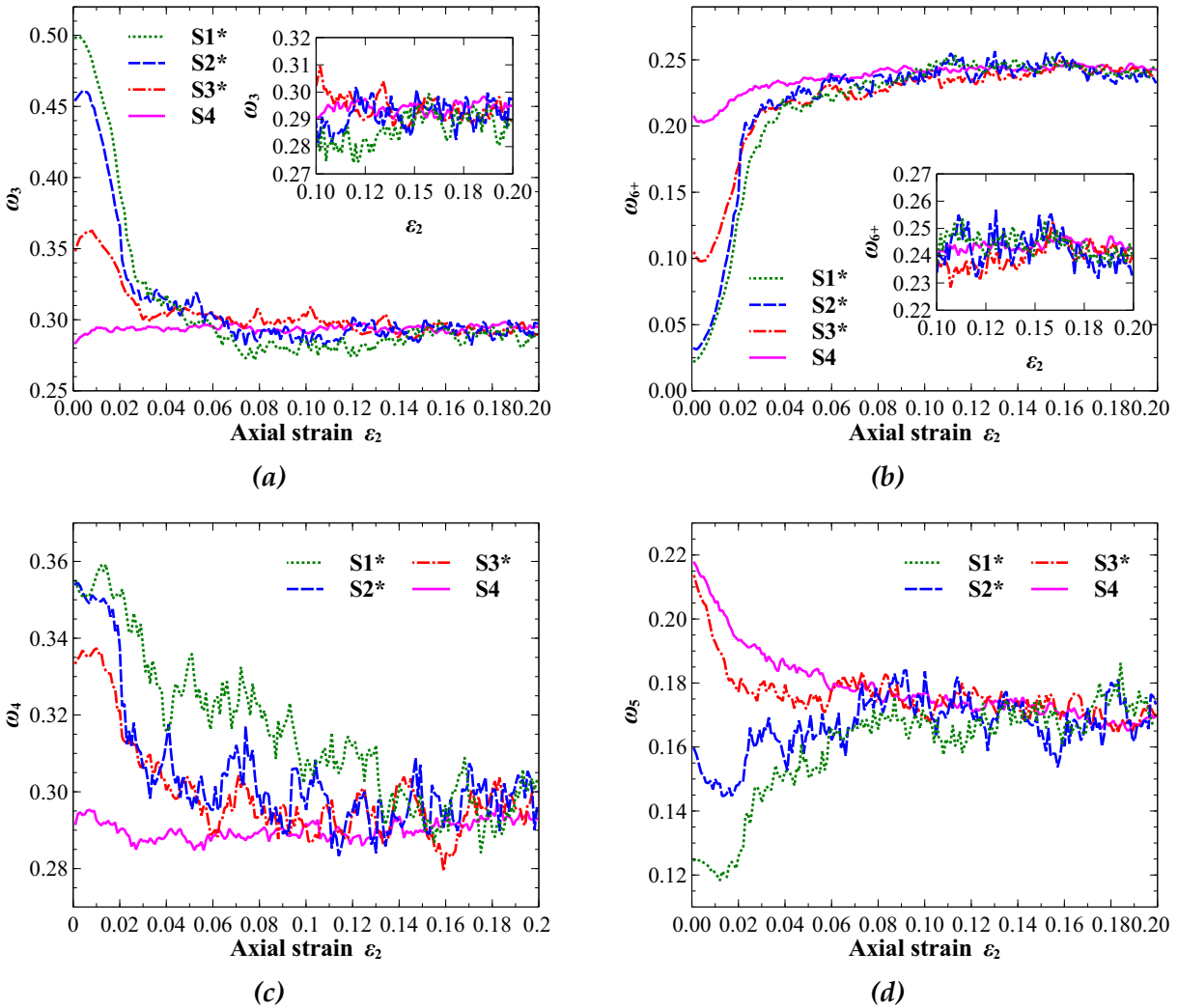


Figure 3.39: With respect to axial strain  $\epsilon_2$ , evolutions of meso-loop ratios  $\omega_3$  (a),  $\omega_{6+}$  (b),  $\omega_4$  (c) and  $\omega_5$  (d) in area S1\*, S2\*, S3\* and S4.

### 3.5.4.1 Meso-loops characteristics

With the same consideration as what we have already shown in the critical state void ratio investigation in subsection 3.5.3, shear band area, instead of whole specimen area, should be the interest area, where main shear deformation actually takes place. Then the meso-structure analysis turns to focus only on the inside failure area. Evolutions of  $\omega_i$  ( $i = 3, 4, 5, 6+$ ) inside the shear band of specimens S1, S2 and S3 (labeled as S1\*, S2\* and S3\*) are tracked along biaxial test and compared with  $\omega_i$  in S4. They are then illustrated in terms of axial strain  $\epsilon_2$  in Figure 3.39.

In  $S1^*$ ,  $S2^*$  and  $S3^*$ , both  $\omega_3$  and  $\omega_{6+}$  unambiguously converge around similar values to those in  $S4$ . This can be also observed from the evolution of  $\omega_4$  and  $\omega_5$ : all specimens evolve to identical final values, as shown in Figure 3.39c and 3.39d. Significant convergences of  $\omega$  in all categories of meso-loop are observed in all specimens, in the failure area rather than in the whole specimen area. Here, the failure area means the shear band area in the specimen of localized failure mode, and the whole area in specimen of diffuse failure mode. This convergence indicates the existence of a common critical state topology on the meso-scale.

An opposite behavior is observed between  $\omega_3$  and  $\omega_{6+}$  in the phase preceding the critical state. For the first three specimens  $S1^*$ ,  $S2^*$  and  $S3^*$ ,  $\omega_3$  shows exponential decrease before their stress peaks. Simultaneously,  $\omega_{6+}$  varies in a sophisticatedly reversed pattern. Both  $\omega_3$  and  $\omega_{6+}$  of  $S1^*$ ,  $S2^*$  and  $S3^*$  generally transit their slopes at the stress peaks, and approach steady values in post-peak phases. Considering that  $\omega_4$  and  $\omega_5$  do not dramatically change in all tests, shear band areas  $S1^*$ ,  $S2^*$  and  $S3^*$  definitively experience strong conversions from  $L_3$  to  $L_{6+}$  before stress peaks, even in the phases we classically consider to be elastic. This points out the fact that bulk dilatancy cumulates potentially before the stress peak, as the big meso-loops are consistently increasing their population. The wording “potentially” means that there may be not a definitively ongoing dilatancy, but rather a dilating trend suggested by the meso-structure. The reason why the material may not dilate immediately following the meso-structure evolution, is because the dilating effect may be covered by the effect given by inter-particle penetration, which also contributes to the bulk variation of the material and normally tends to lead to a contractancy. To this extent, the dilatancy is prepared far before the stress peak, and accelerates until the stress peak (Zhu et al.).

The meso-structure fabric is another aspect in close relation with the material mechanical behavior. In this section, the meso-structure fabric is quantified by a loop tensor  $\underline{H}_l$ , given in similar form as fabric tensor,

$$H_{ij}^l = \frac{1}{2} \sum_{c=1}^{N_c} n_i^c r_j^c, \quad (3.17)$$

where  $l$  is the ID of one meso-loop,  $c$  is the contact in the meso-loop,  $N_c$  is the number of contacts in the meso-loop,  $r$  and  $n$  are respectively the original and the normalized contact branch,  $n = r / |r|$ , and subscripts  $i, j$  denote the  $i$ th and the  $j$ th components of contact branch. The coefficient 0.5 is attributed to the fact that each contact is shared by two meso-loops. For a given meso-loop collection selected by boundaries, as shown in

Figure 3.37,  $\underline{H}^l$  over all meso-loops are summed up to obtain a total meso-loop tensor  $\underline{H}$ . In essence,  $\underline{H}$  is exactly the fabric tensor, as all interior contacts in the considered area have been completely taken into account. The normalized deviator of  $\underline{H}$ ,  $D_H$ , is equal to  $(H_1 - H_2)/I_H$ , as  $I_H$  is the spherical part of  $\underline{H}$ , expressed as  $I_H = H_1 + H_2$ , where  $H_1$  and  $H_2$  are respectively major and minor eigenvalues of  $\underline{H}$ .

In all specimens, evolutions of  $D_H$  and  $I_H$  in both whole specimen and failure area are displayed as function of axial strain  $\varepsilon_2$  in Figure 3.40. As shown in Figure 3.40a and Figure 3.40c, both  $D_H$  and  $I_H$  in the failure area of specimens (S1\*, S2\*, S3\* and S4) converge to a final value. On the contrary,  $D_H$  and  $I_H$  in S1, S2, S3 and S4 stabilize into different values at the end of the test. As long as material forms its internal self-organization, accounting the material as a whole is no longer valid. This means that the failure area, instead of the whole specimen area, of four tested specimens falls on one unified fabric in the critical state. In other words, in S1, S2 and S3, values of  $D_H$  in the shear band area evolve around the value  $D_H = 0.10$  (horizontal dashed line in Figure 3.40a) in the critical state. However, values of  $D_H$  in the whole specimen state at the level much less than the line  $D_H = 0.10$  (horizontal dashed line in Figure 3.40b). This means that the fabric deviator in the whole specimen is always less than that in the shear band area. A higher anisotropy in the fabric of the shear area gives the counter-evidence against the isotropic flow assumption, which hypothesizes the material isotropy under the shear deformation. This supports what Oda (1972a,b,c) has stated: the shear deformation leads to the structure anisotropy of the granular material.

Departing from various initial states, fabrics converge in the critical state. This shows a remarkable agreement with the result obtained from the investigation of meso-loop categories proportion. It is concluded that in the failure area of granular materials, there exists a unified critical state meso-structure with identical morphological characteristics. This critical state meso-structure does not exist in the whole material area, but inside the failure area, where mesoscopic geometry gradually converges with test processing. This convergence is significant, because it makes critical state mechanical properties to be of initial state independence. A convergent meso-structure from different initial states sufficiently ensures the void ratio, deviatoric and mean effective stress to be independent from initial state. On the other hand, this featured fabric can persist (or survive) in a given loading path, after other possible structural patterns have disappeared. It gives rise to a constant stress response and void ratio. Consequently, two fundamental properties of the critical state - initial state independence, and constant stress and volumetric response - can be simultaneously interpreted as deriving from one particular meso-structure. This and only this can persist from a certain loading path. In other words, the critical state

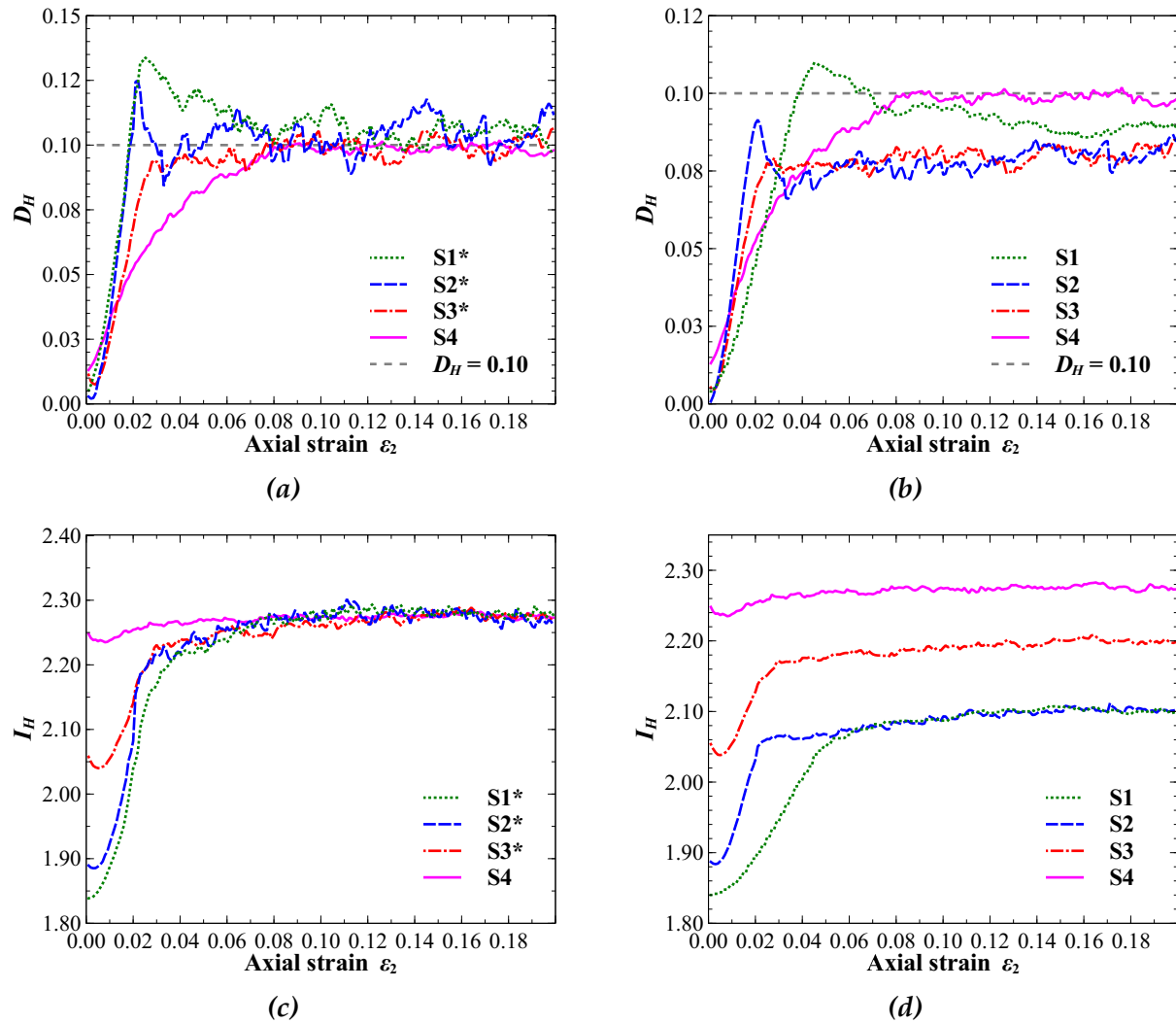


**Figure 3.40:** Evolution of  $D_H$  as function of  $\epsilon_2$  in analyzing area  $S1^*$ ,  $S2^*$ ,  $S3^*$  and  $S4$  (a);  $S1$ ,  $S2$ ,  $S3$  and  $S4$  (b). Evolution of  $I_H$  as function of  $\epsilon_2$  in analyzing area  $S1^*$ ,  $S2^*$ ,  $S3^*$  and  $S4$  (c);  $S1$ ,  $S2$ ,  $S3$  and  $S4$  (d).

meso-structure is the basis of the macroscopic critical state mechanical behavior of the granular material. Further research should be devoted to investigate why only one particular meso-structure can permanently exist under one given loading path. This will answer two fundamental questions: why a granular system can evolve towards a critical state? why mechanical properties in a critical state only depend on the loading path rather than on the initial state?

### 3.5.4.2 Force-chain characteristics

The force transmission is highly inhomogeneous in the granular material. Those major transmission tunnels then construct another kind of meso-structure, i.e. the force-chain, which directly takes charge of the stress response of the material. The material constitutive relation is sensitively related to the evolution and the distribution of force-chains. A massive buckling of force-chains probably leads to the stress peak and the volumetric dilatancy. Consequently, the topology and the duration of the force-chain system primarily decide the mechanical property of the granular material. In this section, attempts are made to give both qualitative and quantitative descriptions on force-chain characteristics in the critical state.

#### Force-chain distribution

Force-chain distribution and buckling events of  $S1$ ,  $S2$ ,  $S3$  and  $S4$  plotted in Figure 3.41 at the strain state of  $\varepsilon_2 = 0.150$ , when the critical state is assumed to be already reached. Buckling events in  $S1$ ,  $S2$  and  $S3$  substantially arise in the shear band area.  $S2$  displays the most concentrated buckling band amongst specimens, while the buckling in  $S4$  occurs pervasively at places without any organization among each other, presenting a chaotic pattern. These are entirely concurrent with the relative displacement field in Figure 3.34, which indicates that displacement localizes into shear band in  $S1$ ,  $S2$  and  $S3$  but diffuses in  $S4$ . When roughly viewing on the force-chain texture of all specimens, we find that inside shear band area or diffuse failure area, force-chains tend to be loosely distributed and less straight ranged towards the major compressing direction than outside shear band area. In a compact force-chain texture, force-chains are well supported by their neighbors, significantly reducing the possibility of buckling, i.e. the health of force-chains. Even if some of them buckle, the material can build new compensatory branches with ease, i.e. the robustness of the force-chain. In a loose force-chain texture, however, force-chains can hardly find neighboring support, so that they are probable of buckling during the loading path. To this extent, the health and the robustness of the force-chain texture are extremely crucial and directly related to the ability of a material to increase its strength. In this section, we do not directly give a degree of health or robustness of the force-chain texture. Alternatively, we survey the age composition over the force-chain system. An age survey on force-chain is suggestive of the demographical age survey, to give the percentages (or the density distribution) of the force-chain in various age ranges, at one stress-strain state of the test. A healthy, robust force-chain environment should be

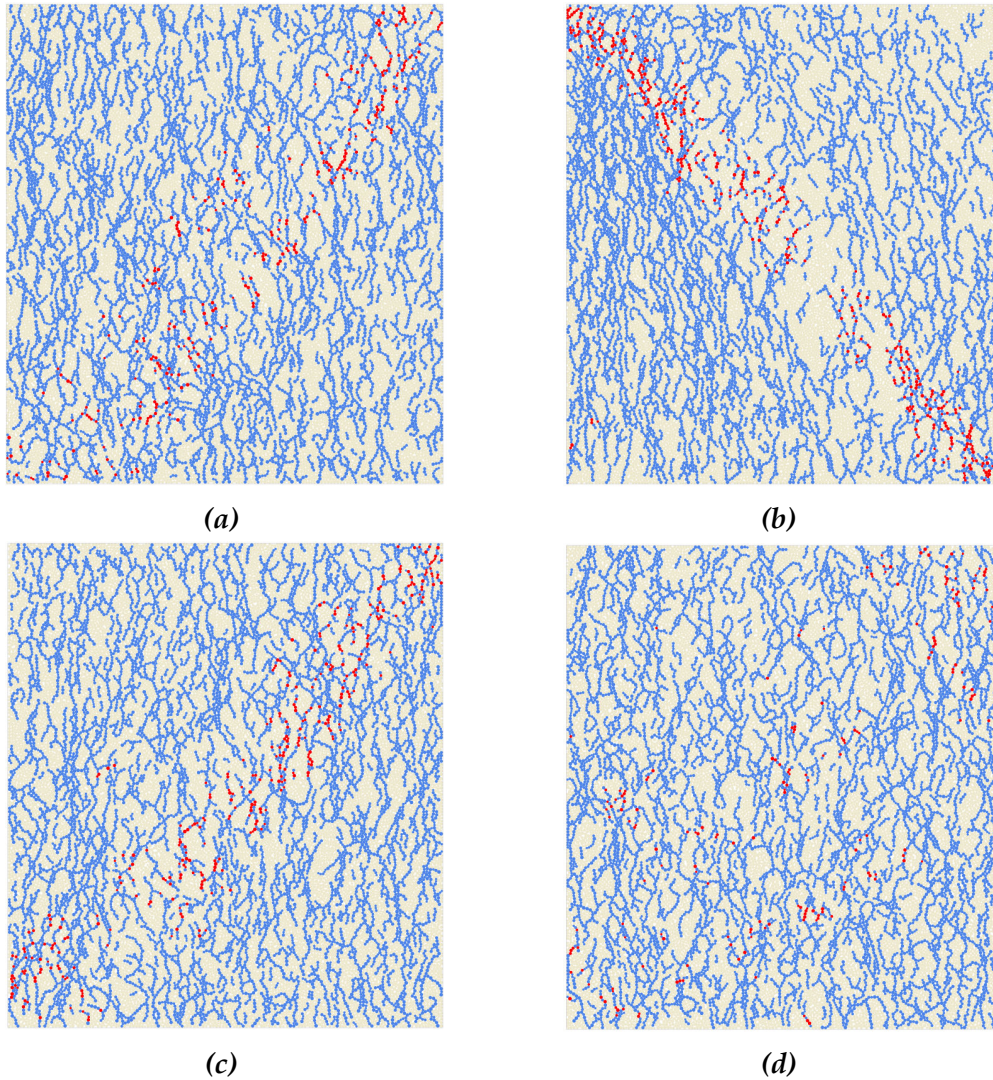


*Figure 3.41: Force-chain distribution (in light blue) and buckling particles (in red) for specimens (a) S1, (b) S2, (c) S3 and (d) S4*

composed of mainly old, or at least middle-aged, force-chains with a small proportion of young force-chains. If a texture is mainly constructed by young force-chains, and hardly builds any long-lasting force-chain, it can be considered as weak and fragile. This will be investigated in the following.

#### **Force-chain age composition in critical state**

The age survey is not directly on force-chains but on 3-particle sets, the force-chain subset, consisting of three particles in force-chain linked head-to-end (already introduced in section 3.4). At the surveying time step, the age of one 3-particle set  $l$  is defined by

the number of time step it unremittingly goes through.  $l$  thus depends on the chosen length of the time step. A normalized age  $l_r$  is therefore introduced in a dimensionless form to diminish this scale dependence, such that  $l_r$  is equal to  $l/l_t$ ,  $l_t$  is the number of experienced time steps of the test to the surveying moment.  $l_r$  belongs to the range  $[0, 1]$ .  $l_r < 0.1$  indicates 3-particle sets (force-chains) created near the end of test, while  $l_r > 0.9$  corresponds to those created near the start of the test. In biaxial test, the situation becomes easier, as a fixed axial strain rate  $\dot{\varepsilon}_2$  ensures  $\varepsilon_2$  to be proportional to the test time as well as the number of time steps, Thus we have

$$l_r = \frac{\varepsilon_2^t - \varepsilon_2^{born}}{\varepsilon_2^t}, \quad (3.18)$$

where  $\varepsilon_2^t$  is the value of the axial strain at surveying moment,  $\varepsilon_2^{born}$  is the value of the axial strain at birth of the considering 3-particle set. Practically, we analyze the age of all 3-particle sets at the end of test  $\varepsilon = 0.200$ . Choosing this time point rather than somewhere in the middle of test is in order to grant force-chains a sufficient time to evolve (to be born and to die) towards a realistic age distribution in the critical state. Then the age density distribution of all 3-particle sets is plotted in histograms, shown in Figure 3.42, in which the horizontal axis is the age  $l_r$  and the vertical axis is the density (the percentage divided by the length of the age range) of the 3-particle sets in a certain range of age  $l_r$ , denoted by  $p$ .

In histograms of Figure 3.42, we distinguish the contributions, given by inside shear band area (denoted by asterisk superscript,  $p^*$ ) and by outside shear band area (denoted by superscript “osb”,  $p^{osb}$ ), to the gross value of  $p$ . We herein briefly mention the way of calculating  $p$ . At the surveying moment, the percentage of 3-particle sets with  $l_r$  dropping into age interval  $[x, x + \Delta x)$  ( $x \in [0, 1)$ ) and position simultaneously being inside shear band area, named by  $P^*$  (or outside shear band, named by  $P^{osb}$ ), can be calculated as:

$$\begin{aligned} P^*(x \leq l_r < x + \Delta x) &= \frac{N^*(x \leq l_r < x + \Delta x)}{N(0 \leq l_r \leq 1)}, \\ P^{osb}(x \leq l_r < x + \Delta x) &= \frac{N^{osb}(x \leq l_r < x + \Delta x)}{N(0 \leq l_r \leq 1)}, \end{aligned} \quad (3.19)$$

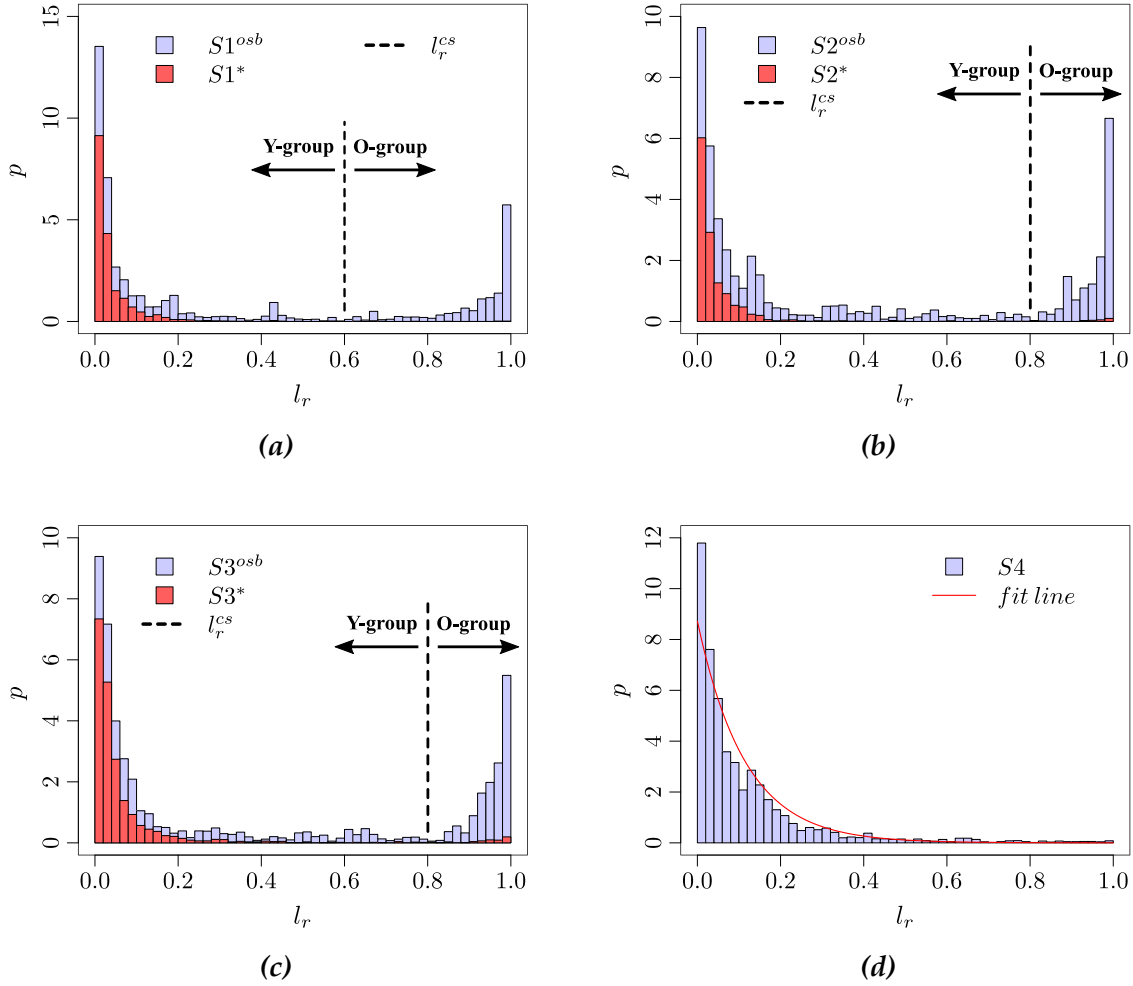


**Figure 3.42:** Age density distribution of all 3-particle sets in specimens (a) S1, (b) S2, (c) S3 and (d) S4 at strain state  $\varepsilon = 0.200$ . Distribution in S4 is exponentially fitted by a continuous line. The value of  $p$  is divided into two parts: contributions given by inside shear band area (denoted by asterisk superscript,  $p^*$ ) and by outside shear band area (denoted by superscript “osb”,  $p^{osb}$ ).

where  $N^*(condition)$ ,  $N^{osb}(condition)$  and  $N(condition)$  respectively denote the number of 3-particle set fulfilling the condition, in area of inside shear band, outside shear band and whole specimen.  $N(0 \leq l_r \leq 1)$  is equal to the total number of 3-particle sets in the specimen. The density  $p^*(x)$  is then given by the percentage  $P^*(x, \Delta x)$  divided by the range length  $\Delta x$ , as follow

$$p^*(x) = \frac{P^*(x \leq l_r < x + \Delta x)}{\Delta x}. \quad (3.20)$$

$p^{osb}(x)$  is given likewise. Therefore, summing up  $p^*(x)$  and  $p^{osb}(x)$  gives the density of the whole specimen  $p(x)$ , making sure that  $\int_0^1 p(x)dx = \int_0^1 (p^*(x) + p^{osb}(x))dx = 1$ . To reiterate, columns biasing  $l_r = 0.0$  include relatively newly created 3-particle sets, and those biasing  $l_r = 1.0$  include relatively old ones. The word “relatively” indicates that the degree of youngness or oldness is only discussed in comparison with the time span of the test.

Similar shapes of  $p$  in S1, S2 and S3 are found in Figure 3.42a, 3.42b and 3.42c, presenting concave outlines with two peaks on both sides, which exponentially drop to the center basin. Distributions of  $p$  in specimens with localized failure reveal that the force-chain system lacks middle age components, when consisting of either young or old elements. Here we separate the  $l_r$  axis into two parts, a young age group of 3-particle sets formed in critical state, named of “Y-group”, and an old age group of 3-particle sets formed before critical state phase, named of “O-group”. Start points of critical state  $\varepsilon_2^{cs}$  are estimated at the reaching of the steady stress and the volumetric strain, as  $\varepsilon_2^{cs} = 0.080$  in S1,  $\varepsilon_2^{cs} = 0.040$  in S2 and  $\varepsilon_2^{cs} = 0.040$  in S3. They are translated to  $l_r^{cs}$  by Eq. 3.18 and labeled by dashed line in Figure 3.42.

In O-group,  $p$  of all specimens in localized failure mode presents similar trend to exponentially grow as  $l_r$  increases. Firstly, there are a large number of O-group force-chains, which preserve to the end of test, and a vast majority of them belongs to outside shear band area. That is because during the formation of the shear band, with the strain concentrating into part of specimen, other areas are allowed to have a quasi-elastic unloading. With nothing but this unloading, force-chains outside shear band can be long-standing. However, it is still notable that force-chains built in early steps of the compression show pronounced vitality in granular material. The longevity tends to decrease for later created force-chains. It gives a significant indication that in drained biaxial test, force-chains are continuously losing their durabilities and sustainabilities with the evolutionary fabric on which they locate. In granular material under drained biaxial test, as long as force-chains collapse, the system is incapable to build new force-chains as robust as collapsed ones. This can be corroborated and explained, from another side, by the consistent depopulation of  $L_3$  in S1, S2 and S3 (shown in Figure 3.39a). The system is irreversibly losing its firm and sustainable members. In lack of reliable carriers, force-chains cannot be long-standing. This is where the deficiency of middle age force-chain comes from. Hence, in critical state there are only robust old force-chains, mostly existing outside shear band, and vulnerable young ones.

In Y-group,  $p$  exponentially drops as  $l_r$  increases. In another word, new created force-chains are dying out in a high rate, it is difficult for force-chains created in the critical state to prolong life. When looking at the distribution of  $p^*$  in localized specimens, we find that  $p^*$  occupies major proportion in  $p$  in interval  $l_r = [0.0, 0.2]$  and presents significantly exponential drop with increasing  $l_r$ . This means that the exponentially decreasing distribution of Y-group is therefore largely attributed to the force-chain evolution in the failure area. Most new created force-chains in specimen are located inside shear band and, meanwhile, these young age force-chains die out in high speed. Combining the information from Y-group and O-group, a scene appears that in the critical state, with the strain localization, the material separates into two domains with different force-chain evolution patterns: the inside shear band area with a tremendously changeable fabric, in which there are young and fleeting force-chains; and the outside shear band area with a healthy and robust force-chain system, in which force-chains can be long-standing.

It is noteworthy that the distribution of  $p$  inside shear band highly resembles what we observe in whole specimen of S4, where  $p$  presents exponentially descend without any rise as  $l_r$  varies from 0.0 to 1.0. The only difference is the gentler descending slope of  $p$  in S4 (we will discuss this in the next paragraph). This indicates that in the critical state, there is a common force-chain evolutionary pattern inside failure area, i.e., again, the shear band area of the localized failure mode specimen and whole area of the diffuse failure mode specimen. High birth and death rates of force-chains coexist inside the failure area, making it a special place in granular materials. For one thing, it is unstable, because the system cannot find enough prolonged force-chains to maintain its strength. For another, it is sensitive. As shown by distribution of  $p^*$ , small strain increment can lead to a massive creating and collapsing of force-chains, i.e. the redistribution of force-chain. With this force-chain redistribution, the fabric must follow and change, then the mechanical response of the granular assembly will vary accordingly.

### Age distribution approximation

Basically, the age distribution of force-chains is dependent on the birth number  $A(0)$  and the decaying (dying) rate  $\phi$  of force-chains in each time step, where  $A(n)$  denotes the number of remaining force-chains, which are created  $n$  time steps before ( $n = 0, 1, 2, \dots$ ). In the other words, provided that there are  $A(0)$  newly created force-chains (as a group named  $FC_{t_0}$ ) in a certain time step  $t_0$ , after  $n$  steps, the number of the remaining force-chains in group  $FC_{t_0}$  is  $A(n)$ . Obviously, if  $\phi$  is fixed (it is basically true in critical state),

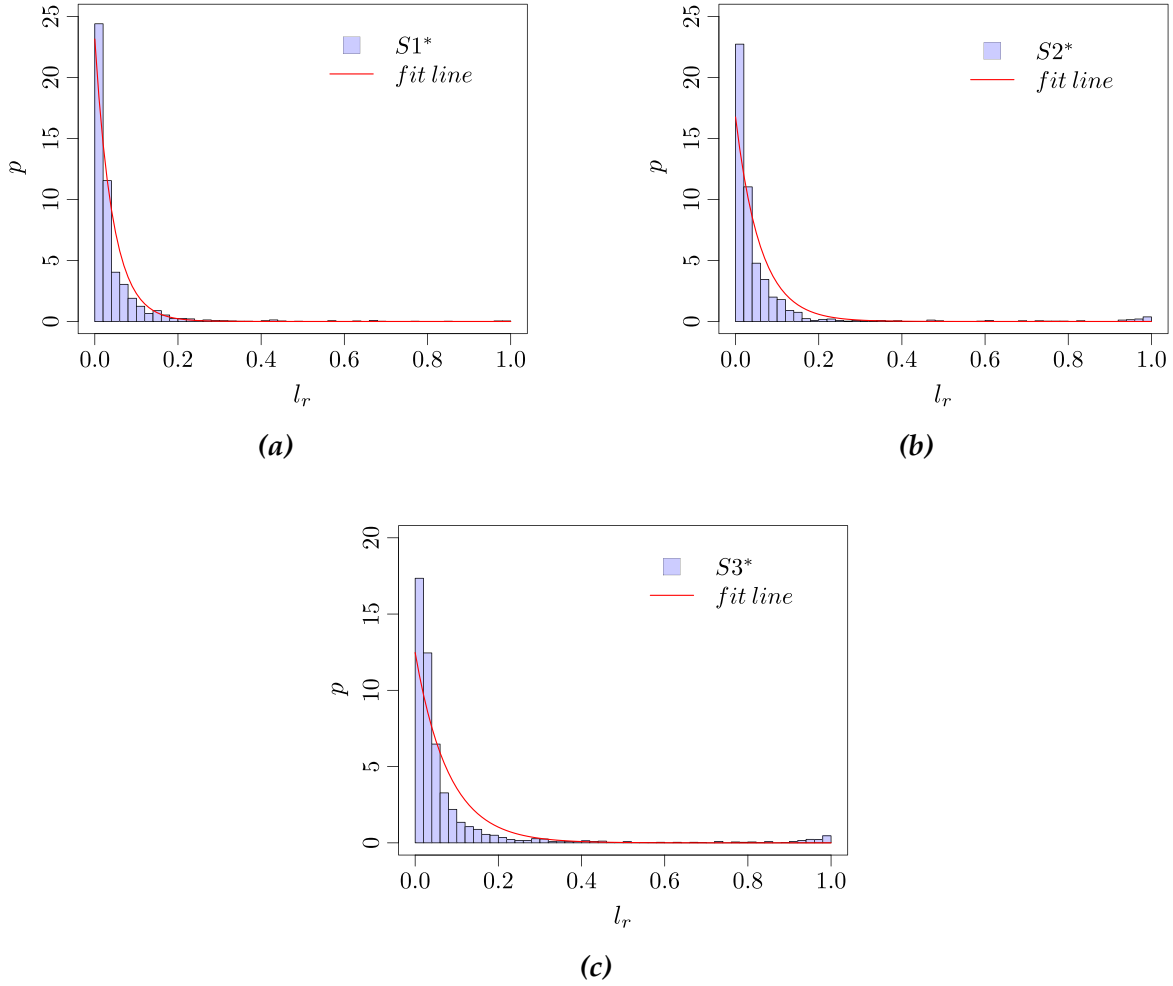


**Figure 3.43:** Age density distributions and their fitted lines of all 3-particle sets in shear band area of specimens (a) S1, (b) S2 and (c) S3 at strain state  $\varepsilon = 0.200$ .

as the time passes step by step, the  $A(n)$  will decay exponentially

$$A(n) = A(0) \cdot (1 - \phi)^n. \quad (3.21)$$

In critical state, the number of new created force-chains  $A(0)$  in every time step is more or less equal. Therefore, at the surveying moment, the approximating percentage of the force-chains created  $n$  time steps before,  $P_a(n)$ , is given by

$$P_a(n) = \frac{A(n)}{\sum_{i=0}^{+\infty} A(i)} = \frac{(1 - \phi)^n}{\sum_{i=0}^{+\infty} (1 - \phi)^i} = \phi(1 - \phi)^n. \quad (3.22)$$

This equation indicates that if  $A(0)$  and  $\phi$  are fixed, at any time step, the force-chain age follows an exponential distribution. Then age distributions of S1, S2, S3 and S4 in  $\varepsilon = 0.200$  are fitted in Figure 3.43 and Figure 3.42d.

In one given time step, the parameter  $\phi$  is approximately equal to  $N_b/N_{3p}$ ,  $N_b$  and  $N_{3p}$  respectively denote in one time step, the number of buckling events and the number of 3-particle set in the failure area. The mean value and standard deviation of  $N_b$  in one time step in critical state ( $0.100 \leq \varepsilon_2 \leq 0.200$ ) are listed in table 3.6. It is shown that the number of force-chain buckling events  $N_b$  generally stays in the same level for all specimens.  $\phi$  therefore is inversely proportional to  $N_{3p}$ . This is the reason why  $\phi$  in S4 is less than that in S1\*, S2\* and S3\*, leading to a gentler decrease of  $p$  for S4.

*Table 3.6: Mean value and standard deviation of buckling events  $N_b$  in critical state*

Specimen	$\langle N_b \rangle$	Std.
S1	327.8	70.6
S2	267.8	70.7
S3	307.6	80.9
S4	308.0	76.6

### 3.5.4.3 Discussion: the homology of localized and diffuse failure modes

The existence of critical state meso-structure provides an insight on the link between localized and diffuse failure modes. Theoretical localized failure criterion was derived by Rice (1976), expressed as the vanishing determinant of acoustic tensor  $n \cdot D \cdot n$ , i.e.

$$\det(\underline{n} \cdot \underset{4}{L} \cdot \underline{n}) = 0, \quad (3.23)$$

where  $n$  is the normal vector of strain localization band and  $\underset{4}{L}$  is the four-order tangential constitutive tensor such that  $d\underline{\underline{\sigma}} = \underset{4}{L} : d\underline{\underline{\varepsilon}}$ . The vanishing second order work  $W_2$ , once proposed by Hill (1958) to signify material instability, was highlighted by Darve et al. (1995a) as a sufficient condition of general diffuse failure, expressed as

$$W_2 = d\underline{\underline{\sigma}} : d\underline{\underline{\varepsilon}} = d\underline{\underline{\varepsilon}} : \underline{\underline{D}} : d\underline{\underline{\varepsilon}} = 0, \quad (3.24)$$

where  $\underline{\underline{D}}$  denotes the second order tangential constitutive tensor.

Later theoretical deduction revealed that the incremental strain inside localized band, which leads to a vanishing of  $\det(\underline{n} \cdot \frac{L}{4} \cdot \underline{n})$ , also ensures the vanishing of  $W_2$ . Localized failure condition then proves to be a sufficient condition of vanishing  $W_2$ . Localized failure also referred to the loss of positiveness of  $\underline{D}$  (Petryk, 1992) in shear band. Consequently, localized failure mode belongs to a subset of general diffuse failure and emerges inside the bifurcation domain defined by the second order work criterion (equivalent to the loss of the positiveness of  $\underline{D}$ ) (Nicot and Darve, 2011a; Wan et al., 2013). Even though the affiliating relation has been theoretically proven, experimental background and mechanism behind this relation still need to be clarified. Convergent void ratio in critical state (shown in subsection 3.5.3) gives an experimental glimpse on the intrinsic connection between these two kinds of failure. The existence of a critical state meso-structure definitely points out that localized and diffuse failure modes derive from a same original texture. This is merely one basic structure appearing on different scales. The localized failure is essentially one particular diffuse failure, what counts only lies in the scale we choose. In the material where localized failure occurs, if the observing scale is set to be smaller than the shear band width, a diffuse failure is observed.

Another notable point is that even in a diffuse failure area, we can also observe localized failure, such as what we can observe in Figure 3.34d, where a blurry and temporary localized band system fabricates a whole diffuse failure space. Given that a same micro-scale topology and force transmission pattern have been captured coincidentally inside shear band and in the whole diffuse failure area, it is reasonable to expect that inside shear band, there is also a systematic localization, which exists in another spatial and temporal scale. Here the spatial scale measures the average range of the localization, which, for example, can be quantified by the average shear band widths  $2\delta$  over the mean particles radius  $D_{50}$ ; the temporal scale averagely measures the time span of the localization process. It is recommended to investigate this scale-dependence (spatially and temporally) of the localization. If it is true, when we continuously reduce our observing scope from extremely large scale, two failure modes will alternatively appear. The only limitation comes from the length of basic grain which constructs the material. In another word, this is expected to be the "fractal" feature of failure in granular materials.

## 3.6 Conclusion

A meso-scale is introduced in this chapter, being different from the micro-scale, i.e. the single contact scale, and the macro-scale, i.e. the scale of *REV*. Two featured structures in the meso-scale, the force-chain and the meso-loop, are mentioned, giving rise to a combining notion - meso-structure. The significance of this meso-structure is highlighted in this chapter. Based on the numerical biaxial test using *DEM*, interests are held on three aspects of granular materials: the evolution of the meso-loops; the interaction between force-chains and meso-loops; the critical state meso-structure in different failure modes. Main results are concluded in what follows.

### 3.6.1 Meso-loop evolution during biaxial loading

A series of drained biaxial tests were carried out based on a discrete element method, to investigate the meso-loop evolution of the granular material in different initial states.

When the evolution of the proportions of meso loop categories ( $\omega_3, \omega_4, \omega_5, \omega_{6+}$ ) was plotted, it was found that  $L_3$  and  $L_{6+}$  were the two most active groups in terms of population variation. Their proportions,  $\omega_3$  and  $\omega_{6+}$ , evolve oppositely, showing a highly negative evolutionary correlation. The mutual conversion between  $L_3$  and  $L_{6+}$  can be representative of the fabric evolution on the meso-scale. Furthermore, in dense and intermediate specimens, the conversion between  $L_3$  and  $L_{6+}$  was generally unidirectional before the stress steady state, i.e. from  $L_3$  to  $L_{6+}$ . Considering the different mechanical characteristics of  $L_3$  and  $L_{6+}$ , this unidirectional conversion before the stress steady state significantly changes the macro-scale properties of the material, in terms of both stress and strain performances. On one hand, the material loses its strength, as there was a continuous conversion from firm elements to deformable elements, which underpins the sustainability of the material. On the other hand, the material volume may increase, as a result of the conversion from dense elements to loose elements. To this degree, the meso-loop evolution is the basis of the stress and volumetric behavior of granular specimens. It can be the link between these two fundamental mechanical features. Moreover, it was observed that  $\omega_3$  basically keeps constant in the loose specimen, even though the specimen volume continuously contracts. This indicates that it is difficult to massively build  $L_3$  along the biaxial loading path, a mere (too small) contractancy is insufficient in bringing substantial  $L_3$  into the system.

The total and average areas of different kinds of loop ( $A_i$  and  $\bar{A}_i$  respectively) were also investigated in this section. According to the result of  $\bar{A}_i$  evolution,  $L_{6+}$  is the only kind of loop geometrically sensitive to the external loading. Meanwhile, evolution of  $a_i$  in dense and intermediate specimens shows that only  $L_{6+}$  presents a volume increase during the loading path while the other kinds of loop contract. The significance of  $L_{6+}$  was highlighted;  $L_{6+}$  exerts the strongest influence on global volumetric variation and is the only contributor to the dilatancy of dense and intermediate specimens.

The concept of the meso-loop volumetric variation is introduced, based on the fact that the creation of  $L_{6+}$  and the destruction of  $L_3$  are contributing to the meso-loop dilatancy (*MV-D*); on the contrary, the creation of  $L_3$  and the destruction of  $L_{6+}$  point to the meso-loop contractancy (*MV-C*). However, in contractancy phases of dense and intermediate specimens, the meso-loop evolution was observed not to be consistent with the evolution of the macroscopic volumetric strain. Then the elastic part of the volumetric variation, which derives from particle penetrations, was assumed to be the factor dominating the macroscopic contractancy in dense and medium-density granular assemblies, over the plastic part which derives from the meso-loops rearrangement. This assumption was then supported by the energy analysis and plastic strain investigation of specimens. Following that, we have verified that particle elastic parameters could impose a strong effect on the contractant behavior of dense granular materials.

### 3.6.2 Force-chain interaction with meso-loop along biaxial loading path

In a granular assembly, there are two kinds of grains organization on the meso-scale: the linearly organized column-like grain series, which is highly inhomogeneous and takes in charge the force transmission; and the grain loops, enclosed by contact branches, which originally distribute relatively homogeneously. How the former interacts with the latter is crucial to understand the mechanism of some macroscopic phenomena in the granular material. Departing from the *DEM* simulation of drained biaxial tests, meso-loops are grouped into 4 categories, according to their side numbers. Additionally, the granular assembly is separated into two parts: loops connected to force-chains (*FCL*) and loops far from force-chains (*NFCL*). Then the pattern and the process of force-chains affecting (section 3.4.2) and being affected by (section 3.4.3) meso-loops are analyzed. Main conclusions extracted from the results are depicted as follows.

When the evolution of meso-loops in *FCL* area is compared with that in *NFCL* area, it is found that under the effect of force-chains, the material is structurized into two differently featured phases with distinct meso-structures and densities. The *FCL* area contains a larger proportion of  $L_3$ ,  $L_4$  and a smaller proportion of  $L_{6+}$ ,  $L_5$  than the *NFCL* area does. This trend is especially prominent for  $L_3$  and  $L_{6+}$ . Evidences can also be found that the *FCL* area is observed to constantly take higher void ratio  $e$  than remaining area. From a volumetric change point of view, the *FCL* area has more instinct to extend its volume, i.e. the meso-scale volumetric dilatancy (*MV-D*). Thus, force-chain area can be seen as the main source and the primary contributor to the global dilatancy. The discrepancy in the ability of dilating between force-chain area and outside force-chain area, derives from the fact that the latter, compared with the former, lacks the ability to generate big loops.

Other than the action force-chains have on their surrounding meso-loops, there also exists a retroaction given by meso-loops. The existence of  $L_3$  proves to handicap the movability of force-chains and to improve the stability of them, while  $L_{6+}$  enhances the movability and alters the stability of force-chains. At the end, the life-cycle of force-chains can be displayed as a history of interaction with its confining meso-loops.

Moreover,  $L_{6+}^{FCL}$  is observed to be more anisotropically stressed than others, while  $L_3^{FCL}$  is the most isotropic one. This means that  $L_3^{FCL}$ , on average, tends to transfer more subjected axial force to its lateral sides. This leads to a bulk expansion in those granular assemblies, where  $L_3$  prevails, e.g. the dilatancy in dense specimens. Then the meso-loops follow the bulk expansion to give rise to the transformation from  $L_3^{FCL}$  to  $L_{6+}^{FCL}$ . When force-chains are no longer confined by as many as  $L_3^{FCL}$  such that its stability can be ensured, they will buckle and collapse. Finally, this causes a drop on the material strength. Therefore, two conclusions can be extracted: (1) according to the initial fabrics, the loading path will direct dilatancy or contractancy; (2) the stability of force-chains varies in accordance with the evolution of meso-structures, and the latter follows the global volumetric change.

### 3.6.3 The critical state meso-structure in localized and diffuse failure modes

The critical state fabric of granular materials has been investigated in localized and diffuse failure modes on a mesoscopic viewpoint, on the basis of the DEM simulation results of a series of 2D drained biaxial tests, with specimens in different initial states. Emphasis was placed on finding a convergent meso-structure as the signature of critical state.

When the relative displacement fields are plotted, specimens S1, S2 and S3 present clear diagonal shear bands, or localized failure modes, S4 undergoes a diffuse failure. Through analyzing the strain field, shear band widths of S1, S2 and S3 are determined.

For each specimen of localized failure mode (S1, S2 and S3), the critical state void ratio both in the whole specimen area  $e$  and in the shear band area  $e^*$  are analyzed and compared with  $e$  of S4. In all finally localized specimens,  $e^*$  is found to diverge with  $e$  at the stress peak and converge with  $e$  of S4 at the critical state. This definitively proves that the critical state void ratio is only valid inside the failure area rather than in the whole specimen area, i.e. the shear band domain of the localized failure, and the specimen domain of diffuse failure.

We then attempted to find out if the identical void ratio originates from one common meso-structure. Two kinds of meso-structure are counted: the meso-loop and the force-chain. In 2D granular materials, the contact network tessellates the material area into meso-loops, minimum polygons encompassed by contact branches. Meso-loops are grouped into 4 categories according to their side number,  $L_3$ ,  $L_4$ ,  $L_5$  and  $L_{6+}$ . Due to the inhomogeneous force transmission in the granular assembly, the quasi-linear columns consisting of particles transmitting a larger force than average are highlighted to form the force-chain system. The element of this system is 3-particle set, involving 3 force-chain particles connecting each other head to end.

Proportions of meso-loop categories  $\omega_i$  ( $i = 3, 4, 5, 6+$ ) have been investigated in the failure area, i.e. the shear band area of localized specimens  $S1^*$ ,  $S2^*$  and  $S3^*$  and the specimen area S4. For all 4 categories, without any exception,  $\omega_i$  in  $S1^*$ ,  $S2^*$ ,  $S3^*$  and S4 meets at the critical state. This convergence indicates the existence of a single critical state topology on the meso-scale. As hypothesized, it only appears in the failure area.  $\omega_3$  and  $\omega_{6+}$  present opposite behaviors before the stress peak. The shear band areas  $S1^*$ ,

$S2^*$  and  $S3^*$  experience strong conversion from  $L3$  to  $L_{6+}$  before the stress peaks, even in the phases we classically consider as elastic. This conversion points to the fact that bulk dilatancy cumulates potentially before stress peak, as big meso-loops are consistently increasing its population.

To find more evidence on the existence of identical critical state fabric in the meso-scale, the loop tensor  $\underline{H}$  is analyzed in the failure area of specimens.  $\underline{H}$  is found to have the similar deviatoric part  $D_H$  and spherical part  $I_H$  in the critical state in areas  $S1^*$ ,  $S2^*$ ,  $S3^*$  and  $S4$ . This proves again that the failure area, instead of the whole specimen area, of four tested specimens falls on one unified fabric in the critical state.

We plotted the force-chain texture and buckling 3-particle sets. Buckling events are found to largely localize in the shear band area,  $S1^*$ ,  $S2^*$  and  $S3^*$ . As with a high buckling rate, the force-chains inside the shear band tend to be loosely distributed and less straight ranged towards the major compressing direction than the outside shear band area. Moreover, this pattern resembles the force-chain distribution in  $S4$ . In roughly viewing the force-chain distribution in the critical state, we discern a similar force transmission pattern of the critical state in the failure area.

Then we investigated the force-chain age composition in the critical state. At the end of the test, the age distribution  $p$  of all 3-particle sets in the considered domain is plotted. Here, the age of a 3-particle set is the number of time steps it lives through. Force-chains built in early steps of the test show prominent vitality in granular material. In drained biaxial tests, force-chains are continuously losing their durabilities and sustainabilities with the evolutionary fabric on which they are located.

Otherwise, we find that most newly created force-chains in specimens are located inside the shear band, but these young age force-chains die out quickly. It is concluded that while the material evolves into the critical state, there are only old, robust force-chains, mainly located outside shear band, and young, fleeting force-chains, mainly located inside shear band. Meanwhile, the force-chain evolution pattern inside shear band highly resembles the force-chain behavior in  $S4$ . High birth and death rates of force-chains coexist inside the failure area, making it an unstable and sensitive place in granular materials. This is the common force-chain behavior for both localized and diffuse failure, which can be approximated by an exponential decay law.

The existence of critical state meso-structure supports that localized and diffuse failure modes derive from the same original structure. The localized failure is essentially one particular diffuse failure, what counts only lies in the scale we choose.

# Chapter 4

## A Multi-scale Approach Constitutive Model

A wide spectrum of complex constitutive characteristics has been observed and recognized in the granular materials, such as a highly incrementally non-linear constitutive behavior (Darve, 1990; Darve et al., 1995b), the existence of the non-associate flow rule, the existence of a bifurcation domain within the plastic limit (Darve et al., 2004; Nicot et al., 2009). A fundamental task (or end) of the mechanics is to translate knowledges and observations into the mathematical relation, which is capable of predicting or simulating the reality. Thus, developing models that succeed in incorporating comprehensive constitutive features of the granular materials becomes a challenging task to the mechanics community.

A large number of phenomenological models have been built in recent decades. In this kind of models, attempts are made to formulate different observed phenomena into a mathematical framework. Different theories have been proposed: elasto-plastic theories (Drucker D. C., 1952; Hill, 1967; Rice, 1970, 1975), endochronic models (Bazant and others, 1978), hypo-plastic theories (Kolymbas, 1991), and non-linear incremental models (Darve, 1990; Darve et al., 1995b). Phenomenological models normally have to introduce an exceeding number of parameters, furthermore, most of these parameters lack physical grounds.

Building a constitutive relation obedient to the material's nature inevitably faces the difficulty of taking into account the constitutive behavior of the material at smaller scales, from which the macro-scale behavior originates. To this end, a multi-scale technique is worthy of being developed. By sophisticatedly establishing links among quantities in different scales, the multi-scale approach embeds the microscopic physical nature into a macroscopic constitutive relation. This grants us a new prospective to formulate relations for better matching the reality.

A prerequisite for applying the multi-scale approach is to seek an appropriate scale, smaller than the macro-scale, to which macroscopic behaviors can be comprehensively associated. A series of enlightenments have been given by the dedication of micro-structure investigation in chapter 3, where characteristic geometrical elements, namely the meso-loops and force-chains, are highlighted at a meso-scale. Such a scale is essential in views of deriving a constitutive relation.

In this manuscript, the meso-loop is employed in building the constitutive model, as the hexagon formed by 6 particles is considered as the basic element. There are two advancing aspects in using meso-loops. In a static or quasi-static 2D granular system, the whole material area can be seamlessly tessellated into meso-loops. This enables the material's volumetric variation to be intrinsically attributed to meso-loops. On the other side, differing from the way considering contacts as mutually independent entities, the meso-loop geometrically orders contacts into a group.

In this chapter, the modified H-directional model, a model developed in the framework of multi-scale approaches, is proposed in extension of the H-directional model proposed by [Nicot and Darve \(2011b\)](#). A review will be first given on the H-directional model and its predecessor the micro-directional model ([Nicot et al., 2005](#)) in section 4.1. Then the modified H-directional model is introduced and validated in section 4.2.

## 4.1 Reviews on the micro-directional model and the H-directional model

Building the constitutive relation needs the stress and strain tensors to be related to the macro-scale, that is to say the representative elementary volume (REV) scale. Furthermore, the multi-scale approach indicates a smaller scale to be associated with the macro-scale. This smaller scale is normally the grain scale (micro-scale) or the grain cluster scale (meso-scale). Quantities in micro-scale or meso-scale involve static variables, i.e. the contact force, and kinematic variables, which decide the geometrical variation

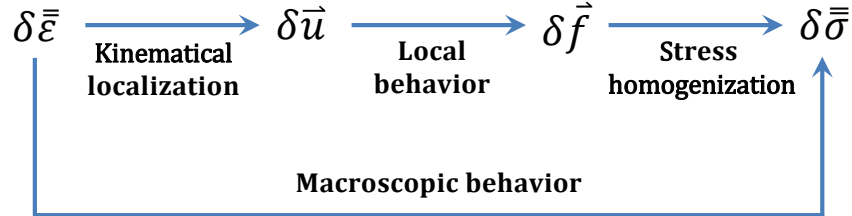


Figure 4.1: General homogenization scheme for multi-scale approaches.

of the elementary entities at this scale. These two kinds of variables are related by the local constitutive law, which defines the local behavior on the micro-scale. However, the different scales can be bridged by mathematical procedure, in which quantities in small scale can be related to macro-scale quantities: the stress averaging, and kinematic localization. Then there are three relations should be formulated in the general multi-scale scheme, as shown in Figure 4.1, exemplified by the case of solving stress from known strain:

- kinematical localization: the local kinematic variables are estimated from the strain tensor;
- local constitutive law: solving local kinematic variables with known local static variables;
- stress averaging: the stress tensor is computed from the local static variables.

All constitutive models discussed in this chapter adopt the scheme departing from incremental strain and returning incremental stress. Therefore the procedures presented in Figure 4.1 will be the guide line for constitutive modeling in this chapter.

#### 4.1.1 The micro-directional model

The micro-directional model, a 3D constitutive model using a multi-scale approach, was first proposed in attempt of simulating the snow behavior (Nicot, 2003, 2004). It was later generalized to apply to other granular materials (Nicot et al., 2005).

At the particle scale, when an incremental strain is imposed to a granular assembly on its boundary grains, relative displacements will take place between the boundary grains and the neighboring grains. This simultaneously induces incremental forces on these neighboring grains. According to Newton's second law, imbalance forces spring on the grains, which are originally in equilibrium, and drive them into an attempt to reach a new equilibrium state. This, again but unavoidably, induces relative displacements between grains in the vicinity. The disturbance caused by the load then propagates throughout the material, the movement of particles transmits neighbors after neighbors. This is the way the load progressively disturbs the granular material and leads to the particles rearrangement and internal forces redistribution. The constitutive modeling of the multi-scale approach, in essence, is little more than to quantify this procedure into an analytical relation between the incremental strain and stress.

However, it is impossible to solve the enormous number of balance equations for each particle in one single constitutive relation. Thus, the multi-scale approach cannot bypass an introduction of additional assumptions, in order to reduce the number of degree of freedom to be solved in the constitutive relation. In the micro-directional model, the granular assembly consists of contacts distributing along different directions, following a directional distribution  $\omega(\vec{n})$  in the physical space, with the unit vector  $\vec{n}$  denoting the contact direction. As an assumption in this model, contacts along different directions evolve independently from each other. Another assumption is the purely affine deformation in the material; this means that the relative displacement between two particles pairing in contact  $c$  is expressed by projecting the global incremental strain  $\delta\bar{\epsilon}$  along the contact direction. The radius of all grains are set to the same value  $r_g$ , the penetration is neglected in this model. The strain localization is given as below,

$$\begin{aligned}\delta\vec{u}^c &= 2r_g\delta\bar{\epsilon} : \vec{n}^c, \\ \delta\vec{u}_n^c &= (\delta\vec{u}^c \cdot \vec{n}^c)\vec{n}^c, \\ \delta\vec{u}_t^c &= \delta\vec{u}^c - \delta\vec{u}_n^c.\end{aligned}\tag{4.1}$$

where  $\delta\vec{u}^c$  is the relative displacement between two particles forming the contact  $c$ , oriented along the direction represented by unit vector  $\vec{n}^c$ ,  $\delta u_n^c$  and  $\delta u_t^c$  are normal and tangential components of  $\delta\vec{u}^c$ .

As the granular assembly is modeled by individual contacts, the local behavior can be as simple as the contact law of the single contact, which determines the incremental forces (denoted by  $\delta\vec{F}_n^c$  and  $\delta\vec{F}_t^c$ ), when incremental deformations on the contact (denoted by  $\delta\vec{u}_n^c$  and  $\delta\vec{u}_t^c$ ) is given. The choice of a contact law depends on the micro-physics we intend to

describe behind the macro behavior of the material. The elasto-plastic performance of the granular material largely stems from the elastic-frictional nature on the contact level. In this manuscript, the elastic-frictional contact law is adopted, including an elastic and a plastic law, the latter comes to effect when the tangential force reaches a pointed value that depends on the magnitude of the normal force. It is expressed as follows:

$$\begin{aligned}\delta\vec{F}_n^c &= -k_n\delta\vec{u}_n^c, \\ \delta\vec{F}_t^c &= \min \left\{ \left\| \vec{F}_t^c + k_t\delta\vec{u}_t^c \right\|, \tan\varphi_g \left( \left\| \vec{F}_n^c - k_n\delta\vec{u}_n^c \right\| \right) \right\} \cdot \vec{\zeta} - \vec{F}_t^c, \\ \vec{\zeta} &= \frac{\vec{F}_t^c + k_t\delta\vec{u}_t^c}{\left\| \vec{F}_t^c + k_t\delta\vec{u}_t^c \right\|},\end{aligned}\quad (4.2)$$

where  $k_n$  and  $k_t$  are respectively normal and tangential stiffnesses on the contact,  $\vec{F}_n^c$  and  $\vec{F}_t^c$  are normal and tangential contact forces,  $\varphi_g$  is the inter-particle friction angle. The tension is not allowed on the contact; the contact force turns to zero, once a tension occurs.

The strain averaging or localization scheme varies from one model to another, according to different prescribed assumptions. In contrast, the translation between micro and macro static variables, the stress averaging scheme, is much more simplex, which widely refers to Love formula (Love, 2013; Christoffersen et al., 1981; Mehrabadi et al., 1982),

$$\sigma_{ij} = \frac{1}{V} \sum_{c=1}^{N_c} f_i^c l_j^c, \quad (4.3)$$

where  $f_i^c$  and  $l_j^c$  are respectively the  $i$ th and  $j$ th coordinate of contact force and contact branch on contact  $c$ ,  $N_c$  is the number of contacts in the specimen with a volume  $V$ .

In multi-scale approach, when the status of contacts arranging along different directions is quantified by  $\bar{\omega}(\vec{n})$ , the frequency of contacts along direction  $\vec{n}$ , the equation 4.3 can be transformed into

$$\sigma_{ij} = \frac{2r_g}{V} \iint_D \hat{F}_i n_j \bar{\omega}(\vec{n}) d\Omega, \quad (4.4)$$

where  $d\Omega$  is the infinitesimal solid angle, which varies in the integration surface  $D$ .  $\hat{F}_i$  is the  $i$ th coordinate of average force of all contacts along the direction represented by the unit vector  $n_j$ . Differentiation of equation 4.4 gives,

$$\delta\sigma_{ij} = \frac{2r_g}{V} \left( \iint_D \delta\hat{F}_i n_j \bar{\omega}(\vec{n}) d\Omega + \iint_D \hat{F}_i n_j \delta\bar{\omega}(\vec{n}) d\Omega \right). \quad (4.5)$$

The material fabric in the assembly may evolve state by state. This evolution is described by the change of the distribution  $\omega(\vec{n})$ , indicating that the contact density varies along each direction. When acting as a key function in the expression of the stress,  $\omega(\vec{n})$  is significant in this model because it not only presents the arrangement of the material texture, but also prominently controls the mechanical response of the material. In fact, several empirical relations can be used to predict the value of  $\omega(\vec{n})$  by referring to different mechanical properties of the material (Chang et al., 1990; Yin et al., 2010, 2011b,a; Chang, 2014). In this model, the relation reported by Oda (1972a); Oda et al. (1980); Calvetti et al. (1997) is built inside, in order to calculate the number of contacts along a given direction in each sept, on the basis of the incremental strain in last step. This relation thinks of the contact number increasing in the contractant directions and decreasing in the dilatant ones, expressed as below,

$$\frac{\delta\omega(\vec{n})}{\omega(\vec{n})} = a(\delta\bar{\epsilon} : \vec{n}) \cdot \vec{n}, \quad (4.6)$$

where  $a$  is an adjustable coefficient for different materials. The meaning of this function is that during a quasi-static loading, the fabric follows the variation of the strain, and the stress response subsequently follows according to the fabric. Consequently, in the implementation of this model, when an incremental strain is given, both fabric and stress evolution can be also determined.

### 4.1.2 limitations of micro-directional model

To point out the limitation of the model, we have to go back to two assumptions ordered in terms of strain localization: (1) there is an affine deformation inside material, enabling the global strain to be projected into each direction of the space to obtain local deformation; and (2) contacts in different directions develop independently from each other. They are foundations of this model and where the convenience of this model comes from, however, as well as where the limitation comes from.

The first assumption can be alternatively expressed as that: the inter-particle contacts fabric is the only origination of the global strain. However, it is mostly paradoxical to the reality. As highlighted in the section 3.3, the global strain derives not only from the deformation between contacting particles, but also from the fabric rearrangement inside the material. From a meso-scale viewpoint, three parts contribute to the global volumetric strain: the relative displacement on the contact, the conversion between different categories of meso-loops (represented by the conversion between  $L_3$  and  $L_{6+}$ )

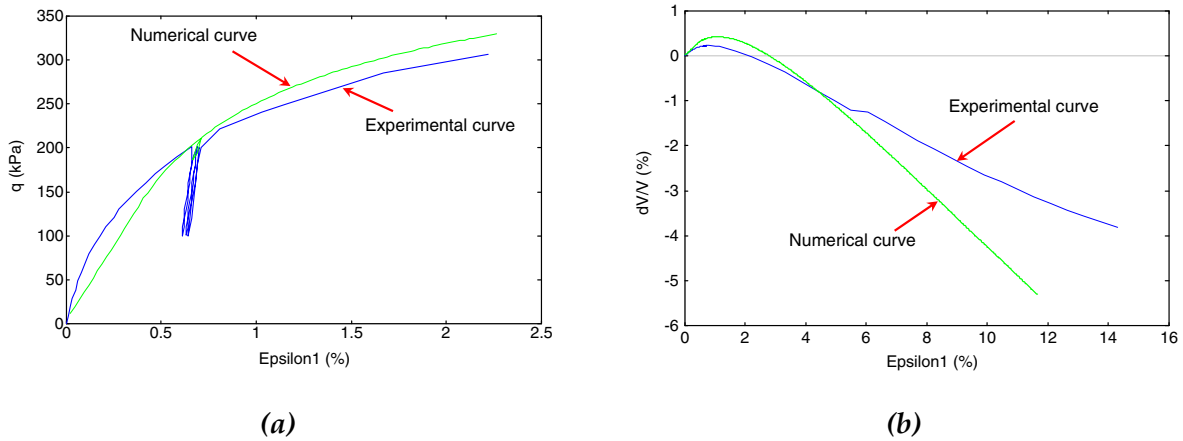


**Figure 4.2:** Deviatoric stress and volumetric strain evolution in terms of axial strain, in the calibration along a symmetric drained triaxial loading path, involving unloading and reloading stages.

and the area variation of meso-loops caused by the shape changing (to which,  $L_6$  contribution the most). Moreover, the latter two parts cannot recover during the unloading, deriving the plastic volumetric strain. In fact, when there is an incremental strain in a granular assembly, a part (may a large part) of it will be absorbed by the void inside meso-loops, especially large meso-loops (such as  $L_6$ ), and by the conversion between different categories of meso-loops, especially the changing between  $L_3$  and  $L_{6+}$ . the relative displacement on the contact only correspond to the remaining part of the incremental strain. The effect of the deformation at contact point only dominates in the case when the material fabric has little way to rearrange, such as in the early stage of a drained biaxial test, when the contractancy of the dense specimen is mainly attributed to the inter-particle penetrations in contacts (demonstrated in subsection 3.3.3). Therefore, the fabric rearrangement in the meso-scale should be considered in the constitutive model.

However, the fabric rearrangement in the meso-scale and its effect on the global strain are ignored in this model, giving rise to two consequences: due to the ignorance on the part of strain deriving from the fabric arrangement, there is an underestimation toward the volumetric contractancy or, inversely, an overestimation toward the dilatancy; the incremental strain is totally assigned on contact points, causing an overestimation of the local contact deformation and, consequently, an over-calculated stress. There is therefore an exceedingly higher stiffness than in reality. Figure 4.2 exemplifies these unrealistic model responses (Nicot and Darve, 2011b), when the micro-directional model is calibrated by experimental results under an antisymmetric drained triaxial loading

path. Even though the performance of the model is quite satisfying, a higher stiffness can be captured before  $\varepsilon_1 = 1.5\%$  in Figure 4.2a, as a little more sloped stress-strain curve than experimental one is observed. This is because in the experiment, the existence of meso-loops in the specimen weakens the stiffness of the material, whereas there is not this kind of meso-structures in the numerical model. On the other side, in Figure 4.2b, there is a notably smaller dilatancy in the experiment than in the numerical test after about  $\varepsilon_1 = 6.0\%$ . Meso-loops in the experiment absorb a part of subjected strain, leading to this smaller dilatancy.

To mention is that the fabric rearrangement here cannot be addressed by changing the contact orientational distribution  $\omega$ , formulated by equation 4.6, because  $\omega$  is not relevant with the strain localization but stress averaging, equation 4.6 just gives a prediction of the contact distribution in next calculation step. To capture the fabric rearrangement in the material requires to correctly describe the relative displacements among contacts. However, the second assumption makes this point impossible to be reached in the model, when contacts in different directions are set up to evolve independently from each other.

To overcome the limitation of this model, features in terms of the fabric rearrangement in the meso-scale should be considered. In the other word, the constitutive model should include two natures: (1) entities resembling meso-loops, which are competent of describing relative displacements among contacts; and (2) the conversion among meso-loop categories of different shape (different side number). The H-directional model, proposed by Nicot and Darve (2011b), gave the first but a nice solution on the first point.

### 4.1.3 H-directional model

The idea of incorporating the meso-scale and meso-loops in the model cradles the H-directional model, a 2D constitutive model using a multi-scale approach, proposed by Nicot and Darve (2011b) in extension of the micro-directional model. The hexagon, a entity as the embodiment of  $L_{6+}$ , is introduced into this model.

The major difference of this model from its predecessor is that, the hexagon takes the place of the single contact to be the directional element constituting the material fabric. The hexagon, as shown in Figure 4.3, consists of six particles with same radius contacting head to end to form a closed loop. This six pattern arranges axi-symmetrically both around the axis  $\vec{n}$  and  $\vec{t}$ , with  $\vec{n}$  passing through two spheres.  $\vec{n}$ , referring to the direction of the hexagon  $\theta$ , presents its preferring inclination in the global coordinate system of the material ( $x_1 - x_2$ ), when the tangential direction is  $\vec{t}$ .

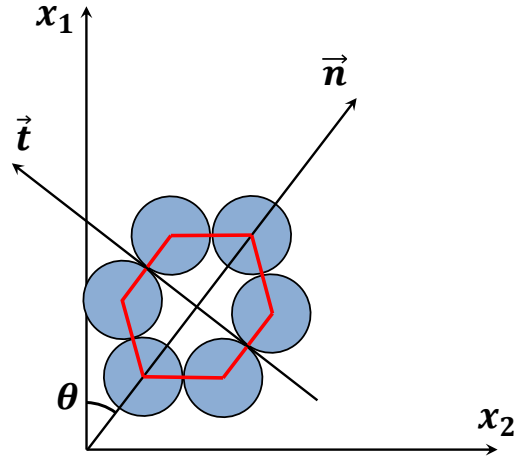


*Figure 4.3: The hexagonal element of the H-directional model.*

The local geometry of the hexagon is illustrated in Figure 4.4, in which numbers label the particle centers. Its length along  $\vec{n}$  and the width extending laterally, along  $\vec{t}$ , are respectively denoted by  $l_1$  and  $l_2$ . Due to an axi-symmetrical layout, the local kinematics of one hexagon is described by only three independent variables: two branch lengths,  $d_1$  and  $d_2$ , which are originally equal to  $2r_g$ , and an opening angle  $\alpha$  between branch  $\vec{l}_{21}$  and  $\vec{n}$ .  $\alpha$  is a significant parameter, controlling the deformation and the void ratio inside the hexagon, and therefore, used to calibrate the volumetric strain of the specimen. In this model, the void ratio of a hexagon is assumed to be same as the void ratio inside it, which is expressed as below,

$$e(\vec{n}) = \frac{4\sin\alpha(1 + \cos\alpha)}{\pi} - 1. \quad (4.7)$$

In terms of local static variables, as shown in Figure 4.4, the symmetry and the equilibrium of this system are ensured by external forces  $\vec{F}_1$  and  $\vec{F}_2$ , exerted respectively symmetrically in the directions of  $\vec{n}$  and  $\vec{t}$ . Three independent variables in terms of the contact force, which form the entire local static information, can be identified:  $N_1$  and  $T_1$ , the normal and shear force between particle 1 and 2, and  $N_2$ , the normal force between particle 2 and 3. Held as an assumption is that to maintain the axi-symmetry around the axis  $\vec{t}$ , the tangential displacement and force between particle 2 and 3 are

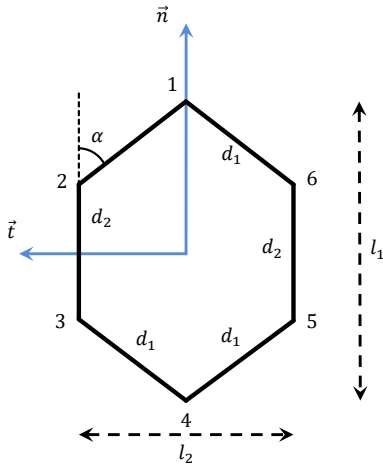


Figure 4.4: local kinematic variables in a hexagon

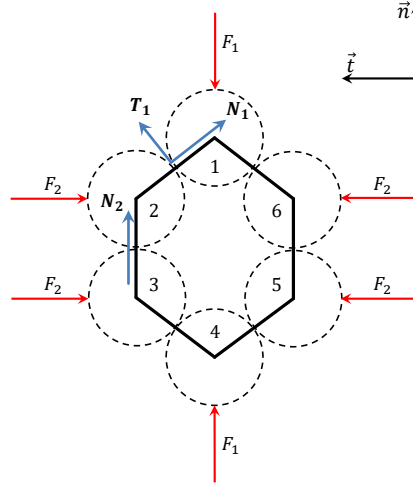


Figure 4.5: local static variables in a hexagon

eliminated. These internal static variables are related to three local kinematic variables in an incremental form by the elasto-frictional law:

$$\begin{aligned}\delta N_1 &= -k_n \delta d_1, \\ \delta N_2 &= -k_n \delta d_2, \\ \delta T_1 &= \min\{|T_1 + k_t d_1 \delta \alpha|, \tan \varphi_g (N_1 - k_n \delta d_1)\} \zeta - T_1,\end{aligned}\tag{4.8}$$

where  $\zeta$  is the sign of  $T_1 + k_t d_1 \delta \alpha$ ,  $k_n$  and  $k_t$  are respectively normal and tangential contact stiffness.

A series of hexagons, instead of single contacts in the microdirectional model, distribute along different orientations, also following a directional distribution  $\omega(\theta)$  in a polar system, where  $\theta$  is the inclination angle of  $\vec{n}$ , i.e.  $\vec{n} = \cos \theta \vec{x}_1 + \sin \theta \vec{x}_2$ . An affinity on the deformation is also assumed. The variation of the dimension on each hexagon, presented by  $\delta l_1$  and  $\delta l_2$ , is then related to the global incremental strain  $\delta \varepsilon_{ij}$  based on its orientation:

$$\begin{aligned}\delta l_1 &= -l_1 \delta \varepsilon_{ij} n_i n_j = -l_1 (\delta \varepsilon_1 n_1^2 + \delta \varepsilon_2 n_2^2), \\ \delta l_2 &= -l_2 \delta \varepsilon_{ij} t_i t_j = -l_2 (\delta \varepsilon_1 t_1^2 + \delta \varepsilon_2 t_2^2),\end{aligned}\tag{4.9}$$

where, restrained by the symmetrical configuration, the material is assumed not to rotate, alternatively saying,  $\delta\bar{\varepsilon} = \begin{bmatrix} \delta\varepsilon_1 & 0 \\ 0 & \delta\varepsilon_2 \end{bmatrix}$ .

The local constitutive relation formulates the behavior of a individual hexagon, determining incremental internal forces, when the variation of the dimension of the hexagon,  $\delta l_1$  and  $\delta l_2$ , is given. The local geometrical compatibility is expressed as:

$$\begin{aligned} l_1 &= d_2 + 2d_1 \cos\alpha, \\ l_2 &= 2d_1 \sin\alpha. \end{aligned} \quad (4.10)$$

Equations 4.10 transformed in incremental form give,

$$\begin{aligned} \delta l_1 &= \delta d_2 + 2\delta d_1 \cos\alpha - 2d_1 \sin\alpha \delta\alpha, \\ \delta l_2 &= 2\delta d_1 \sin\alpha + 2d_1 \cos\alpha \delta\alpha. \end{aligned} \quad (4.11)$$

Checking the balance condition on particle 2 along direction  $\vec{n}$  yields:

$$N_2 = N_1 \cos\alpha + T_1 \sin\alpha, \quad (4.12)$$

and its incremental form,

$$\delta N_2 = \delta N_1 \cos\alpha - N_1 \sin\alpha \delta\alpha + \delta T_1 \sin\alpha + T_1 \cos\alpha \delta\alpha. \quad (4.13)$$

The substitution of equations 4.8 into equation 4.13 gives the balance equation expressed by kinematic variables in a incremental form. Combining with incremental compatibility equations 4.11 yields a linear system deriving  $\delta l_1$  and  $\delta l_2$  from incremental internal kinematic variables,  $d_1$ ,  $d_2$  and  $\alpha$ ,

$$\begin{bmatrix} 2\cos\alpha & 1 & -2d_1 \sin\alpha \\ 2\sin\alpha & 0 & 2d_1 \cos\alpha \\ \cos\alpha + A & -1 & \frac{(N_1 - B)\sin\alpha - T_1 \cos\alpha}{k_n} \end{bmatrix} \begin{bmatrix} \delta d_1 \\ \delta d_2 \\ \delta\alpha \end{bmatrix} = \begin{bmatrix} \delta l_1 \\ \delta l_2 \\ C \end{bmatrix}, \quad (4.14)$$

in the elastic regime,  $A = 0$ ,  $B = k_t d_1$  and  $C = 0$ , and in the plastic regime,  $A = \zeta \tan\phi_g \sin\alpha$ ,  $B = 0$  and  $C = \sin\alpha \left( \frac{\zeta \tan\phi_g N_1 - T_1}{k_n} \right)$ .

When the local kinematic and static variables are solved, the stress averaging process will be used to obtain the global stress. According to the Love formula (equation 4.4), a loop stress  $\tilde{\bar{\sigma}}(\theta)$  referring to local coordinate system  $\vec{n} - \vec{t}$  can be given for every hexagon, as follows,

$$\begin{aligned}\tilde{\bar{\sigma}}(\theta) &= \begin{bmatrix} \tilde{\sigma}_n(\theta) & 0 \\ 0 & \tilde{\sigma}_t(\theta) \end{bmatrix}, \\ \tilde{\sigma}_n(\theta) &= 4N_1d_1\cos^2\alpha + 4T_1d_1\sin\alpha\cos\alpha + 2N_2d_2, \\ \tilde{\sigma}_t(\theta) &= 4N_1d_1\sin^2\alpha - 4T_1d_1\sin\alpha\cos\alpha.\end{aligned}\tag{4.15}$$

An integration of the loop stress along all the orientations renders the global stress,

$$\bar{\sigma} = \frac{1}{V} \int \omega(\theta) \bar{P}^{-1} \tilde{\bar{\sigma}}(\theta) \bar{P} d\theta,\tag{4.16}$$

where  $\bar{P}$  is the transport matrix, being equal to  $\begin{bmatrix} \cos\theta & \sin\theta \\ -\sin\theta & \cos\theta \end{bmatrix}$ ,  $V$  is the volume of the specimen.

Under this framework, two assumptions propounded in micro-directional model and their inducing consequences are invalidated; contacts in the fabric will displace never independently, but compatibly with other contacts in individual hexagons. This, however, do not indicate a comprehensive compatibility among all contacts in the specimen, as it is only satisfied on the scale of an individual hexagon.

## 4.2 Modified H-directional model

In the H-directional model, it is assumed that there is not any rotation of the spheres. From a constitutive point of view, this assumption is at the origin of the impossibility for this model to present the global shear behavior. The symmetrical configuration has internal shear forces offsetting against each other, which in the end contribute nothing to the shear components of the global strain. Consequently, a rotation on the principals of both stress and strain is not practicable. This flaw narrows the extent to which the model is to be applied, and causes the inflexibility of the model in different stress and strain environments and loading paths, especially as would be implemented in numerical tools, such as Finite element method (FEM), where different mechanical conditions can be encountered.

The hope of making an improvement lies on breaking the symmetry of the hexagon. A series of modifications have been made along this way; a point-symmetrical hexagon is introduced to replace the axi-symmetrical one, while the basic framework of the model keeps unchanged.

### 4.2.1 Constitutive relations

In the modified model, a rotation of the central line 16, qualified by angle  $\psi$  ( $\gamma_{12} = \tan\psi$ ), is allowed from the element directional vector  $\vec{n}$ , as shown in Figure 4.6a (Arabic numerals label six particles centers). Consequently, the system is symmetrical in terms neither of  $\vec{n}$  nor  $\vec{t}$ , but of its geometrical centroid. Following a symmetry breaking, a series of new degrees of freedom arises, which, subsequently, require more kinematic variables to describe. Three couples of variables,  $d_1 - \alpha_1$ ,  $d_2 - \alpha_2$  and  $d_3 - \alpha_3$ , are employed to quantify the corresponding length and inclination of three geometrically independent laterals, branches 13, 12 and 35.  $l_1$  and  $l_2$ , projections of 16 on  $\vec{n}$  and 25 on  $\vec{t}$ , characterize the size of the hexagon. Neglecting the penetration between particles, the void ratio of a deformed hexagon  $e(\vec{n})$ , which also only calculates the internal void ratio enclosed by branches, is given as below,

$$e(\vec{n}) = \frac{2[\sin(\alpha_1 + \alpha_2) + (\sin\alpha_1 + \sin\alpha_2)\cos\alpha_3]}{\pi} - 1. \quad (4.17)$$

When the condition  $\alpha_1 = \alpha_2$  and  $\alpha_3 = 0$  are fulfilled, equation 4.17 will become equation 4.7.

The static information refers to three independent contacts, 13, 12 and 35, when remainders can be mirrored with respect to the hexagon centroid. Thus, there are six static variables, illustrated in Figure 4.6c, with normal and tangential forces for each independent contacts. They are  $N_1 - T_1$ ,  $N_2 - T_2$  and  $N_3 - T_3$ , which can be incrementally related to the kinematic variables by the elasto-plastic law,

$$\begin{aligned} \delta N_i &= -k_n \cdot \delta d_i, \\ \delta T_i &= \min\{|T_i + k_t d_i \delta \alpha_i|, \tan\varphi_g(N_i - k_n \delta d_i)\} \xi_i - T_i, \end{aligned} \quad (4.18)$$

where  $i = (1, 2, 3)$ ,  $\xi_i$  is the sign of  $T_i + k_t d_i \delta \alpha_i$ ,  $k_n$  and  $k_t$  are respectively normal and tangential contact stiffness. It is worthy of noting that a strong simplification in this model is that the rotations on particles are fixed. This may lead to unbalanced banding moment on particles or in the total configuration.

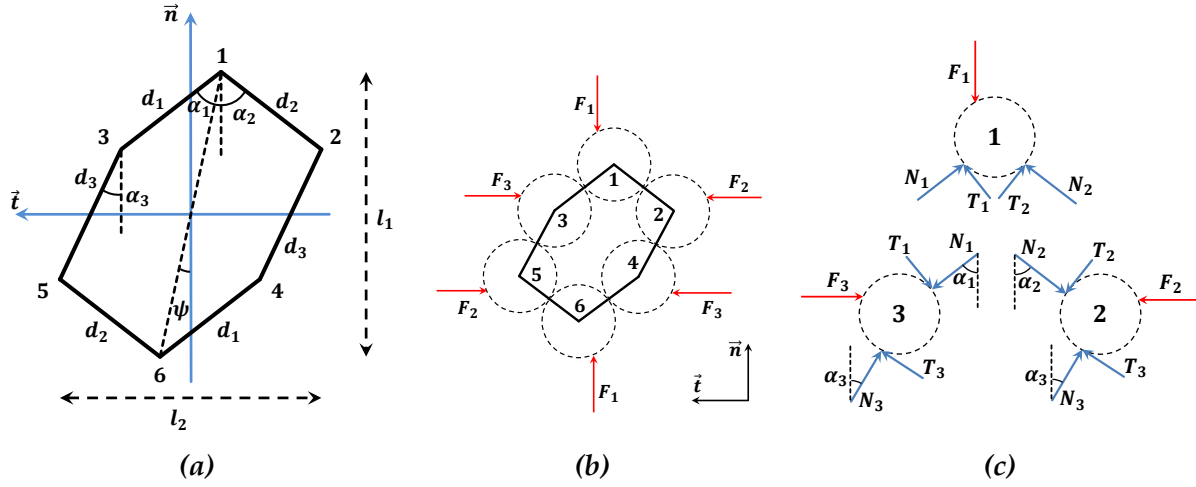


**Figure 4.6:** Configuration of the hexagon with local kinematic and static variables. (a) local kinematic variables; (b) layout of particles in the hexagon subjected to external forces; (c) local static variables

The geometrical compatibility among local kinematic variables is ensured by the compatibility equations:

$$\begin{aligned}
 l_1 &= d_1 \cos \alpha_1 + d_2 \cos \alpha_2 + d_3 \cos \alpha_3, \\
 l_2 &= d_1 \sin \alpha_1 + d_2 \sin \alpha_2 + d_3 \sin \alpha_3, \\
 \gamma_{12} &= \frac{d_1 \sin \alpha_1 + d_3 \sin \alpha_3 - d_2 \sin \alpha_2}{l_1}.
 \end{aligned} \tag{4.19}$$

The equilibrium of particles 1 and 2 along  $\vec{n}$  and particle 3 along  $\vec{t}$  yields three balance equations,

$$\begin{aligned}
 N_3 \cos \alpha_3 + T_3 \sin \alpha_3 &= N_1 \cos \alpha_1 + T_1 \sin \alpha_1, \\
 N_3 \cos \alpha_3 + T_3 \sin \alpha_3 &= N_2 \cos \alpha_2 + T_2 \sin \alpha_2, \\
 N_1 \sin \alpha_1 - T_1 \cos \alpha_1 &= N_2 \sin \alpha_2 - T_2 \cos \alpha_2.
 \end{aligned} \tag{4.20}$$

Noteworthy is that all particles in the hexagon is assumed to be stationary in all cases. The external forces then are dependent on the solved internal forces.

So far, when the deformation on the scale of the hexagon, i.e.  $\delta l_1$  and  $\delta l_2$ , is provided, there are 12 unknowns of variational form waiting to be solved in the system, incorporating 6 kinematic and 6 static variables. Solving 12 unknowns requires 12 equations, of which, 6 are the contact law equations 4.18, 3 are the variational form of

compatibility equations 4.19 and remaining 3 are given by the variational form of balance equations 4.20. Combining all these equations above generates 6 independent equations,

$$\begin{aligned}
& (-k_n \cos \alpha_1 - \sin \alpha_1 \cdot A_1) \delta d_1 + (k_n \cos \alpha_3 + \sin \alpha_3 \cdot A_3) \delta d_3 + \\
& (T_1 \cos \alpha_1 - N_1 \sin \alpha_1 + \sin \alpha_1 \cdot B_1) \delta \alpha_1 + (N_3 \sin \alpha_3 - T_3 \cos \alpha_3 - \sin \alpha_3 \cdot B_3) \delta \alpha_3 \\
& = -\sin \alpha_1 \cdot C_1 + \sin \alpha_3 \cdot C_3, \\
& (-k_n \cos \alpha_2 - \sin \alpha_2 \cdot A_2) \delta d_2 + (k_n \cos \alpha_3 + \sin \alpha_3 \cdot A_3) \delta d_3 + \\
& (T_1 \cos \alpha_2 - N_2 \sin \alpha_2 + \sin \alpha_2 \cdot B_2) \delta \alpha_2 + (N_3 \sin \alpha_3 - T_3 \cos \alpha_3 - \sin \alpha_3 \cdot B_3) \delta \alpha_3 \\
& = -\sin \alpha_2 \cdot C_2 + \sin \alpha_3 \cdot C_3, \\
& (-k_n \sin \alpha_1 + \cos \alpha_1 \cdot A_1) \delta d_1 + (k_n \sin \alpha_2 - \cos \alpha_2 \cdot A_2) \delta d_2 + \\
& (N_1 \cos \alpha_1 - T_1 \sin \alpha_1 - \cos \alpha_1 \cdot B_1) \delta \alpha_1 + (-N_2 \cos \alpha_2 - T_2 \sin \alpha_2 + \cos \alpha_2 \cdot B_2) \delta \alpha_2 \\
& = \cos \alpha_1 \cdot C_1 - \cos \alpha_2 \cdot C_2, \\
& \cos \alpha_1 \cdot \delta d_1 + \cos \alpha_2 \cdot \delta d_2 + \cos \alpha_3 \cdot \delta d_3 \\
& - \sin \alpha_1 \cdot d_1 \cdot \delta \alpha_1 - \sin \alpha_2 \cdot d_2 \cdot \delta \alpha_2 - \sin \alpha_3 \cdot d_3 \cdot \delta \alpha_3 \\
& = \delta l_1, \\
& \sin \alpha_1 \cdot \delta d_1 + \sin \alpha_2 \cdot \delta d_2 + \sin \alpha_3 \cdot \delta d_3 \\
& + \cos \alpha_1 \cdot d_1 \cdot \delta \alpha_1 + \cos \alpha_2 \cdot d_2 \cdot \delta \alpha_2 + \cos \alpha_3 \cdot d_3 \cdot \delta \alpha_3 \\
& = \delta l_2, \\
& [(\sin \alpha_1 - \cos \alpha_1 \cdot \gamma_{12}) / l_1] \delta d_1 + [-(\sin \alpha_2 + \cos \alpha_2 \cdot \gamma_{12}) / l_1] \delta d_2 \\
& + [(\sin \alpha_3 - \cos \alpha_3 \cdot \gamma_{12}) / l_1] \delta d_3 + [d_1 (\cos \alpha_1 + \sin \alpha_1 \cdot \gamma_{12}) / l_1] \delta \alpha_1 \\
& + [d_2 (-\cos \alpha_2 + \sin \alpha_2 \cdot \gamma_{12}) / l_1] \delta \alpha_2 + [d_3 (\cos \alpha_3 + \sin \alpha_3 \cdot \gamma_{12}) / l_1] \delta \alpha_3 \\
& = \delta \gamma_{12},
\end{aligned} \tag{4.21}$$

where

$$\begin{cases} A_i = I_{pla}(i) \cdot \xi_i \cdot k_n \tan \phi_g \\ B_i = I_{ela}(i) \cdot k_t d_i \\ C_i = I_{pla}(i) \cdot [\xi_i \cdot N_i \tan \phi_g - T_i] \end{cases} \quad (i = 1, 2, 3) \tag{4.22}$$

in which,  $i$  ( $i = 1, 2, 3$ ), for both the subscript and the input of the function, identifies the contact,  $\xi_i$  is the sign of the shear direction on contact  $i$  (i.e. the sign of  $T_i + k_t d_i \delta \alpha_i$ ),  $I_{pla}(i)$  and  $I_{ela}(i)$  are indicator functions of the contact state, expressed as below,

$$I_{pla}(i) = \begin{cases} 1 & \text{if contact } i \text{ is plastic} \\ 0 & \text{if contact } i \text{ is elastic} \end{cases} \quad (4.23)$$

$$I_{ela}(i) = 1 - I_{pla}(i).$$

So far, the local constitutive model on an individual hexagon scale (the meso-scale) is enclosed by the equations 4.21, taking into account the variation on the hexagon's dimension, together with the given internal state variables (static and kinematic). As a special case, when an axi-symmetrical configuration is satisfied as for the H-directional model ( $\alpha_1 = \alpha_2$ ,  $\alpha_3 = 0$ ,  $d_1 = d_2$ ,  $N_1 = N_2$ ,  $T_1 = T_2$  and  $T_3 = 0$ ), the balance equations, compatibility equations and contact constitutive equations will respectively degrade into those operating for the H-directional model.

The stress averaging is also processed according to Love formula (equation 4.3). The kinematic localization procedure in this modified version includes the shear strain, expressed as follows,

$$\begin{aligned} \delta l_1 &= -l_1 \delta \varepsilon_{ij} n_i n_j, \\ \delta l_2 &= -l_2 \delta \varepsilon_{ij} t_i t_j, \\ \delta \gamma_{12} &= \delta \varepsilon_{ij} n_i t_j. \end{aligned} \quad (4.24)$$

## 4.2.2 Model performances

In this subsection, the performance of the modified model will be examined along different loading paths. It is worth noting that the aim of this subsection is not to quantitatively validate the model, but to qualitatively test the ability of the model to deliver a reasonable mechanical response.

*Table 4.1: Simulation parameters*

$k_n$ (N/m)	$k_t/k_n$	$\phi_g$ (°)	$e_0(\vec{n})$	initial isotropic stress $p_0$ (kPa)
$0.356 \times 10^6$	0.42	20 – 33	0.35 – 0.63	100 – 300

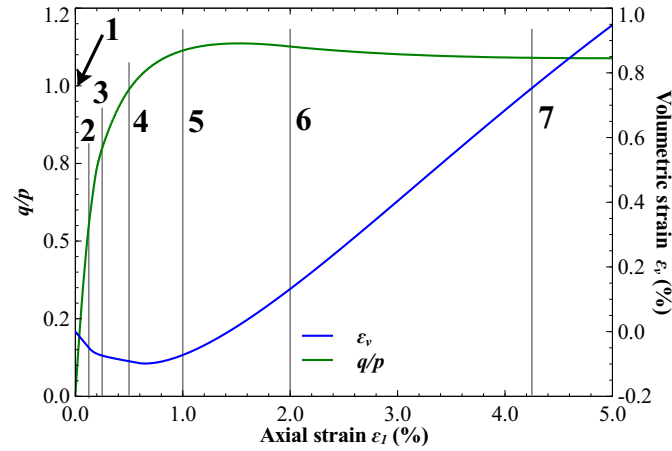


**Figure 4.7:** The stress and volumetric strain response along a drained biaxial loading path, using the modified H-directional model with parameters setting as  $\phi_g = 30^\circ$ ,  $e_0(\vec{n}) = 0.40$  and  $p_0 = 200\text{kPa}$ . line 1 -  $\varepsilon_1 = 0.000$ , line 2 -  $\varepsilon_1 = 0.125$ , line 3 -  $\varepsilon_1 = 0.250$ , line 4 -  $\varepsilon_1 = 0.500$ , line 5 -  $\varepsilon_1 = 1.000$ , line 6 -  $\varepsilon_1 = 2.000$  and line 7 -  $\varepsilon_1 = 4.250$ .

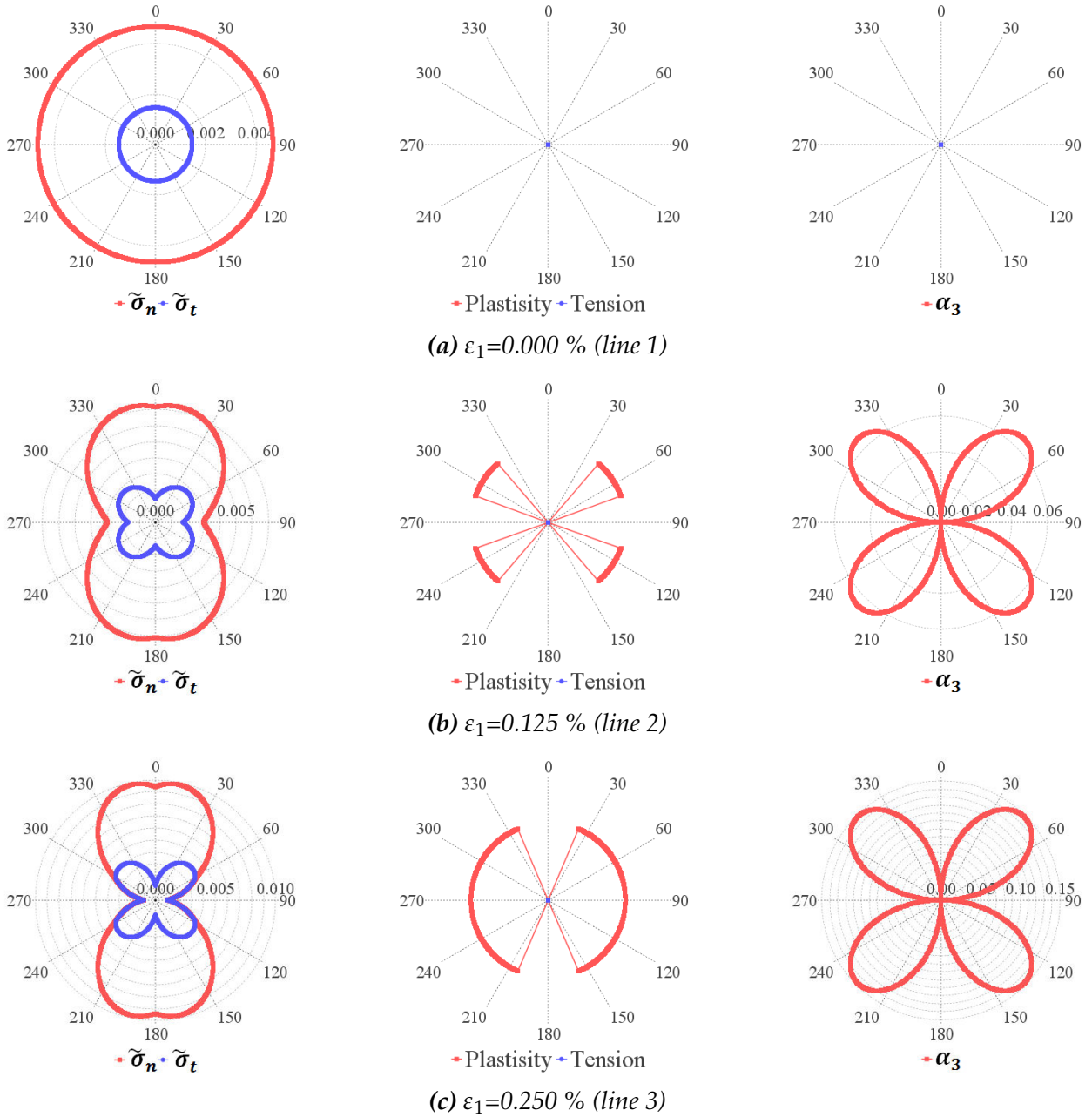
The specimen is installed with hexagons obeying a uniform distribution, laying along different directions in the 2D space. The parameters are set according to Table 4.1, in which only four parameters,  $k_n$ ,  $k_t$ ,  $\phi_g$  and  $e_0(\vec{n})$  (normally dropping in  $[0.35 - 0.65]$ ), refer to microscopic properties. To note is that  $e_0(\vec{n})$ , the initial value of the hexagon internal void ratio, shortly called initial void ratio hereafter, is the local void ratio in the meso-scale, as  $e_0(\vec{n})$  is strongly related to the initial shape of the hexagon (according to equation 4.17, as  $\alpha_1|_{t=0} = \alpha_2|_{t=0}$  and  $\alpha_3|_{t=0} = 0$ ) and associated much to the volumetric behavior of the specimen. In this model, the initial global void ratio is assumed to be equal to the average of the initial local void ratio.

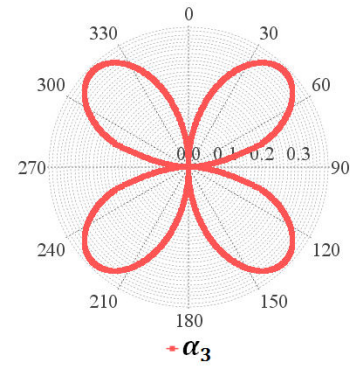
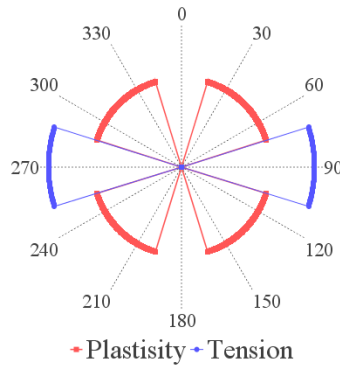
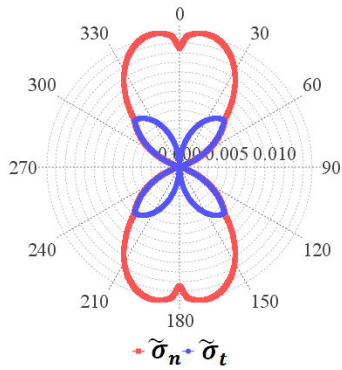
Before the deviatoric load is imposed, a confining procedure operates on the specimen, to prepare it a initial confining pressure, the value of which follows specific condition in different tests. After that, different kinds of anisotropic loading path will be imposed on the specimen to testify the model.

### Drained biaxial test

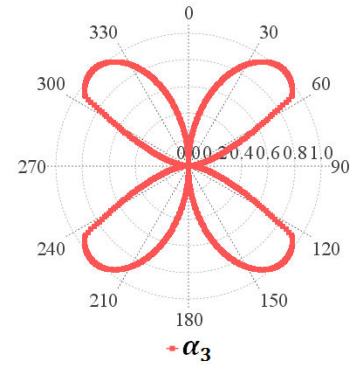
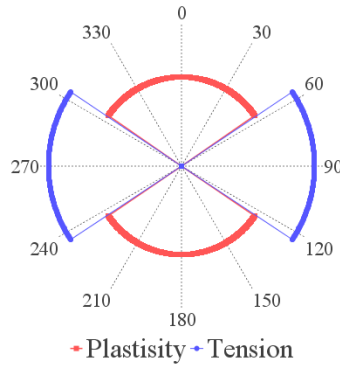
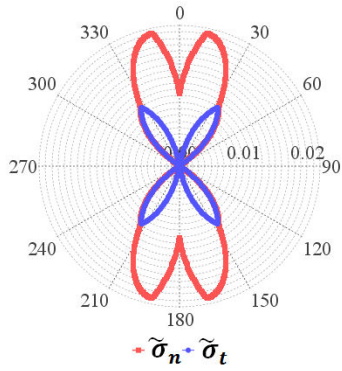
Figure 4.7 presents the stress and volumetric response of the specimen, when it is subjected to a drained biaxial test. The stress ratio  $q/p$  is the ratio of the deviatoric stress  $q$  ( $q = \sigma_1 - \sigma_2$ ) over the hydrostatic pressure  $p$  ( $p = (\sigma_1 + \sigma_2)/2$ ). This ratio, in

**Figure 4.8:** Angular distributions of local variables in strain states, corresponding to lines in Figure 4.7. In each sub-figure, three figures are shown: the angular distribution of the average local stress  $\tilde{\sigma}_n(\theta)$  and  $\tilde{\sigma}_t(\theta)$  (left); the plastic and tensional orientations (center); the evolution of  $\alpha_3$  in terms of orientations (right).

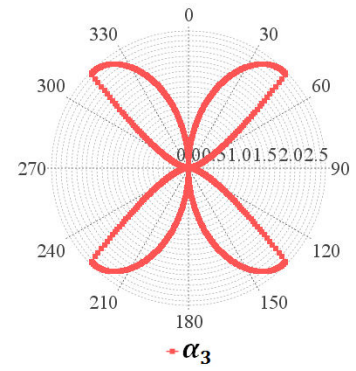
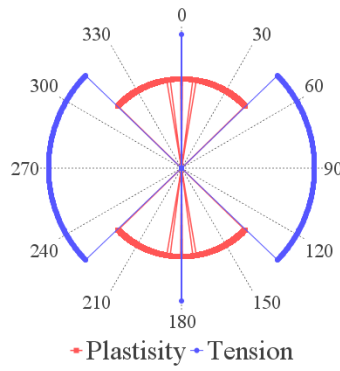
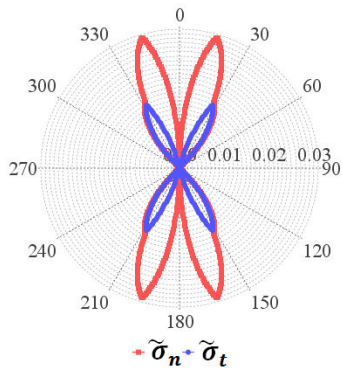




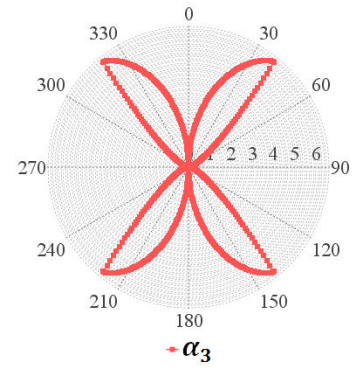
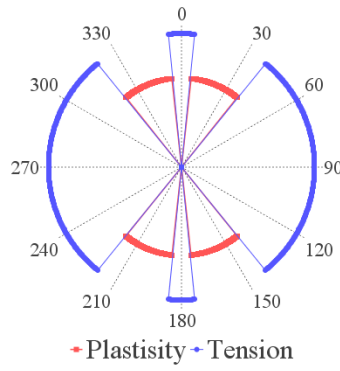
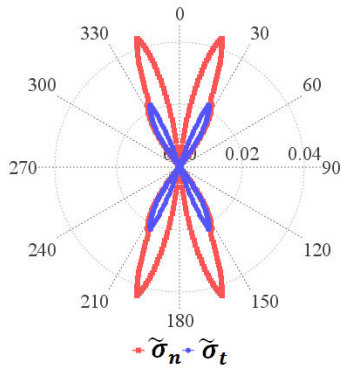
(d)  $\epsilon_1=0.500\%$  (line 4)



(e)  $\epsilon_1=1.000\%$  (line 5)



(f)  $\epsilon_1=2.000\%$  (line 6)



(g)  $\epsilon_1=4.250\%$  (line 7)

cohesionless granular material, is related to macroscopic friction degree  $\phi_m$  as below,

$$\frac{q}{p} = 2 \sin \phi_m. \quad (4.25)$$

The stress peak, around  $q/p = 1.14$ , arrives at a small strain about  $\varepsilon_1 = 3\%$ , after a prominent hardening phase and before a little stress softening. According to equation 4.25, the stress peak corresponds a macro friction  $\phi_m = 34.63^\circ$ . The volumetric strain evolves toward a minimum value at about  $\varepsilon_1 = 0.7\%$  and turns to increase quickly afterwards (dilate regime). Evolutions of the stress ratio and the volumetric strain are in agreement with what is generally observed (experimentally, or numerically using a DEM code) from a qualitative point of view.

The angular distributions of local variables in different strain states are illustrated in Figure 4.8. Figure 4.8a presents that the average local stress  $\tilde{\sigma}_n$  and  $\tilde{\sigma}_t$  are homogeneous at the beginning  $\varepsilon_1 = 0.000$ , as  $\alpha_3$  is equal to 0.0 in any direction. When  $\varepsilon_1 = 0.125$  (Figure 4.8b),  $\tilde{\sigma}_n$  decreases around the lateral direction as growing in other directions. This escalating anisotropy in local stress induces an escalating global stress ratio  $q/p$ . A small plastic band is observed around  $45^\circ$  inclining to the lateral direction, corresponding to the entering to none-elastic phase.  $\alpha_3$  is increasing in a quadrimodal form. As the stress hardening processes to  $\varepsilon_1 = 0.250$  (Figure 4.8c), the plastic zone extends to cover the lateral direction. Both  $\tilde{\sigma}_n$  and  $\tilde{\sigma}_t$  near the lateral direction approach zero. As they reach zero in the last part of the stress hardening phase, the tension failure zone appears and extends symmetrically to the lateral direction. This is what is observed between the strain state  $\varepsilon_1 = 0.500$  and  $\varepsilon_1 = 1.000$  (Figure 4.8d). Noteworthy is that loops aiming to around the axial direction gradually loose its stress. The  $\tilde{\sigma}_n$  around the axial direction vanishes at the stress peak, accompanying with the appearance of the tension sector, which extends afterwards leading to the stress softening (illustrated in Figure 4.8f and 4.8g). The vanishing local stress on the loops around the major loading principal presents the instability of axial directing loops. It is a important feature of this model, which enables it to simulate the persisting loss of contacts along axial direction, caused by the force-chains buckling.

### Drained biaxial test in various parameters

Then, drained biaxial tests are respectively implemented in various  $p_0$  (Figure 4.9a) and various  $\phi_g$  (Figure 4.9b), when keeping other parameters unchanged. As shown in Figure 4.9a, with different stress hardening and softening regimes, specimens initialized

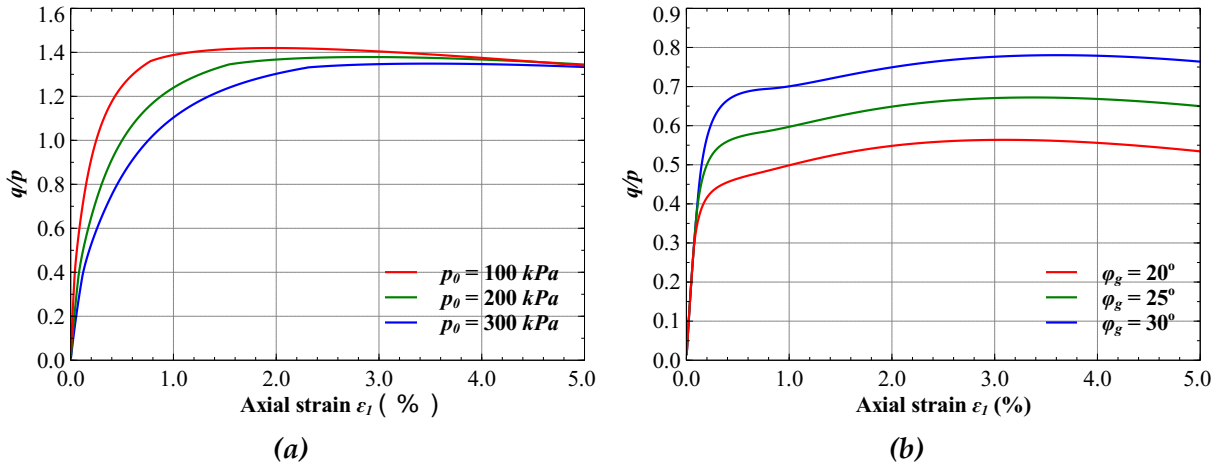


**Figure 4.9:** In drained biaxial test, evolutions of stress ratio in terms of axial strain in specimens of (a) be initialized with various  $p_0$  ( $\phi_g = 30^\circ$  and  $e_0(\vec{n}) = 0.40$ ); and (b) various  $\phi_g$  ( $e_0(\vec{n}) = 0.60$  and  $p_0 = 200 \text{ kPa}$ ).

in different  $p_0$  converge to a value around  $q/p = 1.32$ , corresponding to  $\phi_m = 41.30$ . As confining pressure decreases, the stress is observed to peak sooner with more softening. Figure 4.9b shows that as  $\phi_g$  is increased in the model, stress ratio  $q/p$  also see an increasing trend. However, the shape of the curves of the three specimens appears to be globally similar.

### Undrained biaxial test

The undrained biaxial test is then carried out on two specimens with different  $e_0(\vec{n})$  but same other parameters, to testify whether the model is sensitive enough to the initial density so that it can correctly simulate distinguished behaviors between loose and dense media. The deviatoric stress  $q$  of two specimens is plotted in Figure 4.10 as a function of the hydrostatic stress  $p$ . Two distinct curves can be captured in reminiscence of typical stress paths of loose and dense materials; the dense specimen is able to keep hardening its stress, whereas the loose specimen loses its stress continuously along a line seemingly being at a distance from the plastic limit (Mohr-Coulomb line in Figure 4.10). It is worthy of mentioning that the simulation becomes hard to process (or converge) after the liquefaction, especially when approaching the zero stress, it is also the reason why a section of stress path was missed on the last part to stress zero.

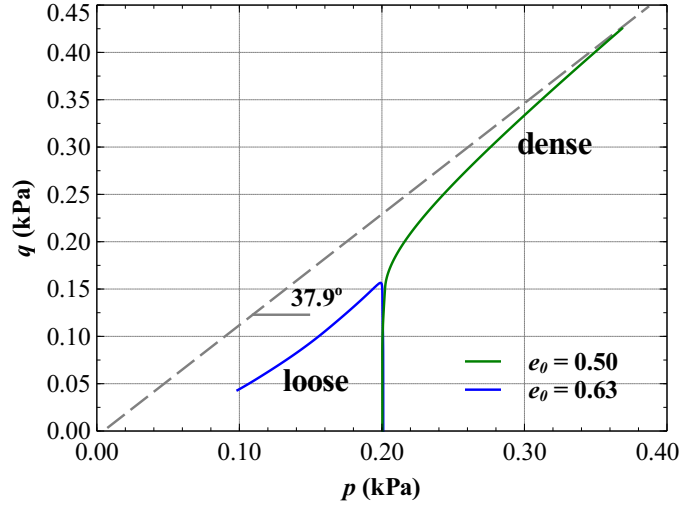


**Figure 4.10:** A divergence on the stress response between a loose ( $e_0(\bar{n}) = 0.50$ ) and a dense ( $e_0(\bar{n}) = 0.63$ ) specimen, subjected to undrained biaxial test. The gray dashed line is the Mohr-Coulomb surface drawn by drained biaxial tests.  $\phi_g = 33^\circ$  and  $p_0 = 200\text{kPa}$ .

### Proportional loading path

A proportional loading path is then considered. After the isotropic confining stage, the specimen is subsequently subjected to a pure strain control loading, with  $\delta\varepsilon_1$  being constant and  $\delta\varepsilon_2$  being prescribed to follow the relation  $\delta\varepsilon_2 = R\delta\varepsilon_1$ , in which  $R$  can be varied in different tests. In this simulation, four different  $R$  values are tested, as shown in Figure 4.11. Most of the specimens can approach the plastic surface (Mohr-Coulomb line in Figure 4.10) and continuously mount its stress to the critical state. As  $R$  decreases until  $R = -1.4$ , a liquefaction is observed. The specimen continuously loses its stress and seems hard to reach the plastic surface. This has also been encountered in Figure 4.11, when the loose specimen undergoes the undrained biaxial test. The ability of the micro-directional model and H-directional model to characterize the liquefaction has been proved (Nicot and Darve, 2006, 2011b). As expected, this ability has been inherited by the modified H-directional model.

Based on these results, it seems that the stress and the volumetric behavior of the modified H-directional model are satisfying. In this model, the value of the initial confining pressure and the inter-particle friction can basically and sensitively control the corresponding macroscopic behavior of the material. And reversely, macroscopic

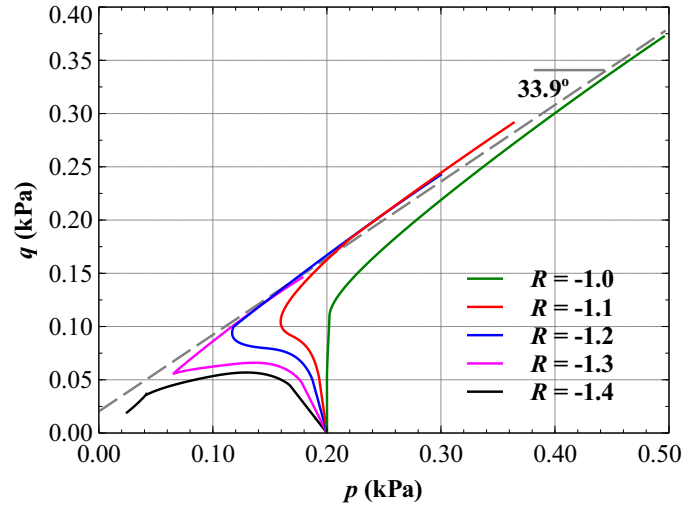


**Figure 4.11:** The stress response of a specimen, when subjected to proportional loading path with different  $R$  ( $\varepsilon_2 = R\delta\varepsilon_1$ ). The gray dashed line is the Mohr-Coulomb surface drawn by drained biaxial tests.  $\phi_g = 30^\circ$ ,  $e_0(\vec{n}) = 0.55$  and  $p_0 = 200\text{kPa}$ .

behavior can be understandably associated with corresponding microscopic parameters. The sensitivity of the granular material to the density is able to be correctly characterized. However, using this model, there can be a realistic simulation on the material's liquefaction.

### 4.2.3 Prospectives on improving the H-directional model

A promising direction for improving the H-directional model is to bring other kinds of loop different from hexagons into the system. In chapter 3, two sets of loop were shown to play a striking role in terms of the force transmission and volumetric evolution. They are  $L_{6+}$  and  $L_3$ .  $L_{6+}$  has a large size and flexible shape, and is often associated to the volumetric behavior of the granular material. Comparably,  $L_3$ , the firmest kind of loop, plays an indispensable role in the force transmission, while it efficiently controls the movability of the force-chains. The interplay between  $L_{6+}$  and  $L_3$  largely governs the diversity of mechanical behaviors of the granular material. To this extent, a multi-scale constitutive model, which is more competent for simulating the granular material, should encompass more mechanical features of these two sets of loop. In the H-directional model and its modified version, the hexagon is built as an embodiment of  $L_{6+}$  and is even positioned at a fundamental place in constructing material's fabric. However, a structure resembling  $L_3$  is excluded. Thus, the future work for improving the model should emphasize on adding a triangle pattern.

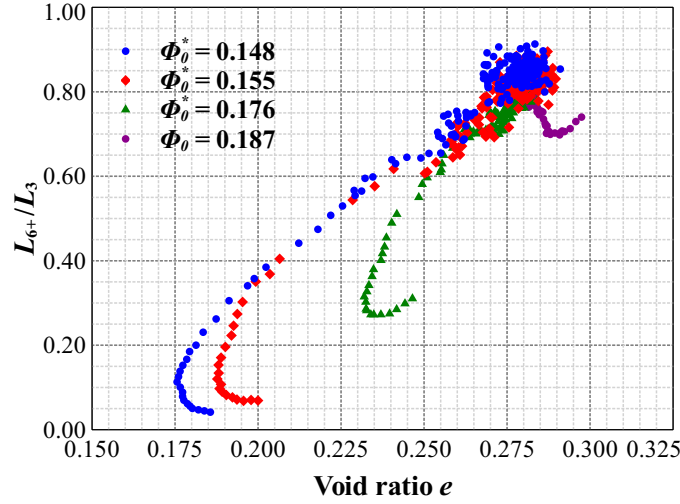


**Figure 4.12:** The evolution of the ratio of the number of the  $L_{6+}$  over  $L_3$  in terms of the void ratio  $e$  in the shear band area of S1, S2 and S3 and in the whole area of S4

The most difficult part may not be to give the local constitutive relation of the triangle pattern, since it has much less degree of freedom than the hexagon. The real challenge would be (1) the proportion between  $L_{6+}$  and  $L_3$  in each direction, and (2) how this proportion evolves during loading.

In order to consider the “hexagon - triangle” proportion in the model, a framework can be embedded into the stress averaging procedure. Two parameters,  $\omega(\theta)$  and  $R_{HT}$ , are respectively the directional distribution of all loop kinds and the ratio the hexagon over the triangle (assuming that  $R_{HT}$  is independent from  $\theta$ ). Provided that  $\bar{\bar{\sigma}}_T(\theta)$  and  $\bar{\bar{\sigma}}_H(\theta)$  are loop tensors respectively for the triangle and the hexagon in the local coordinate system  $\vec{n} - \vec{t}$ ,  $\bar{\bar{\sigma}}_H(\theta)$  has been formulated by equations 4.15.  $\bar{\bar{\sigma}}_T$ , the integration over all  $\bar{\bar{\sigma}}_T(\theta)$  along different orientations, can be obtained in the same way as  $\bar{\bar{\sigma}}_H$  be solved by equation 4.16,

$$\bar{\bar{\sigma}}_T = \frac{1}{V} \int \omega(\theta) \bar{\bar{P}}^{-1} \bar{\bar{\sigma}}_T(\theta) \bar{\bar{P}} d\theta, \quad (4.26)$$

where  $\bar{\bar{P}}$  is the transport matrix. Then the stress tensor can be finally built as following,

$$\bar{\bar{\sigma}} = \frac{1}{1 + R_{HT}} (\bar{\bar{\sigma}}_T + R_{HT} \bar{\bar{\sigma}}_H). \quad (4.27)$$

So far, all problems converge to how  $R_{HT}$  can be solved according to the mechanical state. The investigation in section 3.3 reveals the strong relation between the plastic volumetric strain and the evolution of  $L_3$  and  $L_{6+}$ . This provides a promising way of solving  $R_{HT}$  from time to time by attaching it to the volumetric strain. But before we used to build the constitutive model, the relation between  $R_{HT}$  and the volumetric strain (total or plastic) should be characterized more quantitatively.

Following the results in the section 3.5, evolutions of the ratio of the number of the  $L_{6+}$  over  $L_3$  ( $R_{63}$ ) are shown in terms of the void ratio  $e$  in the shear band area of  $S1$ ,  $S2$  and  $S3$  and in the whole area of  $S4$ . The  $R_{63}/e$  in all cases converges to around a same value. This indicates a critical state relation between  $R_{63}$  and  $e$ . Therefore, the critical state value of  $R_{HT}$  can be given according to the global void ratio or the volumetric strain. However, whether the critical state value of  $R_{63}/e$  keeps stationary in various hydrostatic pressure  $p$  is unclear. If it does, how does it evolve? These problems deserve further investigations.

Another direction of developing the H-directional model is to extend it into a 3D form. This comes from an application end, to embed the model into 3D numerical tools, such as FEM codes. One more dimension is waiting to be involved, however, there are much more things to do than just transferring the elementary body from the plane to the 3D space. Two questions should be asked ahead of the modification: what kinds of shape are representative enough of the reality so as to be employed as the basic element; How does these kinds evolve along loading path. Any answer can be only given on the basis of the knowledge on the micro-structure characteristics of 3D granular assemblies.

## 4.3 Conclusion

There are two sides to be considered in the constitutive modeling of the granular materials using a multi-scale approach. Firstly, the constitutive relation of macroscopic behaviors should be properly related to their microscopic essences, alternatively saying, the local behaviors on the contact scale, from which the macroscopic behavior derives. The more properly this point is achieved, the closer to reality the constitutive model's performance will be. Another concern is to decrease the computational complexity as much as possible with reasonable assumptions, in order to avoid solving a exceeding number of local balance equations, given by all particles. To most cases, involving more mechanical details in the micro-scale and decreasing the computational complexity are paradoxical. In recent decades, many researchers explore between these two ends, trying

to find an optimized solution in favor of both two. However, an optimized solution can only be gained after an accurate and deep understanding on the microscopic behavior of the granular material. This chapter gives an example of the attempt to find this optimized solution.

A review on the micro-directional model is first given. In this 3D constitutive model using a multi-scale approach, the microscopic level of the material (the fabric) consists of individual contacts independent from each other and laying along different directions. As the incremental strain is affinely projected onto all individual contacts, incremental forces are simultaneously generated according to the local constitutive relation, namely, the contact law. Then the global stress can be obtained by integrating all contacts forces in the way given by Love formula. This model succeeds to relate the macro-scale properties to micro-scale ones by employing an assumed fabric. However, strong shortcoming has still been captured. As revealed in the micro-structure investigation in chapter 3, the global strain derives not only from the relative displacements between grains in contact, but also from contacts rearrangement. This unfortunately denies the strain localization scheme used in the micro-directional model: first, the total incremental strain cannot be simply localized; more significantly, contacts are far from independent from each other, but intimately cooperating with each other in terms of transmitting forces (force-chains) or defining voids (meso-loops), in other words, there is a self-organization of contacts.

Then the H-directional model is introduced, which replaces individual contacts by individual hexagonal elements. Also replaced is the local behavior from the contact law to the local constitutive relation of the hexagon, in which contacts are never independent but internally compatible with each other. However, the rotation (the shear deformation) cannot be validated in the H-directional model, due to its symmetrical layout. Both stress and strain cannot rotate from their original direction. This is not realistic, and strongly weakens both the ability of the model to cope with complex stress and strain loading paths and the adaptability to numerical methods, such as FEM.

A modified H-directional model is developed, in order to break the geometrical symmetry of the hexagon. The new model allows a rotation on the former symmetrical axis, while inducing three more variables to both local kinematics and statics. The ability of this new model is then testified under different loading paths. The results are quite satisfying, with reasons listed as follows: (1) both the evolution of stress and volumetric strain are quite reasonable; (2) microscopic parameters are observed to sensitively and correctly govern the corresponding macroscopic behavior of the specimen; (3) the liquefaction and other instability-related phenomena can be captured by this model.

Finally, perspectives for improving the H-directional model are discussed. The triangle is highlighted in chapter 3 as a significant kind of meso-loop in terms of both the force transmission and the volumetric evolution of the material. This gives rise to the necessity of involving a triangle element into the H-directional model. The triangle can be inserted to the stress averaging procedure, by giving a ratio between the population of the triangle and the hexagon. Finally an effort for extending the model into a 3D form is also highly recommended.



# Chapter 5

## General Conclusion

### 5.1 Conclusion

The basic line of reasoning of this manuscript is that (1) on the basis of the DEM simulation, to investigate the micro-structure's evolutionary characteristics of the granular material; and (2) taking the advantage of the knowledge from micro-structure investigation, using multi-scale approach technique, to develop the constitutive model for granular material.

Along this line, several 2D numerical biaxial tests using DEM have been performed. A series of micro-structure investigations are subsequently carried out. A meso-scale is highlighted in the research, as an intermediate scale between the single contact scale, in which contacts are considered independently from each other, and the macro-scale, a scale large enough to be treated as a homogeneous material point. Scoping in this scale enable us to capture diverse topological and mechanical features of the granular material. Two mesoscopic organizations fundamental for material's mechanical behavior are stressed in the investigation. One is the force-chains, column-like structures, formed by contacts linking head to end in a quasi-linear shape, carrying far more forces than their surrounding domain, and, consequently, in charge of the force transmission of the material. Another is the meso-loops, loop-like structures, consisting of contacts linking each other to form a closed loop, by which the whole material area can be seamlessly tessellated. Meso-loops are categorized according to their side number. Three aspects of interest have been investigated in this manuscript: (1) the way of meso-loops evolving

along biaxial loading path, and how they are related to the material's volumetric behavior; (2) the pattern in which force-chains interact with meso-loops, and the role this interaction plays in global volumetric evolution and material instability; and (3) whether there exists featured critical state meso-structures, and the extent of these meso-structures.

Principal results in the micro-structure analysis are summarized:

1. When the evolution of proportions of different kinds of meso-loop was plotted, it was found that  $L_3$  and  $L_{6+}$  were two most active groups in terms of population variation. Their proportions,  $\omega_3$  and  $\omega_{6+}$ , evolved oppositely, showing a highly negative evolutionary correlation. Furthermore, in dense and intermediate specimens, with a continuous conversion from  $L_3$  (firm and dense structure) to  $L_{6+}$  (flexible and loose structure), the material consistently lost its strength and, meanwhile, increased its volume. To this degree, meso-loops can be the link between the stress and volumetric behavior of the granular material.

The total and average areas of different kinds of loop ( $A_i$  and  $\bar{A}_i$  respectively) were also investigated in this section. According to the result of  $\bar{A}_i$  evolution,  $L_{6+}$  was the only kind of loop geometrically sensitive to the external loading. Meanwhile, evolution of  $a_i$  in dense and intermediate specimens showed that only  $L_{6+}$  presented a volume increase during the loading path while the other kinds of loop contracted. The significance of  $L_{6+}$  was highlighted;  $L_{6+}$  exerted the strongest influence on global volumetric variation and was the only contributor to the dilatancy of dense and intermediate specimens.

The evolution on the proportions of different kinds of meso-loop belongs to the plastic deformation, which can not rebound during unloading. Correspondingly, what is recoverable, belonging to the elastic deformation, is due to inter-particle penetrations. The contractancy at the early stage of drained biaxial tests in dense and intermediate specimens is attributed to the elastic penetrations among particles, disregarding the dilatant trend indicated by a consistently significant conversion from  $L_3$  to  $L_{6+}$ . Following that, we had also verified that particle elastic parameters could impose a strong effect on the contractant behavior of dense granular material.

2. On the basis of the *DEM* simulations of the drained biaxial test, the granular assembly was separated into two parts: loops connected to force-chain (*FCL*) and loops far from force-chain (*NFCL*). When the evolution of *FCL* was compared with that in *NFCL* area, it was found that under the effect of force-chains, the material was structurized into two differently featured phases with distinct meso-structure

and density. The *FCL* area contained a prominently larger proportion of  $L_3$  and a smaller proportion of  $L_{6+}$  than the *NFCL* area did. Meanwhile, the *FCL* area was observed to have a constantly higher void ratio  $e$  than remaining area. Force-chain area can be seen as the main source and the primary contributor to the global dilatancy.

The evolutionary status of meso-loops, as a result of the fabric variation, also retro-acted to the stability of the force-chain. The existence of  $L_3$  proved to improve force-chains' stability, whereas  $L_{6+}$  exacerbated force-chains in terms of the stability. Consequently, the life-cycle of the force-chain can be displayed as a history of it interacting with its confining meso-loops.

Moreover,  $L_{6+}^{FCL}$  was observed to be more anisotropically stressed than other categories, while  $L_3^{FCL}$  was the most isotropic one. This eventually gains two conclusions: (1) according to the initial fabrics, the loading path will direct dilatancy or contractancy; and (2) the stability of force-chains varies in accordance with the evolution of meso-structures, and the latter follows the global volumetric change.

3. The critical state fabric of granular material was investigated in localized and diffuse failure modes from a mesoscopic viewpoint. Except with different initial void ratio  $e_0$ , all specimens were attributed to the same parameters and subjected to the same loading path. Specimens undergoing a localized failure were divided into two sub-domains: the shear band area and the outside shear band area.

The evolution of meso-structures were measured and compared respectively in three domains of specimens: the shear band area and outside shear band area of localized failure specimen and the whole area of diffuse failure specimen, where the first and the third are the failure areas. Both the meso-scale topologies characterized by meso-loops and the void ratios were found to converge in the critical state in the failure areas of all specimens. Meanwhile, a similar force-chain evolution pattern was also captured in the failure areas. All these results pointed to a conclusion: in failure area, there exists an identical critical state meso-structure, only from which does the material's critical state derives.

When the force-chain age composition were investigated in the critical state, it is revealed that force-chains built in early steps of the test showed a prominent vitality in granular material. This means that in drained biaxial tests, force-chains are continuously losing their durabilities and sustainabilities with the evolutionary fabric on which they are located. Otherwise, most newly created force-chains

in specimens were found to locate inside the shear band, but these young age force-chains died out quickly. It is concluded that while the material evolves into the critical state, there are only old, robust force-chains, mainly located outside shear band, and young, fleeting force-chains, mainly located inside shear band.

With the knowledge obtained from the micro-structure investigations, a 2D constitutive model, using multi-scale approach, was developed in modification from the H-directional model, proposed by [Nicot and Darve \(2011b\)](#). The developing history of two predecessors of this modified model, micro-directional model and H-directional model, was firstly reviewed. The strain localization procedure was emphasized, which differs among models according to distinct assumptions, bringing in various drawbacks and limitations. In the micro-directional model, contacts are assumed to be independently from each other and to deform affinely following the global strain. H-directional model advanced in the sense of being able to consider the inter-contact rearrangement in the model, by employing a meso-loop, the hexagon, as its fabric element. On the heritage of the merits from H-directional model, the modified H-directional model further broke the assumed axis-symmetry on the configuration of the hexagonal element. A rotation was allowed on the former symmetrical axis, inducing three more variables to both local kinematics and statics. The evolution of local variables of this modified model was traced and analyzed along a drained biaxial loading path. The development of several important local variables was quite reasonable and can be linked to global mechanical responses. The ability of this new model was also testified under different loading paths. The results were quite satisfying, with reasons listed as follows: (1) both the evolution of stress and volumetric strain were quite reasonable; (2) microscopic parameters was observed to be able to sensitively and correctly influence corresponding macroscopic behaviors of the specimen; (3) the liquefaction and other instability-related phenomena can be simulated by this model.

## 5.2 Open issues and perspectives

To better understand and simulate the mechanical behaviors of granular materials, it is necessary to have an insight in the fabric development on the meso-scale. However, there are still many works to do.

**The investigation on meso-structures**

In terms of the meso-structure investigation, several questions can be interesting and need to be addressed: (1) how meso-structures can be defined and identified in 3D granular assemblies, and how they evolve along loading path? (2) how the meso-structures distribute and evolve along loading paths other than the drained biaxial one? (3) what is the relation between the spatial distribution of the meso-structures and the strain localization; (4) how the mutual evolution between force-chains and meso-loops leads to the material instability? and (5) what is the mechanism of the force-chains intervening their surrounding meso-loops?

**The multi-scale approach constitutive modeling**

The fundamental role of force-chains to the mechanical properties of granular materials was confirmed by this thesis and previous studies. An element or a mechanism resembling force-chain's behavior should be incorporated in the constitutive model using the multi-scale approach.

In terms of improving the H-directional model, the triangle was highlighted in chapter 3 as a significant kind of meso-loop in aspects of both the force transmission and the volumetric evolution of the material. This gives rise to the necessity of involving a triangle element into the H-directional model. As discussed at the end of chapter 4 (the subsection 4.2.3), the triangle can be inserted to the stress averaging procedure, by giving a ratio between the population of the triangle and the hexagon. However, the evolutionary relation between the triangle and hexagon elements can be only given on the basis of the further investigation on the meso-structures of granular materials. Otherwise, a work of extending the model into a 3D form is also highly recommended.



# Bibliography

- K. A. Alshibli and S. Sture. Shear band formation in plane strain experiments of sand. *Journal of Geotechnical and Geoenvironmental Engineering*, 126(6):495–503, 2000.
- S. J. Antony. Evolution of force distribution in three-dimensional granular media. *Physical Review E*, 63(1):011302, 2000.
- R. Arévalo, I. Zuriguel, and D. Maza. Topology of the force network in the jamming transition of an isotropically compressed granular packing. *Physical Review E*, 81(4), Apr. 2010.
- D. Athanasiou-Grivas and M. E. Harr. Particle contacts in discrete materials. *Journal of Geotechnical and Geoenvironmental Engineering*, 106(ASCE 15433), 1980.
- E. Azéma, F. Radjai, R. Peyroux, and G. Saussine. Force transmission in a packing of pentagonal particles. *Physical Review E*, 76(1):011301, July 2007.
- Z. Bazant and others. Endochronic inelasticity and incremental plasticity. *International Journal of Solids and Structures*, 14(9):691–714, 1978.
- K. Bagi. On the definition of stress and strain in granular assemblies through the relation between micro-and macro-level characteristics. *Powders & grains*, 93:117–121, 1993.
- K. Bagi. Stress and strain in granular assemblies. *Mechanics of materials*, 22(3):165–177, 1996.
- J. P. Bardet. Observations on the effects of particle rotations on the failure of idealized granular materials. *Mechanics of materials*, 18(2):159–182, 1994.
- R. J. Bathurst and L. Rothenburg. Observations on stress-force-fabric relationships in idealized granular materials. *Mechanics of Materials*, 9(1):65–80, 1990.
- E. Battenberg and D. Wessel. Accelerating Non-Negative Matrix Factorization for Audio Source Separation on Multi-Core and Many-Core Architectures. In *ISMIR*, pages 501–506, 2009.
- K. Been and M. G. Jefferies. A state parameter for sands. *Geotechnique*, 35(2):99–112, 1985.

- R. Behringer, K. E. Daniels, T. S. Majmudar, and M. Sperl. Fluctuations, correlations and transitions in granular materials: statistical mechanics for a non-conventional system. *Philosophical Transactions of the Royal Society A: Mathematical, Physical and Engineering Sciences*, 366(1865): 493–504, Feb. 2008.
- D. Bigoni. *Bifurcation and instability of non-associative elastoplastic solids*. Springer, 2000.
- D. Bigoni and T. Hueckel. Uniqueness and localization—I. Associative and non-associative elastoplasticity. *International Journal of Solids and Structures*, 28(2):197–213, 1991.
- D. L. Blair, N. W. Mueggenburg, A. H. Marshall, H. M. Jaeger, and S. R. Nagel. Force distributions in three-dimensional granular assemblies: Effects of packing order and interparticle friction. *Physical Review E*, 63(4):041304, 2001.
- M. Bornert, N. Lenoir, P. BÉSUELLE, Y. Pannier, S. Hall, G. Viggiani, and J. Desrues. Discrete and continuum analysis of localised deformation in sand using X-ray CT and volumetric digital image correlation. *Géotechnique*, 60(5):315–322, Jan. 2010.
- B. Brogliato. *Nonsmooth mechanics: models, dynamics and control*. Springer Science & Business Media, 2012.
- B. Brogliato and V. Acary. Numerical methods for nonsmooth dynamical systems. *Lecture Notes in Applied and Computational Mechanics*, 35, 2008.
- F. Calvetti, G. Combe, and J. Lanier. Experimental micromechanical analysis of a 2d granular material: relation between structure evolution and loading path. *Mechanics of Cohesive-frictional Materials*, 2(2):121–163, 1997.
- B. Cambou. From global to local variables in granular materials. *Powders and grains*, 93:73–86, 1993.
- B. Cambou, P. Dubujet, F. Emeriault, and F. Sidoroff. Homogenization for granular materials. *European journal of mechanics. A. Solids*, 14(2):255–276, 1995.
- B. Cambou, M. Chaze, and F. Dedecker. Change of scale in granular materials. *European Journal of Mechanics-A/Solids*, 19(6):999–1014, 2000.
- B. Cambou, M. Jean, and F. Radjai, editors. *Micromechanics of granular materials*. ISTE ; Wiley, London : Hoboken, NJ, 2009.
- R. Chambon and D. Caillerie. Existence and uniqueness theorems for boundaryvalue problems involving incrementally non linear models. *International journal of solids and structures*, 36(33): 5089–5099, 1999.
- C. S. Chang. *Micromechanical modelling of constitutive relations for granular material*. 2014.

- C. S. Chang and A. Misra. Stress-strain behavior of sands-A microstructural approach. *Proceedings, Fourth International Symposium on Interaction of Non-Nuclear Ammunition with Structures, Panama City Beach, Florida*, pages 354–459, 1989.
- C. S. Chang, A. Misra, and S. S. Sundaram. Micromechanical modelling of cemented sands under low amplitude oscillations. *Geotechnique*, 40(2):251–263, 1990.
- C. S. Chang, Y. Chang, and M. G. Kabir. Micromechanics modeling for stress-strain behavior of granular soils. I: Theory. *Journal of geotechnical engineering*, 118(12):1959–1974, 1992.
- J. Christoffersen, M. M. Mehrabadi, and S. Nemat-Nasser. A micromechanical description of granular material behavior. *Journal of Applied Mechanics*, 48(2):339–344, 1981.
- P. A. Cundall. A computer model for simulating progressive, large-scale movements in blocky rock systems. 1971.
- P. A. Cundall and O. D. Strack. A discrete numerical model for granular assemblies. *Geotechnique*, 29(1):47–65, 1979.
- P. Dantu. Etude statistique des forces intergranulaires dans un milieu pulvérulent. *Géotechnique*, 18(1):50–55, 1968.
- F. Darve. The expression of rheological laws in incremental form and the main classes of constitutive equations. *Geomaterials: Constitutive Equations and Modelling*, pages 123–148, 1990.
- F. Darve and X. Roguiez. Homogeneous bifurcation in soils. *Adachi et al., editor, Localization and Bifurcation Theory for Soils and Rocks*, pages 43–50, 1998.
- F. Darve, E. Flavigny, and M. Meghachou. Constitutive modelling and instabilities of soil behaviour. *Computers and Geotechnics*, 17(2):203–224, 1995a.
- F. Darve, E. Flavigny, and M. Meghachou. Yield surfaces and principle of superposition: revisit through incrementally non-linear constitutive relations. *International Journal of Plasticity*, 11(8): 927–948, 1995b.
- F. Darve, G. Servant, F. Laouafa, and H. D. V. Khoa. Failure in geomaterials: continuous and discrete analyses. *Computer methods in applied mechanics and engineering*, 193(27):3057–3085, 2004.
- G. Debunne, M. Desbrun, M.-P. Cani, and A. H. Barr. Adaptive simulation of soft bodies in real-time. In *Computer Animation 2000*, pages 133–144, 2000.
- J. Desrues, R. Chambon, M. Mokni, and F. Mazerolle. Void ratio evolution inside shear bands in triaxial sand specimens studied by computed tomography. *Géotechnique*, 46(3):529–546, 1996.
- F. V. Donzé and S. A. Magnier. Spherical discrete element code. *Discrete element project report*, 2, 1997.

- A. Drescher and G. D. J. De Jong. Photoelastic verification of a mechanical model for the flow of a granular material. *Journal of the Mechanics and Physics of Solids*, 20(5):337–340, 1972.
- P. W. Drucker D. C. Soil Mechanics and Plastic Analysis or Limit Design. *Quarterly of applied mathematics*, 10(2):157–65, 1952.
- F. Emeriault and B. Cambou. Micromechanical modelling of anisotropic non-linear elasticity of granular medium. *International Journal of Solids and Structures*, 33(18):2591–2607, 1996.
- J. M. Erikson, N. W. Mueggenburg, H. M. Jaeger, and S. R. Nagel. Force distributions in three-dimensional compressible granular packs. *Physical Review E*, 66(4):040301, 2002.
- Y. T. Feng, K. Han, and D. R. J. Owen. Coupled lattice Boltzmann method and discrete element modelling of particle transport in turbulent fluid flows: Computational issues. *International Journal for Numerical Methods in Engineering*, 72(9):1111, 2007.
- Y. T. Feng, K. Han, and D. R. J. Owen. Combined three-dimensional lattice Boltzmann method and discrete element method for modelling fluid-particle interactions with experimental assessment. *International journal for numerical methods in engineering*, 81(2):229–245, 2010.
- Z.-G. Feng and E. E. Michaelides. The immersed boundary-lattice Boltzmann method for solving fluid-particles interaction problems. *Journal of Computational Physics*, 195(2):602–628, 2004.
- P. Fu and Y. F. Dafalias. Fabric evolution within shear bands of granular materials and its relation to critical state theory. *International Journal for Numerical and Analytical Methods in Geomechanics*, 35(18):1918–1948, Dec. 2011.
- Z. Gao and J. Zhao. Constitutive modeling of artificially cemented sand by considering fabric anisotropy. *Computers and Geotechnics*, 41:57–69, 2012.
- Z. Gao, J. Zhao, X.-S. Li, and Y. F. Dafalias. A critical state sand plasticity model accounting for fabric evolution: SAND MODEL ACCOUNTING FOR FABRIC EVOLUTION. *International Journal for Numerical and Analytical Methods in Geomechanics*, 38(4):370–390, Mar. 2014.
- X. Gu, M. Huang, and J. Qian. Discrete element modeling of shear band in granular materials. *Theoretical and Applied Fracture Mechanics*, 72:37–49, Aug. 2014.
- N. Guo and J. Zhao. The signature of shear-induced anisotropy in granular media. *Computers and Geotechnics*, 47:1–15, 2013.
- M. Hajime. A microscopic study on shear mechanism of granular materials. *Soils and Foundations*, 14(1):29–43, 1974.
- A. Hasan and K. Alshibli. Three dimensional fabric evolution of sheared sand. *Granular Matter*, 14(4):469–482, 2012.

- W. B. Heard. *Rigid body mechanics: mathematics, physics and applications*. John Wiley & Sons, 2008.
- R. Hill. A general theory of uniqueness and stability in elastic-plastic solids. *Journal of the Mechanics and Physics of Solids*, 6(3):236–249, 1958.
- R. Hill. Elastic properties of reinforced solids: some theoretical principles. *Journal of the Mechanics and Physics of Solids*, 11(5):357–372, 1963.
- R. Hill. On the classical constitutive relations for elastic/plastic solids. *Recent progress in applied mechanics*, 241, 1967.
- D. Howell, R. P. Behringer, and C. Veje. Stress fluctuations in a 2d granular Couette experiment: a continuous transition. *Physical Review Letters*, 82(26):5241, 1999.
- P. M. Hubbard. Approximating polyhedra with spheres for time-critical collision detection. *ACM Transactions on Graphics (TOG)*, 15(3):179–210, 1996.
- U. Itasca and U. D. E. Code. *Version 5.0*. Itasca Consulting Group, Inc., Minneapolis, 2011.
- K. Iwashita and M. Oda. Micro-deformation mechanism of shear banding process based on modified distinct element method. *Powder Technology*, 109(1-3):192–205, Apr. 2000.
- H. M. Jaeger, S. R. Nagel, and R. P. Behringer. Granular solids, liquids, and gases. *Reviews of Modern Physics*, 68(4):1259, 1996.
- M. Jean. The non-smooth contact dynamics method. *Computer methods in applied mechanics and engineering*, 177(3):235–257, 1999.
- A. F. Johnson and M. Holzapfel. Modelling soft body impact on composite structures. *Composite Structures*, 61(1):103–113, 2003.
- D. Jung and K. K. Gupta. Octree-based hierarchical distance maps for collision detection. In *Robotics and Automation, 1996. Proceedings., 1996 IEEE International Conference on*, volume 1, pages 454–459. IEEE, 1996.
- K. D. Kafui, C. Thornton, and M. J. Adams. Discrete particle-continuum fluid modelling of gas-solid fluidised beds. *Chemical Engineering Science*, 57(13):2395–2410, 2002.
- T. Kawaguchi, T. Tanaka, and Y. Tsuji. Numerical simulation of two-dimensional fluidized beds using the discrete element method (comparison between the two- and three-dimensional models). *Powder technology*, 96(2):129–138, 1998.
- K. Ken-Ichi. Distribution of directional data and fabric tensors. *International Journal of Engineering Science*, 22(2):149–164, 1984.

- J. T. Klosowski, M. Held, J. S. Mitchell, H. Sowizral, and K. Zikan. Efficient collision detection using bounding volume hierarchies of k-DOPs. *Visualization and Computer Graphics, IEEE Transactions on*, 4(1):21–36, 1998.
- D. Kolymbas. An outline of hypoplasticity. *Archive of applied mechanics*, 61(3):143–151, 1991.
- L. Kondic, A. Goulet, C. S. O’Hern, M. Kramar, K. Mischaikow, and R. P. Behringer. Topology of force networks in compressed granular media. *EPL (Europhysics Letters)*, 97(5):54001, 2012.
- J. Kozicki and F. V. Donzé. A new open-source software developed for numerical simulations using discrete modeling methods. *Computer Methods in Applied Mechanics and Engineering*, 197(49):4429–4443, 2008.
- J. Kozicki and F. V. Donzé. Yade-open dem: an open-source software using a discrete element method to simulate granular material. *Engineering Computations*, 26(7):786–805, 2009.
- N. P. Kruyt. Statics and kinematics of discrete Cosserat-type granular materials. *International Journal of Solids and Structures*, 40(3):511–534, Feb. 2003.
- N. P. Kruyt and L. Rothenburg. Micromechanical definition of the strain tensor for granular materials. *Journal of applied mechanics*, 63(3):706–711, 1996.
- N. P. Kruyt and L. Rothenburg. Statistics of the elastic behaviour of granular materials. *International Journal of Solids and Structures*, 38(28):4879–4899, 2001.
- N. P. Kruyt and L. Rothenburg. On micromechanical characteristics of the critical state of two-dimensional granular materials. *Acta Mechanica*, 225(8):2301–2318, 2014.
- M. R. Kuhn. Structured deformation in granular materials. *Mechanics of materials*, 31(6):407–429, 1999.
- A. J. Ladd. Numerical simulations of particulate suspensions via a discretized Boltzmann equation. Part 1. Theoretical foundation. *Journal of Fluid Mechanics*, 271:285–309, 1994a.
- A. J. Ladd. Numerical simulations of particulate suspensions via a discretized Boltzmann equation. Part 2. Numerical results. *Journal of Fluid Mechanics*, 271:311–339, 1994b.
- A. J. C. Ladd and R. Verberg. Lattice-Boltzmann simulations of particle-fluid suspensions. *Journal of Statistical Physics*, 104(5-6):1191–1251, 2001.
- C. R. Leonardi, D. R. J. Owen, and Y. T. Feng. Simulation of fines migration using a non-Newtonian lattice Boltzmann-discrete element model: Part I: 2d implementation aspects. *Engineering Computations*, 29(4):366–391, 2012a.
- C. R. Leonardi, D. R. J. Owen, and Y. T. Feng. Simulation of fines migration using a non-Newtonian lattice Boltzmann-discrete element model: Part II: 3d extension and applications. *Engineering Computations*, 29(4):392–418, 2012b.

- X. S. Li and Y. F. Dafalias. Anisotropic Critical State Theory: Role of Fabric. *Journal of Engineering Mechanics*, 138(3):263–275, Mar. 2012.
- C.-L. Liao, T.-P. Chang, D.-H. Young, and C. S. Chang. Stress-strain relationship for granular materials based on the hypothesis of best fit. *International Journal of Solids and Structures*, 34(31):4087–4100, 1997.
- A. E. H. Love. *A treatise on the mathematical theory of elasticity*, volume 1. Cambridge University Press, 2013.
- O. Mahabadi, P. Kaifosh, P. Marschall, and T. Vietor. Three-dimensional FDEM numerical simulation of failure processes observed in Opalinus Clay laboratory samples. *Journal of Rock Mechanics and Geotechnical Engineering*, 6(6):591–606, Dec. 2014.
- O. K. Mahabadi, A. Lisjak, A. Munjiza, and G. Grasselli. Y-Geo: New combined finite-discrete element numerical code for geomechanical applications. *International Journal of Geomechanics*, 2012.
- T. S. Majmudar and R. P. Behringer. Contact force measurements and stress-induced anisotropy in granular materials. *Nature*, 435(7045):1079–1082, 2005.
- M. M. Mehrabadi, S. Nemat-Nasser, and M. Oda. On statistical description of stress and fabric in granular materials. *International Journal for Numerical and Analytical Methods in Geomechanics*, 6(1):95–108, 1982.
- V. Šmilauer and B. Chareyre. Yade dem formulation. *Yade Documentation*, 2010.
- V. Šmilauer, E. Catalano, B. Chareyre, S. Dorofeenko, J. Duriez, A. Gladky, J. Kozicki, C. Modenese, L. Scholtès, L. Sibille, and others. Yade documentation. *The Yade Project*. (<http://yade-dem.org/doc/>), 2010a.
- V. Šmilauer, E. Catalano, B. Chareyre, S. Dorofeenko, J. Duriez, A. Gladky, J. Kozicki, C. Modenese, L. Scholtès, L. Sibille, and others. Yade reference documentation. *Yade Documentation*, 474, 2010b.
- I. Miller, J. E. Freund, and R. A. Johnson. *Probability and statistics for engineers*, volume 1110. Prentice-Hall Englewood Cliffs, NJ, 1965.
- N. W. Mueggenburg, H. M. Jaeger, and S. R. Nagel. Stress transmission through three-dimensional ordered granular arrays. *Physical Review E*, 66(3):031304, 2002.
- D. M. Mueth, H. M. Jaeger, and S. R. Nagel. Force distribution in a granular medium. *Physical Review E*, 57(3):3164–3169, Mar. 1998.
- D. M. Mueth, G. F. Debregeas, G. S. Karczmar, P. J. Eng, S. R. Nagel, and H. M. Jaeger. Signatures of granular microstructure in dense shear flows. *Nature*, 406(6794):385–389, July 2000.

- A. Munjiza and K. R. F. Andrews. NBS contact detection algorithm for bodies of similar size. *International Journal for Numerical Methods in Engineering*, 43(1):131–149, 1998.
- A. Munjiza and P. W. Cleary. Industrial particle flow modelling using discrete element method. *Engineering Computations*, 26(6):698–743, 2009.
- M. Muthuswamy and A. Tordesillas. How do interparticle contact friction, packing density and degree of polydispersity affect force propagation in particulate assemblies? *Journal of Statistical Mechanics: Theory and Experiment*, 2006(09):P09003, 2006.
- N.-S. Nguyen, H. Magoaric, B. Cambou, and A. Danescu. Analysis of structure and strain at the meso-scale in 2d granular materials. *International Journal of Solids and Structures*, 46(17):3257–3271, 2009.
- N.-S. Nguyen, H. Magoaric, and B. Cambou. Local stress analysis in granular materials at a mesoscale. *International Journal for Numerical and Analytical Methods in Geomechanics*, 36(14):1609–1635, 2012.
- F. Nicot. Constitutive modelling of a snow cover with a change in scale. *European Journal of Mechanics-A/Solids*, 22(3):325–340, 2003.
- F. Nicot. From constitutive modelling of a snow cover to the design of flexible protective structures Part I: Mechanical modelling. *International Journal of Solids and Structures*, 41(11):3317–3337, 2004.
- F. Nicot and F. Darve. Micro-mechanical investigation of material instability in granular assemblies. *International journal of solids and structures*, 43(11):3569–3595, 2006.
- F. Nicot and F. Darve. Diffuse and localized failure modes: Two competing mechanisms. *International Journal for Numerical and Analytical Methods in Geomechanics*, 35(5):586–601, Apr. 2011a.
- F. Nicot and F. Darve. The H-microdirectional model: accounting for a mesoscopic scale. *Mechanics of Materials*, 43(12):918–929, 2011b.
- F. Nicot, F. Darve, and R. Group. A multi-scale approach to granular materials. *Mechanics of materials*, 37(9):980–1006, 2005.
- F. Nicot, L. Sibille, and F. Darve. Bifurcation in granular materials: An attempt for a unified framework. *International Journal of Solids and Structures*, 46(22-23):3938–3947, Nov. 2009.
- F. Nicot, N. Hadda, M. Guessasma, J. Fortin, and O. Millet. On the definition of the stress tensor in granular media. *International Journal of Solids and Structures*, 50(14):2508–2517, 2013.
- D. Nishiura and H. Sakaguchi. Parallel-vector algorithms for particle simulations on shared-memory multiprocessors. *Journal of Computational Physics*, 230(5):1923–1938, 2011.

- M. Oda. Deformation Mechanism of Sand in Triaxial Compression Tests. *Soils and Foundations*, 12(4):45–63, 1972a.
- M. Oda. Initial Fabrics and Their Relations to Mechanical Properties of Granular Material. *Soils and Foundations*, 12(1):17–36, 1972b.
- M. Oda. The Mechanism of Fabric Changes During Compressional Deformation of Sand. *Soils and Foundations*, 12(2):1–18, 1972c.
- M. Oda. A micro-deformation model for dilatancy of granular materials. In *Mechanics of Deformation and Flow of Particulate Materials*, pages 24–37. ASCE, 1997.
- M. Oda and K. Iwashita. Study on couple stress and shear band development in granular media based on numerical simulation analyses. *International Journal of Engineering Science*, 38(15):1713–1740, Oct. 2000.
- M. Oda and H. Kazama. Microstructure of shear bands and its relation to the mechanisms of dilatancy and failure of dense granular soils. *Geotechnique*, 48(4):465–481, 1998.
- M. Oda, J. Konishi, and S. Nemat-Nasser. Some experimentally based fundamental results on the mechanical behaviour of granular materials. *Geotechnique*, 30(4):479–495, 1980.
- M. Oda, J. Konishi, and S. Nemat-Nasser. Experimental micromechanical evaluation of strength of granular materials: effects of particle rolling. *Mechanics of materials*, 1(4):269–283, 1982.
- M. Ostoja-Starzewski. *Microstructural randomness and scaling in mechanics of materials*. CRC Press, 2007.
- H. Ouadfel and L. Rothenburg. Stress–force–fabric relationship for assemblies of ellipsoids. *Mechanics of Materials*, 33(4):201–221, 2001.
- K. Pearson. Note on regression and inheritance in the case of two parents. *Proceedings of the Royal Society of London*, pages 240–242, 1895.
- J. F. Peters, M. Muthuswamy, J. Wibowo, and A. Tordesillas. Characterization of force chains in granular material. *Physical Review E*, 72(4), Oct. 2005.
- H. Petryk. Material instability and strain-rate discontinuities in incrementally nonlinear continua. *Journal of the Mechanics and Physics of Solids*, 40(6):1227–1250, 1992.
- H. Petryk. *Theory of bifurcation and instability in time-independent plasticity*. Springer, 1993.
- H. D. R. D. Mindlin. Elastic Spheres in Contact Under Varying Oblique Forces. *Journal of Applied Mechanics*, 20, 1953.
- F. Radjai and S. Roux. Friction-induced self-organization of a one-dimensional array of particles. *Physical Review E*, 51(6):6177, 1995.

- F. Radjai, M. Jean, J.-J. Moreau, and S. Roux. Force Distributions in Dense Two-Dimensional Granular Systems. *Physical Review Letters*, 77(2):274–277, July 1996.
- F. Radjai, D. E. Wolf, M. Jean, and J.-J. Moreau. Bimodal character of stress transmission in granular packings. *Physical review letters*, 80(1):61, 1998.
- F. Radjai, S. Roux, and J. J. Moreau. Contact forces in a granular packing. *Chaos: An Interdisciplinary Journal of Nonlinear Science*, 9(3):544–550, 1999.
- F. Radjai, H. Troadec, and S. Roux. Key features of granular plasticity. *Granular materials: fundamentals and applications*, pages 157–184, 2004.
- M. J. Rhodes. Principles of powder technology. 1990.
- J. R. Rice. On the structure of stress-strain relations for time-dependent plastic deformation in metals. *Journal of applied mechanics*, 37(3):728–737, 1970.
- J. R. Rice. Continuum mechanics and thermodynamics of plasticity in relation to microscale deformation mechanisms. *Constitutive Equations in Plasticity*. Massachusetts Institute of Technology Press, Cambridge. 1975, 23-79, 1975.
- J. R. Rice. *The localization of plastic deformation*. Division of Engineering, Brown University, 1976.
- K. Roscoe and J. B. Purland. On the generalized stress-strain behaviour of wet clay. 1968.
- K. H. Roscoe, A. Schofield, and C. P. Wroth. On the yielding of soils. *Geotechnique*, 8(1):22–53, 1958.
- L. Rothenburg and R. J. Bathurst. Analytical study of induced anisotropy in idealized granular materials. *Géotechnique*, 39(4):601–614, Jan. 1989.
- K. SAS. Une nouvelle approche de l’homogénéisation des milieux granulaires. In *Symposium Saint-Venant*, pages 597–603, 1997.
- M. Satake. Fabric tensor in granular materials. In *Proc., IUTAM Symp. on Deformation and Failure of Granular materials, Delft, The Netherlands*, 1982.
- M. Satake. A discrete-mechanical approach to granular materials. *International journal of engineering science*, 30(10):1525–1533, 1992.
- A. Schofield and P. Wroth. Critical state soil mechanics. 1968.
- Y. Shigeto and M. Sakai. Parallel computing of discrete element method on multi-core processors. *Particuology*, 9(4):398–405, 2011.
- L. E. Silbert, G. S. Grest, and J. W. Landry. Statistics of the contact network in frictional and frictionless granular packings. *Physical Review E*, 66(6):061303, 2002.

- R. Smith. *Atomic and ion collisions in solids and at surfaces: theory, simulation and applications*. Cambridge University Press, 2005.
- A. J. M. Spencer. Isotropic polynomial invariants and tensor functions. In *Applications of tensor functions in solid mechanics*, pages 141–169. Springer, 1987.
- W. B. Streett, D. J. Tildesley, and G. Saville. Multiple time-step methods in molecular dynamics. *Molecular Physics*, 35(3):639–648, 1978.
- J. Tejchman and J. Górski. Deterministic and statistical size effect during shearing of granular layer within a micro-polar hypoplasticity. *International journal for numerical and analytical methods in geomechanics*, 32(1):81–107, 2008.
- C. Thornton and S. J. Antony. Quasi-static deformation of particulate media. *Philosophical transactions-royal society of London series a mathematical physical and engineering sciences*, pages 2763–2782, 1998.
- C. Thornton and D. J. Barnes. Computer simulated deformation of compact granular assemblies. *Acta Mechanica*, 64(1-2):45–61, 1986.
- A. Tordesillas. Force chain buckling, unjamming transitions and shear banding in dense granular assemblies. *Philosophical Magazine*, 87(32):4987–5016, 2007.
- A. Tordesillas, D. M. Walker, and Q. Lin. Force cycles and force chains. *Physical Review E*, 81(1), Jan. 2010.
- A. Tordesillas, C. A. H. Steer, and D. M. Walker. Force chain and contact cycle evolution in a dense granular material under shallow penetration. *Nonlinear Processes in Geophysics*, 21(2): 505–519, Apr. 2014.
- Y. Tsuji, T. Kawaguchi, and T. Tanaka. Discrete particle simulation of two-dimensional fluidized bed. *Powder technology*, 77(1):79–87, 1993.
- M. Tuckerman, B. J. Berne, and G. J. Martyna. Reversible multiple time scale molecular dynamics. *The Journal of chemical physics*, 97(3):1990–2001, 1992.
- I. Vardoulakis and J. Sulem. *Bifurcation analysis in geomechanics*. Chapman & Hall. London, 1995.
- I. Vardoulakis, M. Goldscheider, and G. Gudehus. Formation of shear bands in sand bodies as a bifurcation problem. *International Journal for numerical and analytical methods in Geomechanics*, 2 (2):99–128, 1978.
- R. Wan, M. Pinheiro, A. Daouadji, M. Jrad, and F. Darve. Diffuse instabilities with transition to localization in loose granular materials: diffuse instabilities with transition to localization. *International Journal for Numerical and Analytical Methods in Geomechanics*, 37(10):1292–1311, July 2013.

- R. G. Wan, M. Pinheiro, and P. J. Guo. Elastoplastic modelling of diffuse instability response of geomaterials. *International Journal for Numerical and Analytical Methods in Geomechanics*, 35(2): 140–160, Feb. 2011.
- T. Washizawa and Y. Nakahara. Parallel Computing of Discrete Element Method on GPU. *arXiv preprint arXiv:1301.1714*, 2013.
- X. T. Wei-Xin Ren. Nonlinear analysis of plane frames using rigid body-spring discrete element method. *Computers & Structures - COMPUT STRUCT*, 71(1):105–119, 1999.
- B. H. Xu and A. B. Yu. Numerical simulation of the gas-solid flow in a fluidized bed by combining discrete particle method with computational fluid dynamics. *Chemical Engineering Science*, 52(16):2785–2809, 1997.
- M. Xu, F. Chen, X. Liu, W. Ge, and J. Li. Discrete particle simulation of gas-solid two-phase flows with multi-scale CPU-GPU hybrid computation. *Chemical Engineering Journal*, 207:746–757, 2012.
- Z.-Y. Yin, C. S. Chang, M. Karstunen, and P.-Y. Hicher. An anisotropic elastic-viscoplastic model for soft clays. *International Journal of Solids and Structures*, 47(5):665–677, 2010.
- Z.-Y. Yin, M. Hattab, and P.-Y. Hicher. Multiscale modeling of a sensitive marine clay. *International Journal for Numerical and Analytical Methods in Geomechanics*, 35(15):1682–1702, 2011a.
- Z.-Y. Yin, M. Karstunen, C. S. Chang, M. Koskinen, and M. Lojander. Modeling time-dependent behavior of soft sensitive clay. *Journal of geotechnical and geoenvironmental engineering*, 137(11): 1103–1113, 2011b.
- J. Zhang, T. Majmudar, and R. Behringer. Force chains in a two-dimensional granular pure shear experiment. *Chaos*, 18(4):41107, 2008.
- J. Zhao and N. Guo. Unique critical state characteristics in granular media considering fabric anisotropy. *Géotechnique*, 63(8):695–704, 2013.
- H. Zhu, F. Nicot, and F. Darve. Meso-structure evolution in a 2d granular material during biaxial loading. *Granular Matter*.